Development of a Radio-Frequency Inductively Coupled Plasma Torch for near-Thermal Nitrogen Plasma Production

Murray Schild Jobbins

A thesis submitted for the degree of

Master of Philosophy

The Australian National University

Research School of Physics



Australian National University

June 2026

© Copyright by Murray Schild Jobbins, 2026

All Rights Reserved

Declaration

I hereby declare that the work undertaken in this thesis has been conducted by me alone, except where indicated in the text. I conducted this work between August 2022 and June 2026, during which period I was an MPhil student at the Australian National University. I acknowledge this work has been completed on the lands of the Ngunnawal and Ngambri people, the traditional owners of the land of the ANU, and pay my respect to the elders past and present. This thesis, in whole or any part of it, has not been submitted to this or any other university for a degree.

Murray Schild Jobbins

29 June 2026

Acknowledgements

Firstly, I must extend my sincere gratitude to my primary supervisor Cormac Corr, for his guidance over the course of this work. I truly appreciate his patience, which was no doubt stretched at times by my obsessing over irrelevant details.

I'd also like to thank my associate supervisors, Trevor Lafleur and James Sullivan, for their feedback and thoughtful advice.

My thanks to Michael Blacksell and the RSPhys workshop for their advice on and production of the key components of the torch.

To my colleagues in the group: Ash Pascale, thank you for the incredibly helpful guidance in assembling and operating the torch, and for your generosity with snacks and energy drinks. Tom Hort, thank you for your assistance with troubleshooting the rig, and being much more on top of what goes where than I am. Josh Wei, thank you for your thoughtful feedback and your help taking photos of the sparking on the coil. Bryan Teo, thank you for the lunchtime banter and letting me share your lab.

Finally I want to thank my parents for their support, and my friends Tian Xiao, Josh, Callum, Holly, and Matt for their encouragement and advice.

Abstract

Electrification of heat production is vital for a transition to a low-carbon economy. Current electric heating technologies are not well adapted to very high temperature processes (>800 C°), limiting the viability of decarbonisation of industries such as steelmaking and cement production. Plasma technologies show potential as electrically-driven sources of process heat. Current large-scale industrial plasma torches primarily generate plasma through arc discharges, which require frequent replacement of costly plasma-facing electrodes and can be prone to instability. Radio-Frequency inductively-coupled plasma (RF-ICP) is an alternate method of thermal plasma generation that does not require contact between plasma and electrodes. The technology already sees use in some industrial applications due to its high chemical purity and suitable device geometry. Historically, ICPs have primarily been operated using argon gas, the cost of which may limit the economic viability of large-scale heating applications. As a result, few studies have evaluated or developed RF-ICPs purely as a source of process heat.

In this research, a 1kW RF-ICP device was developed for the generation of near-thermal plasma in nitrogen gas, employing a 27.12 MHz AC power supply and a reverse vortex flow regime in the plasma source. The thermal behaviour and plasma parameters of the device are characterised for a constant input power of 950 W, with gas flows rates of 2.5-12.5 slpm and discharge pressures of 3-300 Torr. Optical Emission Spectrometry (OES) is used to determine the rotational and vibrational temperatures of the $N_2(C)$ and $N_2^+(B)$ metastable states using Second Positive and First Negative emission system spectra captured in the plasma source and plume. Two spectral fitting models, Specair and MassiveOES, are examined and employed. Equilibration between the spectrally-determined $N_2(C)$ rotational temperature and neutral gas temperature in the plasma in most examined conditions allows the impacts of flow rate and pressure on plasma temperature to be studied. Plasma resistance is determined for all discharges using current probe measurements. A simple analytical model is developed to estimate electron temperatures present in the discharge, using gas densities calculated using spectrally-determined gas temperatures. These electron temperatures are used alongside plasma resistance measurements to evaluate electron densities.

It is shown that variation in flow rate yielded notably different trends with respect to pressure for all examined parameters, indicating the gas dynamics of the reverse vortex flow influence the properties and stability of a discharge. This is evidenced by electron density results, in which flows above 5 slpm exhibit plateaus with respect to pressure. These plateaus start at pressures and electron densities that decrease

as flow rate increases. Such results suggest that increased flow rates result in greater charged particle losses into the plume. This is supported by measurements of time-varying oscillations in electron density, which are found to strengthen under similar conditions. Temperature results find that for higher flow rates, gas temperatures in the plume surpass those in the source. It is shown that the observed enthalpy changes cannot be accounted for by relaxation of the vibrational mode, suggesting the increased heating may result from electron-ion recombination. This study indicates that nitrogen-fed, reverse vortex RF-ICPs show promise as sources of process heat, however better understanding of fluid flow behaviour within the plasma source is necessary to electrically optimise such devices for operation at higher powers and pressures.

Contents

List of Figures v
List of Tables xi

1 Introduction **1**
1.1 Fundamentals of Plasma 2
1.2 High-Enthalpy Plasma Sources 5
1.3 Nitrogen Plasma 17
1.4 Thesis Goals and Outline 22

2 Experimental Design and Methodology **24**
2.1 Plasma Torch Design 24
2.2 Experimental Set-up 28
2.3 Diagnostics 33
2.4 Temperature Determination from Experimental Spectra 38

3 Thermal Characterisation **45**
3.1 Neutral Gas Density and Collision Frequency 45
3.2 Neutral Gas Temperatures 52
3.3 $N_2(C)$ Vibrational Temperatures 57
3.4 $N_2^+(B)$ Temperatures 67
3.5 Evaluation of Thermal Characteristics 72
3.6 Summary 80

4 Plasma Behaviour **82**
4.1 Analytical Model 82
4.2 Plasma Parameters 87
4.3 Plasma Oscillation 101
4.4 Summary 109

5 Summary and Conclusions **111**
5.1 Summary 111
5.2 Future Works 117
5.3 Final Remarks 118

List of Figures

1.1 An example plot for electron, ion and gas temperatures in a plasma against pressure, distinguishing the non-thermal and thermal regimes. Figure from [1]. 4

1.2 Schematic of a non-transferred DC arc discharge torch. Figure from [2]. 6

1.3 Schematic of a surface-wave driven microwave plasma torch. Figure adapted from [3]. 9

1.4 Schematic diagrams of (a) cylindrical and (b) planar inductively coupled plasma devices. Figure adapted from original in [4]. 10

1.5 Schematic diagram of the gas flow through a typical Fassel torch. Strong sheath gas flows are used to push the peak heating regions toward the device axis and minimise thermal load on the walls. 13

1.6 Idealised gas flow through a reverse-vortex fed plasma source. Figure adapted from [5]. 15

1.7 Electron-neutral elastic scattering cross sections against incident electron energy for nitrogen and argon. Nitrogen data from [6], Argon data from [7]. 17

1.8 Potential energy curves of several relevant states of the N_2 molecule. Highlighted areas indicate the internuclear distance range of the N_2(X) ground state (blue), N_2(C) excited state (green), and N_2(A) excited state (orange). Plotted using RKR potential curves from Ref.[8] and an approximation to the N_2^- (X) curve described in Ref.[9]. . . . 19

1.9 Example emission spectra for molecular nitrogen (left) and argon (right). An additional line in the argon spectrum originating from hydrogen is labelled. Argon spectrum from [10]. 20

2.1 Schematic cross-section of the device source region. Key parameters of the discharge geometry are labelled, with the lengths used in this work provided in Table 2.1. Figure adapted from [11]. 25

2.2 Left: Circuit diagram model of an RF discharge, showing the inductive and capacitive modes in parallel. Right: Modelled electron density of a low-pressure inductive discharge against coil current. Higher driving frequencies produce higher electron densities when the capacitive mode dominates the discharge. Figures adapted from [12]. . . . 27

2.3 Schematic diagram of the experimental set-up. 28

2.4 Circuit diagram of the modified Pi-type matching network. 30

2.5 Matchbox model results showing capacitance required for perfect matching against discharge electron density for discharges in argon and nitrogen. Dashed lines indicate the maximum capacitances of the variable capacitors selected. 32

2.6 Relative intensity calibration procedure with example curves for the wavelength region centred on ∼400 nm. Experimental spectrum captured in the source region of a 950 W, 5 slpm discharge at 9 Torr. . . 36

2.7 Example step-and-glue spectrum with major peaks and vibrational band structures of the First Negative and Second Positive systems labelled. Experimental data captured along the device axis of a 950 W, 5 slpm discharge at a pressure of 200 T. Emission system peaks and contribution regions labelled according to Ref.[8]. 39

2.8 Comparison of neutral spectral fitting produced using MassiveOES (top) and Specair (bottom). Experimental spectrum captured downstream of a 950 W, 7.5 slpm discharge at 13 Torr. 42

2.9 Comparison of ion spectral fitting produced using MassiveOES (top) and Specair (bottom). Experimental spectrum captured in the source of a 950 W, 5 slpm discharge at 204 Torr. 44

3.1 Neutral gas density calculated for the source region against pressure for all examined discharge conditions. 47

3.2 Average axial flow velocity against pressure for all flow rates, calculated assuming an incompressible flow using calculated values of average source density. The dashed grey line corresponds to the local speed of sound, calculated using average temperatures calculated from 5 slpm flows. Other flow rates yield similar speeds of sound. . . 48

3.3 Downstream pressures against upstream pressures, measured for all discharges and flow rates. Left: full pressure range examined, Right: detailed view of lower pressures, corresponding to the highlighted region of the full range plot. Dashed lines indicate the downstream pressure required for the pressure ratio to produce the velocities shown in Figure 3.2. 49

3.4 Neutral gas collision frequency against pressure, calculated using pressures and $N_2(C)$ rotational temperatures captured in the source region. The dashed grey line marks the rate corresponding to a collision interval one-quarter of the radiative lifetime of the $N_2(C)$ state. The rotational temperature determined using the Second Positive system cannot be assumed to be in equilibrium with gas temperatures for discharges exhibiting collision frequencies below this value. 50

3.5 Neutral gas collision frequency against pressure, calculated using pressures and $N_2(C)$ rotational temperatures captured in the plume. The dashed grey line marks the rate corresponding to a collision interval one-quarter of the radiative lifetime of the $N_2(C)$ state. The rotational temperature determined using the Second Positive system cannot be assumed to be in equilibrium with gas temperatures for discharges exhibiting collision frequencies below this value. 51

3.6 Gas temperatures measured in the source region against pressure, for all examined discharges where equilibration between $N_2(C)$ rotational temperatures and gas temperature occurs. 52

3.7 Gas temperatures measured in the plume against pressure, for all examined discharges where equilibration between $N_2(C)$ rotational temperatures and gas temperature occurs. 55

3.8 Difference between the measured gas temperatures in the source and plume, plotted against pressure for all examined discharges where equilibration between $N_2(C)$ rotational temperatures and gas temperature occurs. Positive values indicate the source is hotter, negative indicate the plume is hotter. 56

3.9 Comparison of neutral spectral fitting of the (2-5) and (1-4) peaks (top), the (1-4) and (0-3) peaks (middle) and all three peaks (bottom). All fitted spectra were produced using MassiveOES. Experimental spectrum captured in the source of a 950 W, 7.5 slpm discharge at 14 Torr. 58

3.10 Calculated relative populations of the v=0,1,2 vibrational states plotted against vibrational energy for data captured in the source of a 950 W, 7.5 slpm discharge at 14 Torr. Dashed lines show the trend-lines expected for Boltzmann distributions with vibrational temperatures corresponding to the fittings shown in Figure 3.9. See below for details on the calculation method. 59

3.11 Calculated relative populations of the vibrational levels of the N_2 $C^3\Pi_u$ state against pressure in the source region of a 950 W, 5slpm discharge. The expected ground state population based on the temperature of the upper vibrational levels, scaled to match the upper state populations of the measured spectra, is indicated with a dashed line. Uncertainties propagated from the error of measured vibrational temperature. 60

3.12 Deficit in the calculated relative population of the v=0 state compared to a Boltzmann distribution of temperature T_{vib}(v=1,2) against pressure for all examined flow rates. Uncertainties propagated from the error of measured vibrational temperature. 63

3.13 N_2(C) vibrational temperatures measured in the source region against pressure. Two temperatures are used to describe the non-Boltzmann population distribution observed across vibrational states. 65

3.14 N_2(C) vibrational temperatures measured in the plume against pressure. 66

3.15 Source region N_2+(B) rotational temperatures (circles) and vibrational temperatures (stars) against pressure. 69

3.16 Plume N_2+(B) rotational temperatures (circles) and vibrational temperatures (stars) against pressure. 70

3.17 Steady-state coolant water output temperatures achieved by the chiller, plotted against pressure. 73

3.18 Difference between the source region rotational and vibrational enthalpies and those of the plume, plotted against pressure. Positive values indicate enthalpy is higher in the source region, negative values indicate the plume enthalpies are higher. 75

3.19 Estimated thermal efficiency of the device against pressure. Calculated assuming the entire flow through the torch is heated to the temperatures measured in the plume. 79

4.1 An example of solving for ω_{pe} using the measured plasma resistance. Two solutions exist where measured R_p equals R_p evaluated using Equation 4.8. These correspond to different electron densities that produce the same plasma resistance, the under-dense (low) and over-dense (high) scenarios. 87

4.2 Electron temperatures determined by the model using experimental temperature and pressure measurements. Circles indicate values calculated using measured gas temperatures, crosses indicate values calculated assuming a gas temperature equal to that of the lowest pressure conditions for which a gas temperature could be measured for a discharge of the same flow rate. 88

4.3 Measured RF efficiency against pressure in the source region. 90

4.4 Electron density, calculated using measured plasma resistance and modelled electron temperatures, plotted against pressure in the source. Circles indicate values calculated using measured gas temperatures, crosses indicate values calculated assuming a gas temperature equal to that of the lowest pressure conditions for which a gas temperature could be measured for a discharge of the same flow rate. 92

4.5 Ionisation rate factor calculated using electron temperatures determined by the global model from measured pressures and temperatures, plotted against neutral gas density for all data points. The dashed line shows the data can be approximately fit to the inverse square of neutral gas density. 95

4.6 Plots of gas temperatures (left axis) and electron densities (right axis) against pressure for discharges with flow rates of a) 7.5 slpm, b) 10 slpm, and c) 12.5 slpm. Electron densities for the 5 slpm case are included on all plots (grey markers with dashed line) as an non-plateauing baseline for electron density. The dashed black line on each plot indicates the approximate pressure where the electron density trend diverges from the 5 slpm case, marking the start of the plateau. 97

4.7 Skin depth, determined using calculated electron density values, against pressure. Circles indicate values calculated using measured gas temperatures, crosses indicate values calculated assuming a gas temperature equal to that of the lowest pressure conditions for which a gas temperature could be measured for a discharge of the same flow rate. 98

4.8 Ionisation ratio, determined using calculated electron density values, against pressure. Circles indicate values calculated using measured gas temperatures, crosses indicate values calculated assuming a gas temperature equal to that of the lowest pressure conditions for which a gas temperature could be measured for a discharge of the same flow rate. 100
4.9 Time-resolved current probe (top) and photodiode (bottom) signals, produced by a 950 W, 5 slpm discharge at 400 Torr. Noise in the current probe signal is produced by the sampling rate of the oscilloscope data output, however evidence of a regular oscillation can be seen in the width of the peak-to-peak envelope (middle). 102
4.10 Dominant frequency of the oscillation (top), and ratio between the amplitude of the emission intensity oscillation and the time-averaged output (bottom), against flow rate for a 600 W discharge at 20 Torr. 104
4.11 Dominant frequency of the oscillation (top), and ratio between the amplitude of the emission intensity oscillation and the time-averaged output (bottom), against pressure for a 600 W discharge with a flow rate of 10 slpm. 105
4.12 Dominant frequency of the oscillation (top), and ratio between the amplitude of the emission intensity oscillation and the time-averaged output (bottom), against pressure for 950 W discharges of differing flow rates. 107

List of Tables

2.1 Values used in this work for key parameters of the source region geometry presented in Figure 2.1. 26

3.1 $N_2(C)$ production mechanisms assessed in the kinetic model of Ref. [13] 61

5.1 Maximum electron densities achieved by feed gas flow rate, 950 W supplied power. Note that the 2.5 slpm discharge did not exhibit an electron density plateau in the examined pressure range, which did not extend beyond 188 Torr due to the plume being too dim for OES measurements. 115

Chapter 1

Introduction

In response to the threat posed by anthropogenic climate change, significant efforts across the world are being made to reduce or eliminate the use of fossil fuels. This technological and economic transition away from carbon-intensive activities requires the development or refinement of viable alternatives for existing industrial processes that generate or consume energy. Electricity generation occupies a particular focus in discussions of the energy transition, as the sector is the largest contributor to global emissions. However, as of 2023, the power industry produces only 29% of all greenhouse gas emissions, with the next most significant contributor at 21% being industrial processing [14]. While significant strides have been made in decarbonising electricity production [15], uptake of low- or zero- carbon industrial processing methods has been limited [16, 17], suggesting further work is required in developing these technologies.

Energy consumed in industrial processes is primarily used as heat, constituting 74% of industrial energy use globally [18]. This heat is produced largely by combustion of fossil fuels, with only 14% produced using low- or no- carbon sources, the vast majority of which being bioenergy [19]. Approaches for the decarbonisation of industrial heating are dependent on the temperature needed by a given process. For temperatures below $\sim$250°C, electrification using highly efficient heat pumps is largely being pursued, allowing such processes to use renewable energy. Geothermal and concentrated solar thermal technologies are also of use in these applications, though see greater geographical constraints in their use [20].

The pathway to decarbonisation for processes requiring high temperatures ($>$ 800°C) is less clear however, as implementing current high-temperature electric heat sources would require significant redesign of the relevant industrial processes [20]. As the cost of electricity is still coupled to the wholesale price of fossil fuels [21], the operational costs of these electric heat sources are generally similar to or higher than the existing natural gas- or coal-burning infrastructure [22]. This means the capital cost of redesign cannot be recovered without additional large investment into

renewable power infrastructure, discouraging the uptake of such technologies.

Additionally, high-temperature electric heat sources are limited by the heating methods they employ. The two most widely used high temperature electric heating methods in heavy industry, induction heating and electric arc furnaces, both rely on the target material being electrically conductive [23]. While useful for metallurgical applications such as aluminium and steel processing, such heat sources cannot be employed in many carbon-intensive industries which involve non-conductive or fluid feedstock, such as cement and ammonia production, or hydrocarbon refinement.

These limitations preventing electrification of high-temperature industrial processes may be overcome using low-cost plasma torches. Plasma generators can be designed to efficiently heat jets of feedstock gas to very high temperatures (> 5000K [24]), surpassing the physical constraints imposed by current heating methods. As plasma torches produce streams of heated gas, they may be compatible with infrastructure currently using fossil-fuels, allowing existing facilities to be electrified by retrofit, instead of costly redevelopment [25]. This thesis presents the development and characterisation of a plasma torch, designed and built as a test article for producing plasma jets of nitrogen heated to industrially-relevant temperatures while operating at industrially-relevant pressures.

This chapter will provide an introduction to the operating principles of a plasma torch and the broad context of developments in thermal plasma generation. First a fundamental overview of plasma is presented, focusing on the differences between non-thermal and thermal plasma. An exploration of high enthalpy plasma sources follows, examining common methods of thermal plasma generation and reviewing the current development of inductively-coupled plasma torches. The impacts of using nitrogen as a plasma feed gas are then detailed, particularly in the context of spectrometry, with a discussion of the vibrational non-equilibrium often observed in nitrogen plasma in the literature. Finally, the goals and outline of this thesis is presented.

1.1 Fundamentals of Plasma

Plasma is a state of matter made up of a mixture of freely moving electrons, neutral particles, positive ions and, in some cases, negative ions. The ratios of these components can vary, however the positive and negative charge densities must be approximately equal throughout a substance to meet the definition of a plasma. This attribute is referred to as *quasi-neutrality*. The mobility of free charges allows

them to respond to electric fields. This results in the charged particles exhibiting *collective behaviour*, as the movements of charges give rise to local electric fields and, through the currents generated by their motion, magnetic fields that produce forces on other charged particles in the substance. The requirement of collective behaviour specifically distinguishes plasmas from slightly ionised gases, as it defines plasma as having high enough charge density that forces can be conveyed between constituent particles by means other than direct collisions, meaning that the motion of a constituent particle is determined not only on its local conditions, but the conditions of distant regions of the plasma [26].

Due to the collective behaviour of charged particles, a plasma can be coupled to an externally applied electric field. The nature of this coupling can vary significantly depending on the properties of both the applied field and the plasma. Applying a constant electric field or one with a low frequency of oscillation results in a plasma that acts as a conductor. At higher frequencies a plasma will behave as a dielectric medium, with free charges moving to produce electric fields that cancel out the externally applied field [12]. The exact frequencies at which this change occurs is dependent on the density of charged particles in the plasma. While operating as a dielectric medium the plasma functions as a source of impedance, thus energy is coupled out of the external electric field and into the plasma. This energy flow increases the kinetic energy of charged particles. Depending on the overall density of the plasma (that its, the combined densities of neutral and charged particles), these charged particles may experience collisions with each other and with neutral particles, resulting in various forms of thermal and electrical excitation, including ionisation [4]. In sparse plasma, where collisions are too infrequent to dominate plasma behaviour, this energy remains in the charged particles, but may be conveyed between them by electro-magnetic waves or ambipolar diffusion [26].

1.1.1 Plasma Thermalisation

The constituent particles making up any plasma differ significantly in mass. Electrons, typically either the only or most abundant negatively charged particle present in a plasma, are far lighter than even the smallest possible ion, as a single proton is approximately 2000 times more massive. As a result, external electric fields accelerate electrons much more rapidly than ions.

Since temperature is determined by the average kinetic energy of constituent particles, many plasmas (both artificial and naturally occurring) cannot be described by a single temperature. Instead, each species exists in its own temperature distribution, typically defined by Maxwell-Boltzmann distributions [26]. Such plasmas

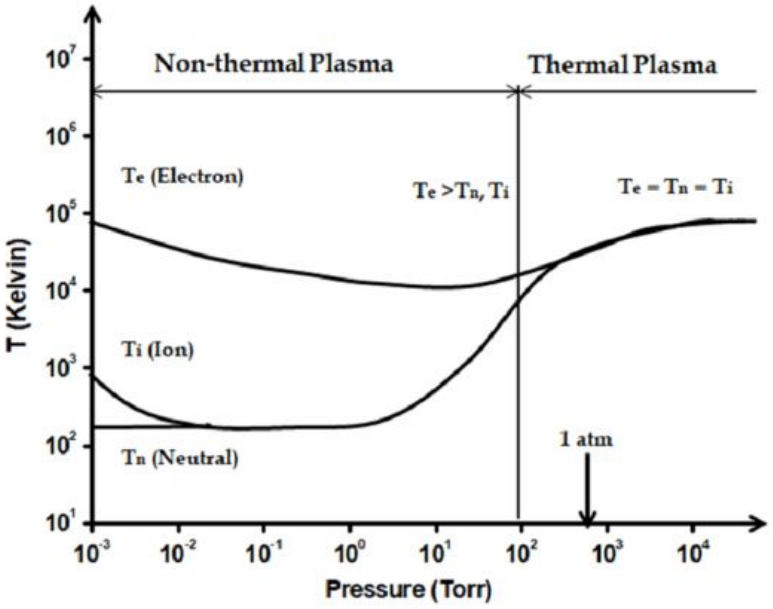

Figure 1.1: An example plot for electron, ion and gas temperatures in a plasma against pressure, distinguishing the non-thermal and thermal regimes. Figure from [1].

do not exhibit local thermal equilibrium across constituent species, and are thus referred to as *non-thermal plasma* [27].

These temperature differences can only be maintained in operating conditions with sufficiently low collision rates between electrons and other present species [28]. As collision rate increases, more energy flows out of electrons and into the rest of the plasma through scattering collisions, yielding lower electron temperatures and higher gas temperatures. Therefore, sufficiently high collision rates produce plasma where electrons are in thermal equilibrium with the other plasma species, which is referred to as *thermal plasma*.

Collision rate is a function of particle density, which itself is weakly dependent on temperature and strongly dependent on pressure. Pressure can therefore be used as a proxy for collision rate, as in Figure 1.1. The figure shows the thermalisation of a plasma as pressure increases. A strongly non-equilibrium temperature distribution exists across the plasma species for pressures up to 100 Torr (∼0.15 atm), by which point the electron temperature is only two times the gas temperature. By atmospheric pressure the remaining temperature difference has been closed, and all species exhibit a shared temperature, often called the plasma temperature. Thus, thermal plasma converts energy from electric fields into thermal motion of electrons, which cascades into thermal motion of all plasma particles. This makes it appealing as a possible electrification method for high-temperature industrial heat

sources.

1.2 High-Enthalpy Plasma Sources

The industrially-relevant thermal plasma generators of interest in this work fall within a category of plasma devices referred to as high-enthalpy sources. These devices produce sustained flows of highly energetic plasma, and are therefore capable of outputting significant heat fluxes [29]. The specification of high-enthalpy plasma as opposed to high-temperature or simply thermal plasma is used to distinguish such devices from lower-energy intermittent sources such as pulsed laser or pulsed electric discharges, which are capable of producing high transient temperatures but exhibit low total enthalpy. Additionally, the term is inclusive of devices that output plasma flows with high kinetic energy but low thermal energy, which are primarily seen in wind-tunnel devices for simulating atmospheric re-entry and typically employ similar plasma generation methods to high-temperature devices [30, 31].

A feature exhibited across all high-enthalpy plasma sources is the ejection of a jet or plume of high-energy plasma. These plumes allow interactions between plasma and other matter to occur outside of a region of active plasma generation. This offers a range of benefits, particularly in the context of industrial applications, including removing geometric constraints arising from the plasma source design and providing fine control of heat flux delivered to target matter. It also offers a benefit to the stability of the plasma by removing the need to pass target matter through the source region, preventing perturbation of the electromagnetic fields or fluid flows that maintain the discharge.

1.2.1 Thermal Plasma Generation Methods

High-enthalpy plasma sources can employ a range of methods for generating plasma, the selection of which is informed by operating conditions, intended use and economic limitations. The three most commonly produced forms of thermal plasma are arc discharges, microwave plasma, and radio-frequency, inductively coupled plasma (RF-ICP) [27], which are detailed in the following sections.

Arc Discharge Plasma

Arc discharge plasma sources generate electric arcs using a variety of electrode configurations and materials. Figure 1.2 depicts a simplified diagram of a DC, blown-arc plasma torch. Plasma is generated by arcing between a cathode positioned along the device axis and an anode that, in this case, also functions as a nozzle. As the

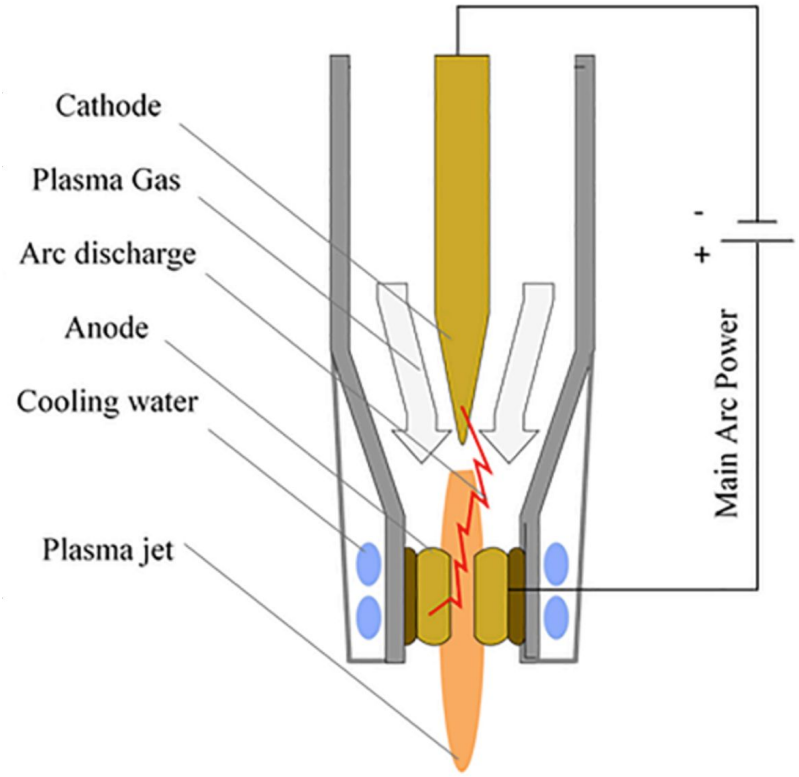

Figure 1.2: Schematic of a non-transferred DC arc discharge torch. Figure from [2].

electrical conductivity of plasma increases with temperature, the path of the arc, following the path of least resistance between the electrodes, will preferentially flow through the hottest plasma regions [32]. Using this principle, the flow of cold feed gas around the cathode and along the device walls serves to minimise thermal load on the walls and keep the arc aligned with the device axis, as the arc is discouraged from flowing through regions where electrical conductivity is reduced due to strong mixing with and convective heat flow to fresh feed gas. This protective effect can be amplified using a vortex flow, which adds a centripetal force that keeps cool gas close to the walls and the upper surface of the anode. Axial flow is still necessary, however, both to help push hot plasma out of the device and to cool the plasma closest to the cathode to prevent damage.

The peak plasma temperature in arcs generated in such devices can reach over 20 000 K near the cathode, falling to around 15 000 K at the nozzle exit. The rapid rate at which heating occurs in the arc creates strong, laminar flows due to thermal expansion, limiting mixing between plasma directly in the path of the arc and that around it. As a result, the radial temperature gradients of arc discharge plasma are steep, reducing only after turbulent mixing with the atmosphere once exhausted from the device [28]. Despite high peak temperatures, the overall average

temperature of plasma produced by such devices is around 4000 K [33].

Arc discharge sources are capable of operating at high powers and pressures, which has made them appealing for wind tunnel applications. High operating powers result in significant heating of high flow rates of working gas, while high operating pressures allows a continuous discharge to be maintained while a nozzle constrains and accelerates that heated gas, increasing the pressure in the plasma source up to several atmospheres. Together these factors allow for the production of high enthalpy flows that can accurately simulate heat fluxes experienced during atmospheric reentry from lunar or interplanetary speeds. The Plasma Wind Tunnel facility at the Institute for Space Systems operates an arc discharge source with input powers up to 6 MW and at pressures as high as 10 MPa ($\sim$100 atm) [34, 35]. The Interaction Heating Facility arcjet at the NASA Ames Research Centre operates at 60 MW and 5 atm for up to an hour [36].

Metals used for cathodes, which are exposed to the hottest regions of the arc, must be thermally robust in addition to exhibiting suitably high electrical conductivity. A high melting point and thermal conductivity are required, the former to optimise operating conditions of the plasma and the latter to optimise the efficiency of thermal management such as water cooling [37]. Additionally, as local electric fields strongly accelerate nearby ions toward the cathode, they must also resist sputtering caused by the resulting bombardment [38]. Due to these requirements, tungsten is the historically dominant choice for cathodes in high-enthalpy arc discharge devices [39].

Even after accounting for these considerations, cathode wear imposes a significant constraint on the uptake of arc discharge devices. Despite the metal's hardiness, tungsten cathodes still see operational lifetimes as low as 20-200 hours [33]. The high cost of tungsten necessitates that when it is used as an electrode, its lifetime is extended through use of a water cooling system. This results in heat losses up to 30-50% of the the input energy, motivating research into and development of consumable graphite electrodes. These electrodes experience significantly more wear than their metal counterparts, however the low cost of the material allows for its constant replenishment [40]. Plasma torches using steel or copper alloy cathodes have also been developed, with significantly longer lifetimes of up to 1000 hours. However these devices operate at average temperatures of just $\sim$500 K [33]. Regardless of material, cathode degradation poses two major issues for industrial applications. Firstly, plasma jets produced by these devices are contaminated by varying amounts of electrode material, preventing use where plasma purity is a concern [2]. Secondly, both the materials and the machine downtime required to replace

or service electrodes increases operational costs in industrial settings [41]. These limitations suggests that development of thermal plasma sources utilising electrode-less generation methods, namely microwave and RF inductively coupled plasma, may be necessary to enable the decarboniation of many industrial processes.

Microwave Plasma

Unlike arc discharge plasma, which is sustained by exposure to steady electric fields, both microwave and inductively coupled plasma are sustained by electromagnetic oscillations. This difference enables the latter generation methods to operate without direct contact between electrodes and plasma, as electromagnetic waves produced by an antenna can propagate through a dielectric material and into a plasma. The primary difference between microwave and inductively coupled plasma is the frequency of the exciting electromagnetic wave, which gives rise to significant differences in device operation and plasma behaviour.

In the case of microwave plasma, the discharge is sustained using very high frequency waves, between 500 MHz and 10 GHz [27]. Waves of these frequencies have no effect on ions present in a plasma, as the electromagnetic fields vary too rapidly to overcome the high inertia of such massive particles. Even the comparatively small mass of electrons is enough to limit coupling between particle motion and wave energy. This leads to low attenuation of the driving wave, allowing it to penetrate far into plasma before its energy is fully dissipated [4]. While this property limits the amount of energy delivered into any given volume within a plasma, it also allows sufficiently energetic waves to sustain plasmas with high volumes compared to other generation methods [27].

Thermal microwave plasma devices typically consist of a magnetron connected to a waveguide, typically by way of a directional coupler and waveguide tuner, which produces and concentrates microwaves into a resonator region through which a dielectric tube runs perpendicular to the waveguide. Figure 1.3 shows a diagram of such a device. Gas injected into the dielectric tube is heated to a plasma by the incident microwaves, producing a plasma jet within the tube. When the electron density and thus electrical conductivity of the plasma within the waveguide is low, microwaves travelling along the waveguide can penetrate the plasma transversely, delivering energy across the radius of the plasma jet. When electron density is sufficiently high as to prevent microwaves reaching the device axis, energy is deposited in a smaller volume near the surface, increasing local electron density until it behaves as a conductor. This allows the plasma jet to act as a waveguide, either independently as a circular waveguide or coupled with a metal sheath around the dielectric

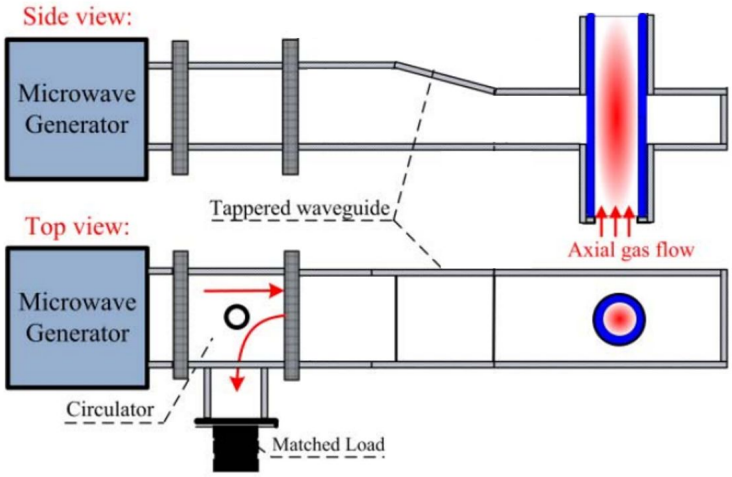

Figure 1.3: Schematic of a surface-wave driven microwave plasma torch. Figure adapted from [3].

tube as the inner conductor of a coaxial waveguide, depending on device design and geometry [42]. This allows the driving waves to travel axially along the surface of the plasma jet, outside of the region enclosed by the device waveguide. This delivers energy into cooler regions of the plasma and improves coupling by reducing the power reflected back toward the magnetron [3].

Due to peak heating occurring at the surface of the plasma, heat losses to the dielectric tube are a vital consideration of source design and a key limiting factor in both peak operating powers and peak gas temperatures [27]. As a result, microwave plasma torches used in industrial applications operate with significantly lower powers than those typical of arc discharges [43], with the highest-power commercially available microwave plasma source operating using up to 100kW [44]. This limits the peak temperatures achieved in microwave plasmas to ∼6000 K [43, 45], significantly lower than those present in arc discharges. Thermal efficiencies reported for microwave torches, at ∼55% [46], also fall below those typical of arc discharges at 65-78% [47]. This is largely a result of the energy coupling between source and plasma occurring over a comparatively greater volume in microwave discharges, producing lower peak temperatures and larger surface areas for conductive and radiative heat losses.

Microwave plasma sources can be developed for operation across a wide range of pressures, with thermal applications operating almost exclusively at atmospheric pressure [43, 48].

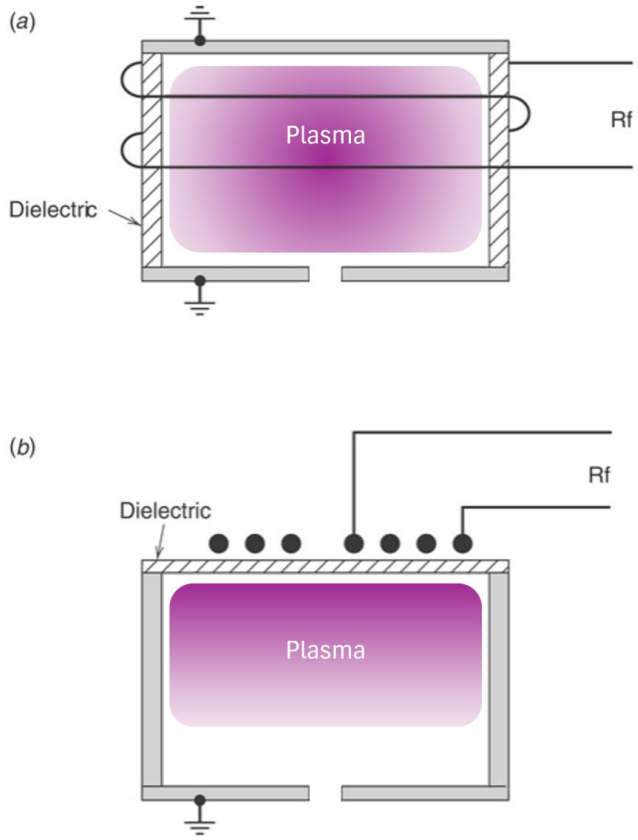

Figure 1.4: Schematic diagrams of (a) cylindrical and (b) planar inductively coupled plasma devices. Figure adapted from original in [4].

Inductively Coupled Plasma

Radio-frequency inductively coupled plasma (RF-ICP) operates using electromagnetic oscillations in the frequency range of 1 to 500 MHz, most commonly at 13.56 MHz [4]. Such frequencies are, like microwaves, too high for efficient coupling to the motion of ions. Unlike microwaves, however, waves in this frequency range can couple strongly to electron motion, leading to comparatively strong wave attenuation within the plasma.

Figure 1.4 depicts the two common designs of inductively coupled plasma devices. RF alternating current flows through a coil, either planar or cylindrical, which is separated from the plasma volume by a dielectric window. The oscillating current through the coil produces an oscillating magnetic field in the plasma region. This field induces an alternating current within the plasma that flows to oppose the change in the magnetic field. This current accelerates the far more mobile electrons through the plasma, thereby coupling the energy of the oscillating electromagnetic fields into electron motion. Collisions between accelerated electrons and

other species in the plasma further distribute this energy deposited into the electrons into various forms of thermal and chemical energy across the plasma. As the induced current moves to negate changes in the external field, at sufficient electron densities the core of the plasma under the coil will be fully shielded from the coil fields. This results in energy coupled into inductive plasma being deposited in an annular region extending inward from the dielectric walls, to a depth called the skin depth, beyond which the coil fields are effectively fully attenuated.

RF ICP devices operate over a wide range of input powers and discharge pressures. Atmospheric pressure thermal ICP devices can achieve peak temperatures as high as 12000 K [28], higher than microwave plasmas but lower than arc discharges. This is due to the plasma generating volume of RF ICPs being smaller than microwave devices and larger than arc discharges. The peak operating powers achieved in RF ICPs are significantly higher than in microwave devices, reaching up to 1.3 MW in low-pressure devices used for re-entry simulation [49]. Industrially available devices reach as high as 1 MW of power draw, though power transfer efficiency has not been reported. Operation at or above atmospheric pressure is common for such high-power ICPs, with claims of operation up to 7 atm [50]. Suggestion has been made that scaling devices up to operate at powers up to 15 MW is possible, though without significant changes to typical source designs the greater heat flux to the walls in such devices would necessitate the development of improved cooling methods [50]. It is therefore unlikely that RF ICPs will be able to match arc discharge sources for single-source power output. Nonetheless, the greater scaling potential of inductively coupled devices compared to microwave sources and lower ongoing maintenance and material needs compared to arc discharges together suggest the technology may be well suited to electrical generation of industrial process heat.

1.2.2 High-Enthalpy ICP Torch Development

In 1961 Reed published his work detailing the first inductively coupled plasma torch, an atmospheric pressure discharge that used thermal expansion of argon feed gas to expel a high-temperature jet of plasma from under the antenna [51]. This initial design remained largely unchanged for several decades [52, 53], during which time uptake of thermal ICP torches remained limited. They saw use primarily in applications that required the very high purity offered by electrodeless plasma that cannot be achieved by arc discharge sources. These included sample atomisation for use in optical and mass spectrometry, and deposition of cladding on fibre-optic lines.

Part of this slow uptake may be attributable to the thermal efficiency of prevailing torch designs. In his work Reed reported the power deposited in the gas, lost to ra-

diation and lost to the walls for several plasmas generated using differing flow rates. Of these plasmas the highest reported share of the total coupled power deposited in the gas (ie. highest thermal efficiency) was ∼45%. Additionally, the reported power transfer efficiency of the torch was 52-57%. Taken together, the best possible electrothermal efficiency offered by the torch was ∼26%. It therefore follows that the uptake of the technology focused on applications requiring high chemical purity.

The decades since Reed's work have seen significant increases in efficiency exhibited in RF-ICP devices. Improved matching networks and power supply electronics have lead to power transfer efficiencies of well optimised ICP torches reaching >95% [5]. Thermal efficiency improvements have been less drastic, though modern designs report thermal efficiencies up to 70% [54]. With these improvements to efficiency has come increased interest in RF ICP devices as a source of thermal plasma. Investigation and development of inductive plasma sources and reactors for a variety of material processing applications are occurring [55]. These applications include decomposition of volatile chemicals [56], carbon deposition for diamond production [57], and nanopowder synthesis [58].

The primary target of efforts to improve the thermal efficiency of ICP torches has been the convective heat flow from the hot plasma under the antenna to the device walls. This heat loss is minimised by establishing various gas flow regimes within the source region that push the hottest regions of plasma off the walls and toward the device axis. This is analogous to the gas flow considerations required in arc discharge sources to reduce thermal load to the electrodes and maintain arc stability. A range of insulating flow regimes have been developed.

Gas Flow Regimes

The simplest of such flow regimes is the forward vortex flow, produced by injecting the feed gas tangentially along the inner wall of the source region. This provides the injected gas with some azimuthal velocity, which produces a centripetal force that pushes the flow outward, against the wall [59]. This results in lower pressures along the device axis, encouraging the expansion of the heated gas under the coil radially inward, away from the outer wall. This technique was in fact implemented in Reed's torch, though in pursuit of plasma stability, not for thermal optimisation [51]. The low pressure region on the axis produces a recirculation zone slightly downstream of the coil, causing some plasma to flow back up toward the gas injection region. In Reed's torch this backflow helped prevent the plasma under the coil from being expelled faster than it could be replenished. While beneficial, a vortex flow alone is

insufficient for preventing significant heat flow to the walls.

In the decade following Reed's paper, work to adapt the RF ICP torch for atomic emission spectrometry led to the development of the Fassel torch, which introduced a gas flow regime that can significantly reduce heat loss to the walls [60]. A schematic of this flow regime is shown in Figure 1.5. In it, additional internal tubes are used to inject several distinct concentric feed gas flows into the source. The outermost flow closest to the wall is called the sheath gas, and typically constitutes a large majority of the total feed gas. This flow is introduced just upstream of the peak plasma heating region, which allows the thermal expansion of the hot plasma under the coil to push it close to the wall, allowing it to act as an insulating layer. The high share of total flow rate running through this sheath provides it with a high heat capacity, meaning even as it mixes with the hot plasma under the coil the temperature of gas directly against the wall is kept low. Sheath gas flow rates significantly higher than those near the centre also produce low pressures along the device axis, akin to a forward vortex flow, encouraging thermal expansion to push hot plasma inward, away from the walls [61].

While initially developed for relatively low-power torches used to atomise samples for atomic emission spectroscopy, the flow design of the Fassel torch is now utilised in a wide range of thermal ICP devices. The design is well suited to exposing target material that can be added to the feed gas flow, like powders or aqueous solutions, to high temperature thermal plasma, thus has been applied to processes such as powder spheroidisation, thermal spray deposition and nanoparticle synthesis [54].

The primary limitation of the Fassel torch is the very high sheath flow rates re-

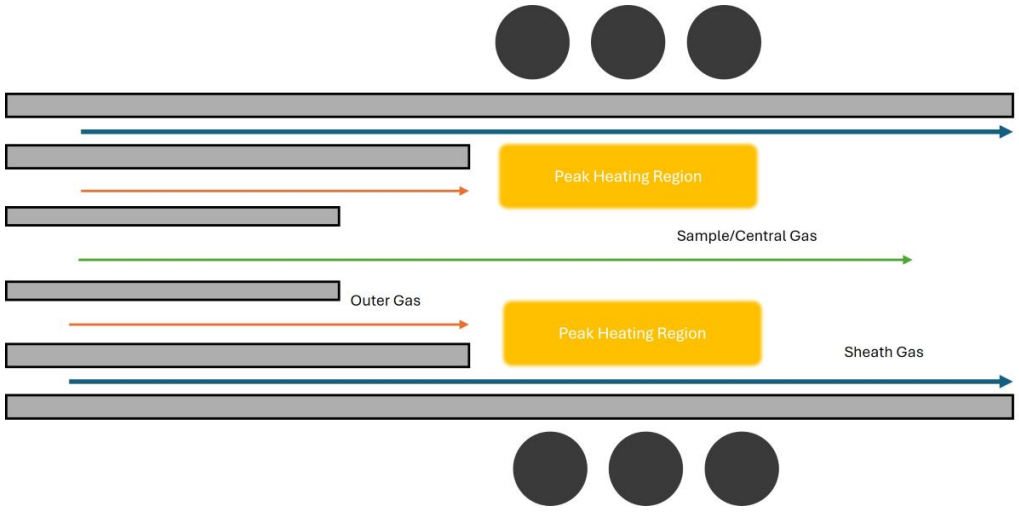

Figure 1.5: Schematic diagram of the gas flow through a typical Fassel torch. Strong sheath gas flows are used to push the peak heating regions toward the device axis and minimise thermal load on the walls.

quired to sufficiently cool the device walls [62]. RF-ICP torches often operate using argon feed gas, particularly those used in mass and optical emission spectrometry. Argon is produced by fractional distillation, an energy and capital intensive processes that results in high prices for the gas. Simply reducing the sheath flow rates to minimise gas consumption increases thermal flux to the walls, decreasing thermal efficiency and necessitating additional external cooling. A reduction in thermal efficiency in turn requires both higher overall energy use and higher-capacity RF power supplies, increasing capital costs and negating the savings from reducing gas consumption.

In response to this economic consideration, Alavi et. al. developed the conical torch in 2017 [63]. This design retains the central and sheath gas flows of the Fassel torch, while removing the intermediate flow using an expanding conical geometry for the outer walls and injector under the coil. Computational flow dynamics simulations showed a conical design results in less turbulent mixing under the coil compared to the Fassel torch, reducing heat flow into the sheath gas and wall. Initial experimental results indicated a conical torch operating with 900W achieved peak axial gas temperatures 1000-1700K higher than those achieved in a Fassel torch configuration using 1100W. Simulation results published by Ebrahimi et. al. in 2025 [54] supported the improved thermal performance of a conical torch design, seeing 25-50% lower gas consumption compared to a Fassel torch for power spheroidisation applications.

The results from Ebrahimi et. al. also portray an issue with scaling the power of such sheath-gas insulated torch designs, however. Thermal efficiencies were found to decrease substantially with increasing power at constant flow rates, from 69% at 5kW to 40% at 20kW. While changes to gas flow rates may be able to improve efficiencies at high powers somewhat, the reported energy balance values indicate that over two-thirds of the efficiency decrease is attributable to increased radiative losses from the plasma, not convective heat loss to the device. Fassel torches report similar decreases in thermal efficiency at high powers [61]. Both flow regimes rely on heating only a small amount of the total feed gas flow to very high temperatures, up to 9000-12000K, which then heats the the remaining gas upon mixing. At these temperatures the plasma produces significant optical emission, leading to radiative energy losses. Increasing supplied power typically increases peak temperature only slightly [54], as it increases electron density and thus decreases the skin depth of the plasma, increasing the surface area of the hot plasma region where radiative losses occur.

Decreasing the radiative losses and improving thermal efficiency in such plasmas

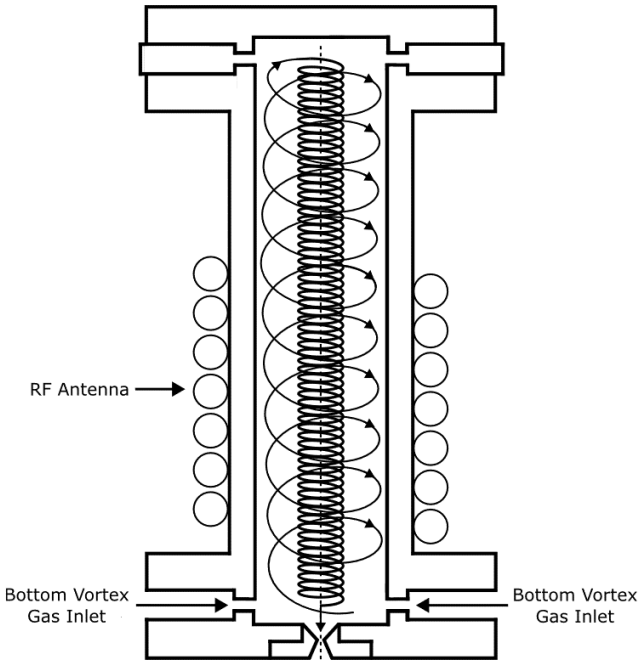

Figure 1.6: Idealised gas flow through a reverse-vortex fed plasma source. Figure adapted from [5].

requires a lower peak temperature. This is not optimal for heat flow into a centrally injected target material, and thus is not useful for spectrometry or similar materials processing applications. For process heat production, however, the primary consideration is the enthalpy output of the plasma jet, suggesting such thermal improvements would be beneficial. Increasing central gas flow in a Fassel or conical torch would spread the plasma heating across a greater mass, leading to lower peak temperatures and electron densities. However, such devices also use weak central flows for plasma stability, thus an alternative flow regime is necessary to optimise for thermal efficiency and output enthalpy.

Reverse Vortex Flow

In 1998, Gutsol published an investigation of a novel gas flow regime, which he labelled the reverse vortex flow [64]. This regime is depicted in Figure 1.6, and, like the vortex flow discussed previously, involves injecting feed gas into a cylindrical plasma device tangentially along the wall in order to produce a swirling flow pattern. Unlike the typical vortex flow, however, the injector is located at the opposite end of the plasma source, near where the plasma is exhausted. This causes in the axially-centred recirculation region that is formed by the injected gas spiralling along the device walls to be aligned with the expelled plume. The hot recirculated plasma is thus blown out of the plasma forming region, in contrast to the forward vortex flow

regime, in which it is constrained by the top of the device and thus forced to mix with and heat freshly injected gas in direct contact with the device walls. Gutsol identified that this flow regime may offer significantly improved thermal efficiency compared to the forward vortex flow, and may be a useful alternative to Fassel-style sheath gas flows.

The initial investigation into the reverse vortex flow performed by Gutsol and collaborators were performed using a 3.5 kW microwave torch. This work showed that swapping a forward vortex for reverse vortex flow reduced heat loss to the walls, with the largest decreases dropping from ∼40% of input energy to ∼7% [64]. By 2001, Gutsol and collaborators had applied the method to a high-power RF ICP device [59]. They found that, for a constant 25kW input power, the thermal efficiency of the forward and reverse vortex flows are similar for low feed gas flow rates, but diverge as flow rate increases, with the reverse vortex flow increasing significantly more than its counterpart. For a flow rate of 3.2g/s the thermal efficiency of the reverse vortex was measured at 58%, while the forward vortex achieved only ∼40%. The reverse vortex efficiency also compares favourably to those simulated for a conical torch by Ebrahimi et. al., which for similar total flow rates and absorbed powers achieves 51% efficiency. This is primarily due to the reverse vortex flow having far smaller radiative losses, ∼10% of absorbed power compared to ∼38% for the conical torch.

In order for a reverse vortex flow to be established, a nozzle or throat is required between the plasma generation region and plume expansion chamber. This forces the feed gas to spiral upward instead of being swept downstream by the prevailing flow. It is therefore an appealing flow regime for applications that would otherwise already require a nozzle. In recent years Lafleur, Corr and Pascale have developed and characterised a 1kW RF ICP with a supersonic nozzle for use as an electrothermal thruster [65]. A comparative study [5] of the forward and reverse vortex flow regimes showed similar results to Gutsol et. al., with the reverse vortex producing higher stagnation temperatures and lower heat fluxes to the wall. Due to using a supersonic nozzle, however, a larger portion of absorbed power is lost to the walls compared to Gutsol's results. Pascale's initial study using a 2mm diameter nozzle exit reported heat loss between ∼65 and ∼99% of delivered power, depending on flow rate. A subsequent study comparing nozzle diameters saw a minimum heat loss of ∼30% for a 4mm diameter nozzle. These findings suggest a reverse vortex torch optimised for heating would benefit from a subsonic nozzle with the largest possible exit diameter to minimise heat losses to the wall.

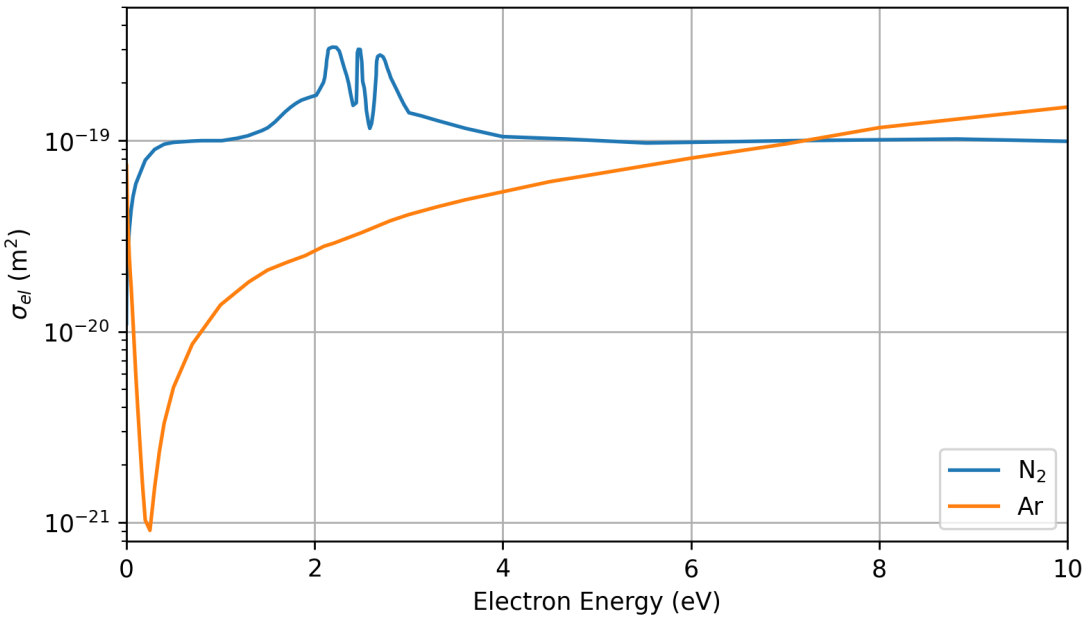

Figure 1.7: Electron-neutral elastic scattering cross sections against incident electron energy for nitrogen and argon. Nitrogen data from [6], Argon data from [7].

1.3 Nitrogen Plasma

Many plasma devices in both research and industrial applications use argon as a feed gas, particularly in inductively coupled plasma. Argon presents a range of benefits suited to plasma torches. As a noble gas it eliminates risk of chemical reaction with device walls, heating targets or trace atmospheric elements that may be present in the feed gas flow. As a monatomic gas does not undergo dissociation, leaving discharge energy available for ionisation and heating, and preventing potential instabilities arising from pressure fluctuations. It has low thermal conductivity compared to other atmospheric gases, which can be useful for minimising heat flux onto device walls.

The property of argon most relevant to plasma formation is its abnormally low elastic electron scattering cross section at low collision energies [7]. Figure 1.7 compares this cross section for argon and nitrogen, showing that for collisions below 2 eV, the effective cross section for argon is between 10 to 100 times smaller than that of nitrogen. This occurs in argon due to the Ramsauer-Townsend effect, a quantum phenomenon produced when the De Broglie wavelength of an incident electron is in harmonic resonance with the energy well created by the electric potential of an atom [66]. Such a resonance results in destructive interference of the electron wavefunctions scattered by interaction with the atom, meaning the resonant electron passes through the atom without depositing any energy. Therefore in a plasma

with electron temperatures on the order of 1 eV, which includes most high-pressure inductively coupled and microwave plasmas [67], operating with argon reduces the effective atom-electron collision rate. This allows electrons to be accelerated for longer intervals between collisions, causing them to reach higher speeds. These on-average more energetic electrons are then more likely to be involved in excitation or ionisation reactions, producing a greater population of metastable atoms, ions and free electrons than would otherwise be possible. Thus, using argon feed gas generally produces a higher electron density and temperature for a given input power and operating pressure.

As discussed in the previous section, the cost of argon gas can be a barrier for industrial application of inductively coupled plasma technology. This may be another contributor to the current dominance of arc discharge torches among plasma process heat applications, as the electron temperature within the core of an arc generally exceeds 10 eV, meaning nitrogen can offer higher electron densities than argon. Nitrogen, making up more than 71% of the atmosphere, is far cheaper to use in large quantities than argon and is therefore a desirable operating gas for industrial applications [68].

Despite its industrial applicability, research on inductively coupled plasma devices using exclusively nitrogen as a feed gas is limited. Nitrogen appears extensively in the literature as a swirl or sheath gas in Fassel torches, while the central flow uses another gas, typically argon [69]. Lower electron densities result in difficulty igniting nitrogen plasma at high pressures, which likely contributes to this gap in the research. Using a mixture of argon and nitrogen allows a pure argon flow to be used for ignition, before the flow mixture is gradually shifted toward nitrogen while the discharge is maintained. In 1985, Meyer et. al. [70] extended this procedure to study pure nitrogen and air ICPs for applicability to optical emission spectrometry, though the high flows of argon needed to ignite the discharge and transition it to nitrogen likely limited future interest in such applications. Unlike in spectrometry, many process heat applications operate continuously for extended time periods and so can accommodate longer ignition procedures. Further investigation of the thermal behaviour of inductively coupled discharges operating with only nitrogen feed gas is therefore necessary to evaluate ICPs as a potential transition technology for process heat generation.

1.3.1 Nitrogen Emission Spectrum

Examination of the thermal properties of a nitrogen plasma is assisted by its molecular structure. As a diatomic molecule, nitrogen can be excited into rotational and

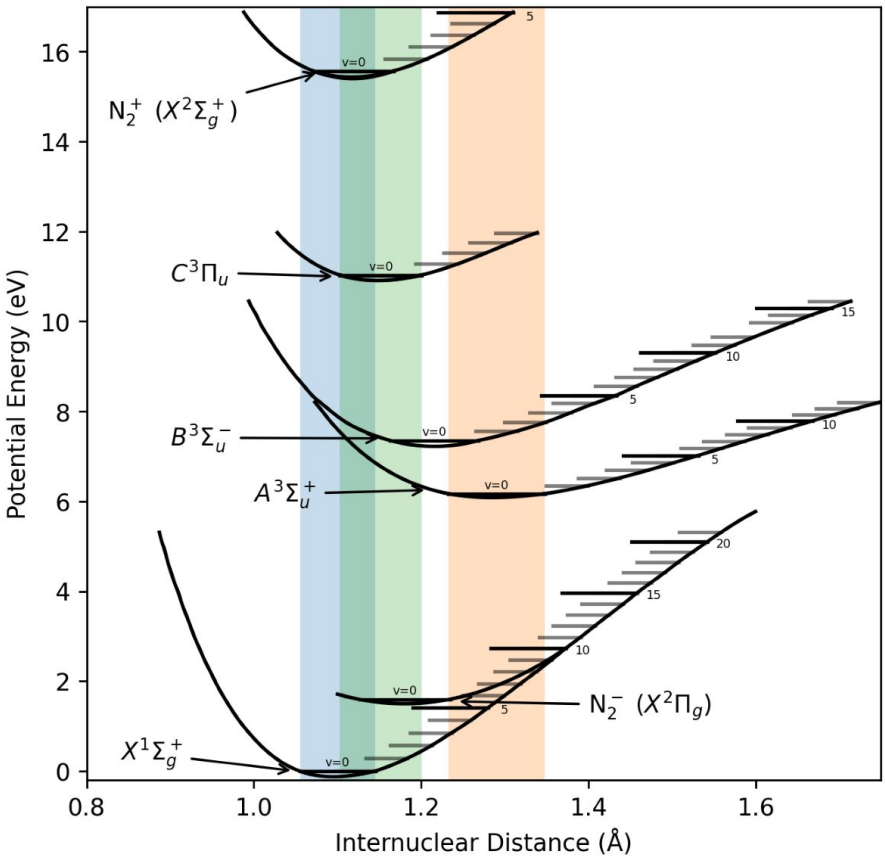

Figure 1.8: Potential energy curves of several relevant states of the N_2 molecule. Highlighted areas indicate the internuclear distance range of the N_2(X) ground state (blue), N_2(C) excited state (green), and N_2(A) excited state (orange). Plotted using RKR potential curves from Ref.[8] and an approximation to the N_2^- (X) curve described in Ref.[9].

vibrational modes, which store predictable, quantised amounts of energy. These energies are smaller than those corresponding to electronic excitation, adding finer structure to the allowed energies particles can exhibit compared to single atoms, which are limited only to metastable electronic states [71]. Figure 1.8 shows the electronic and vibrational levels accessible to nitrogen molecules against internuclear distance. Rotational energy levels are separated by small energy steps, and are thus not shown for clarity. When molecules transition between electronic excited states, the amount of energy released as light is determined in part by its initial and final rotational and vibrational states. As the energy of a photon determines its wavelength, this results in electronic transitions appearing in molecular emission spectra as detailed structures spanning significant wavelength ranges, instead of single peaks as they do in atomic emission spectra. This comparative abundance of detail is visible in Figure 1.9, which shows a roughly 400 nm wide section of the emission spectra of both nitrogen and argon .

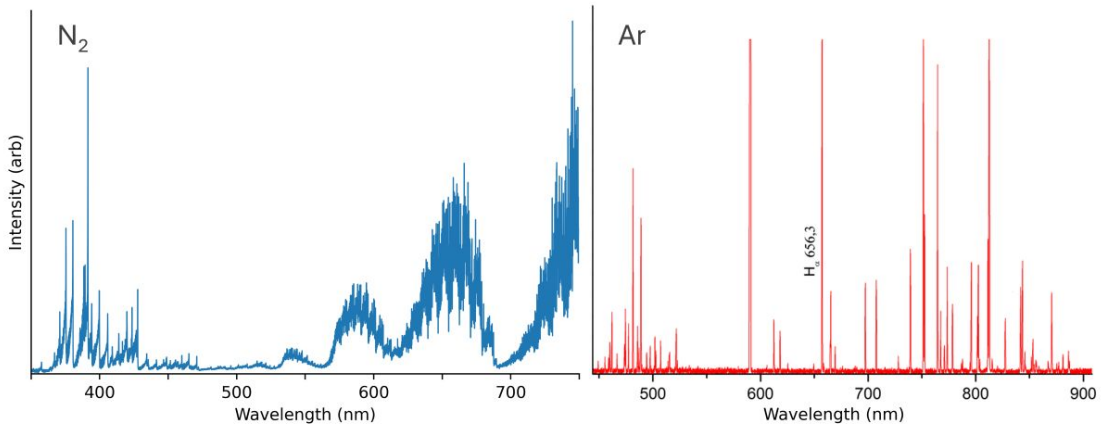

Figure 1.9: Example emission spectra for molecular nitrogen (left) and argon (right). An additional line in the argon spectrum originating from hydrogen is labelled. Argon spectrum from [10].

The transition probabilities between ro-vibrational energy levels can be calculated or deduced experimentally, allowing the relative heights of peaks within emission bands corresponding to a single electronic transition to be used to determine the rotational and vibrational population distributions of the upper state [72]. In most cases these distributions are Maxwellian and thus provide values for the rotational and vibrational temperature of the upper state. In nitrogen, the rotational mode is strongly coupled to the translational mode though collisions, meaning a rotationally excited molecule will return to rotational and translational equilibrium with the rest of the population after very few collisions [73]. As a result, at all but the lowest pressures, the translational and rotational temperatures of the ground state and all excited states will be equal, making the measurement of the excited state rotational temperature from the emission spectrum a valid measurement for the overall gas temperature of the discharge.

Determination of the gas temperature of plasma using the nitrogen emission spectrum is widely employed in the literature. Trace amounts of nitrogen is commonly added to argon feed gas flows, minimally changing plasma behaviour while adding molecular nitrogen rotation bands to the emission spectrum which can be used to determine the gas temperature [74]. This is a particularly common practice in investigations of low-power or low-pressure inductively coupled plasma devices which produce non-thermal or near-thermal plasma [75]. Temperatures of pure nitrogen plasmas are also commonly determined using nitrogen emission. The second positive system, produced by the electronic transition between the third and second excited states ($N_2(C) \rightarrow N_2(B) + h\nu$), is most commonly used, followed by the first positive system ($N_2(B) \rightarrow N_2(A) + h\nu$) [73]. Temperature determinations can be

made using a linear fit to a Boltzmann plot generated from the measured values of peaks against the corresponding transition energy [76], or by fitting the experimental spectra to simulated spectra generated from spectral databases [77]. In the latter case Specair, a proprietary spectral simulation and fitting program, is often employed [78–81].

Vibrational Distribution

Unlike rotational energy, which flows rapidly between nitrogen molecules by way of translational energy, vibrational energy is much slower to equilibrate. Both vibration-vibration (V-V) and vibration-translation (V-T) coupling are weak for collisions between nitrogen molecules, due to the restricted incident angles and timing required for a collision to transfer the oscillating motion of a bonded nitrogen atom into another molecule [82]. Even at gas temperatures over 15 000K, where characteristic vibrational relaxation times are more than 10^4 times shorter than at ∼1000K, equilibration of vibrational and rotation/translation temperatures can require more than 100 collisions [83]. Therefore in most laboratory-scale plasma devices, the vibrational temperature of an excited state will not equilibrate with that of the ground state or with the overall gas temperature before the molecule undergoes radiative decay. The vibrational temperature determined from emission spectra is thus applicable only to the upper state of the examined transition. The vibrational distribution of this state can, however, yield information on the excitation mechanisms prevalent in the plasma, which can correlate to vibrational distributions of other excited states.

Non-Boltzmann vibrational distributions of the $N_2(C)$ state have been observed in second positive system emissions of nitrogen plasmas. Initially identified in the afterglow of pulsed discharges [13], this behaviour has more recently also been observed under some discharge conditions [76]. Such distributions show an apparent underpopulation of the vibrational ground state, and in some cases even population inversion of the ground and v=1 levels. Initial explanations focused on two competing excitation processes producing the $N_2(C)$ state, direct excitation from the ground state by electron collision ($N_2(X) + e^- \rightarrow N_2(C) + e^-$) and energy pooling through collisions between molecules in the first excited state ($N_2(A) + N_2(A) \rightarrow N_2(C) + N_2(X)$) [84].

Due to the Franck-Condon principle, valid electronic transitions require constant internuclear distance, meaning allowed transitions appear on plots like Figure 1.8 as vertical lines [85]. As the ground and $N_2(C)$ states have similar internuclear distances, electron excitation of the ground state will produce $N_2(C)$ molecules with

a similar vibrational distribution [86]. In non-thermal discharges electron temperatures are typically high enough to ensure this is the dominant production pathway, resulting in Boltzmann-like vibrational distributions [13]. The $N_2(A)$ state has typical internuclear distances larger than those of the $N_2(C)$ state, causing the vibrational distribution of molecules produced by energy pooling collisions to be skewed toward higher vibrational levels, which exhibit larger internuclear distance ranges and thus greater overlap with those of the $N_2(A)$ state.

Models using only these two pathways were able to recreate population inversion of the first two vibrational levels, but could not accurately fit experimentally observed vibration distributions. Work by De Benedictis and Dilecce showed that including excitation of the first excited state by electron collision ($N_2(A) + e^- \rightarrow N_2(C) + e^-$) is required to accurately model experimental data, as it is likely the dominant $N_2(C)$ production pathway in many non-equilibrium afterglow conditions [13]. Such conditions may be encountered in an expanding plasma plume. These findings suggest that measurement of the vibrational temperature and distribution of the $N_2(C)$ excited state, while not immediately applicable to other states of nitrogen, can serve as an indicator of underlying plasma dynamics. These include $N_2(A)$ state production rates and equilibration of electron and vibrational temperatures.

1.4 Thesis Goals and Outline

This thesis presents the development and characterisation of a 1 kW inductively coupled plasma source that operates using nitrogen feed gas, injected in a reverse vortex configuration, at pressures up to 0.5 atm. The characterisation focuses on the thermal properties of the plasma, both in the source and the expelled plume, for flow rates between 2.5 and 12.5 slpm across varying pressures. Such properties were primarily measured using optical emission spectrometry, targeting segments of the second positive and first negative emission systems to capture ro-vibrational structures emitted by the $N_2(C)$ and $N_2^+(B)$ states. Temperatures fittings of the captured spectra were performed, providing gas temperatures and vibrational distributions. Independently determined temperature values allowed an existing global model of an inductively coupled argon discharge to be adapted for nitrogen plasma. Experimentally determined temperatures were combined with measurements of source pressure and coil current to inform a global model of the discharge, allowing evaluation of electron temperature and density under the coil.

Chapter 2 describes the plasma source and the motivations involved in its development process. The device dimensions, power coupling and typical operating pro-

cedure are detailed. Measurement techniques and their experimental set-up is discussed, including the optical emission spectrometry set-up, calibration and fitting procedures.

Chapter 3 reports neutral gas densities and collision frequencies in the source region and plume and assesses the conditions for which $N_2(C)$ rotational temperatures equilibrate with neutral gas temperatures. The neutral gas temperatures are subsequently reported for the source region and plume. Following this, $N_2(C)$ vibrational population distributions are reported and the implications for the underlying plasma chemistry are examined. The corresponding vibrational temperatures are presented. $N_2^+(B)$ state temperature results are reported and contrasted with $N_2(C)$ temperatures. Cooling water temperature measurements, serving as a proxy for heat flux to the walls, are presented and used to assess the insulative effect of the reverse vortex flow. Evidence of equilibration between vibrational and translational temperatures of the neutral gas is evaluated using enthalpies calculated for each energy mode. Finally, calculated estimates of thermal efficiency are reported and used to assess the overall thermal performance of the device.

Chapter 4 first describes the analytical model used to calculate electron temperatures. Following this, the procedure for using this temperature to solve for electron density is detailed. These parameters are presented for all examined discharge conditions. Next, measurements of power transfer efficiency are detailed and discussed with reference to the determined skin depth. Trends in electron density with respect to pressure and flow rates are compared to those of neutral gas temperatures to explore the correlation between plasma dynamics and thermal conditions. Finally, measurements of oscillations observed in plasma parameters at higher pressures leading to discharge instability are presented and a production mechanism proposed.

Chapter 5 concludes this work with an overview of findings and commentary on possible directions for future research.

Chapter 2

Experimental Design and Methodology

In the previous chapter it was established that radio-frequency inductively coupled thermal plasma technology shows promise as a high-temperature heat source in industrial applications. The use of nitrogen as a feed gas in these applications could offer advantageous thermal behaviour and electrical efficiencies when compared to argon. For these reasons the goal of this project was to develop a low power RF-ICP torch capable of operation using nitrogen at sufficiently high pressures to generate and output thermal or near-thermal plasma. This chapter first details considerations that went into the design of the device and its operational configuration. Next, the diagnostic tools used to measure its electronic performance are described. Finally, the optical emission spectrometry methods used to characterise the thermal performance of the device are examined.

2.1 Plasma Torch Design

In previous work from the Experimental Plasma Science Group at the ANU, a low-cost inductively coupled plasma source was developed for use in space propulsion [65]. This design was iterated upon and improved over several years [5, 11]. Due to its proven performance and the immediate availability of both designs and parts, it was used as the basis of the device developed for this work. This section first describes the plasma source studied in this work. Next, the choice of power supply frequency is examined, noting the changes made compared to similar previous devices to optimise it for operation with nitrogen.

2.1.1 Plasma Source

Figure 2.1 shows a schematic representation of the device plasma source. Two concentric alumina dielectric tubes are held between two grounded aluminium end

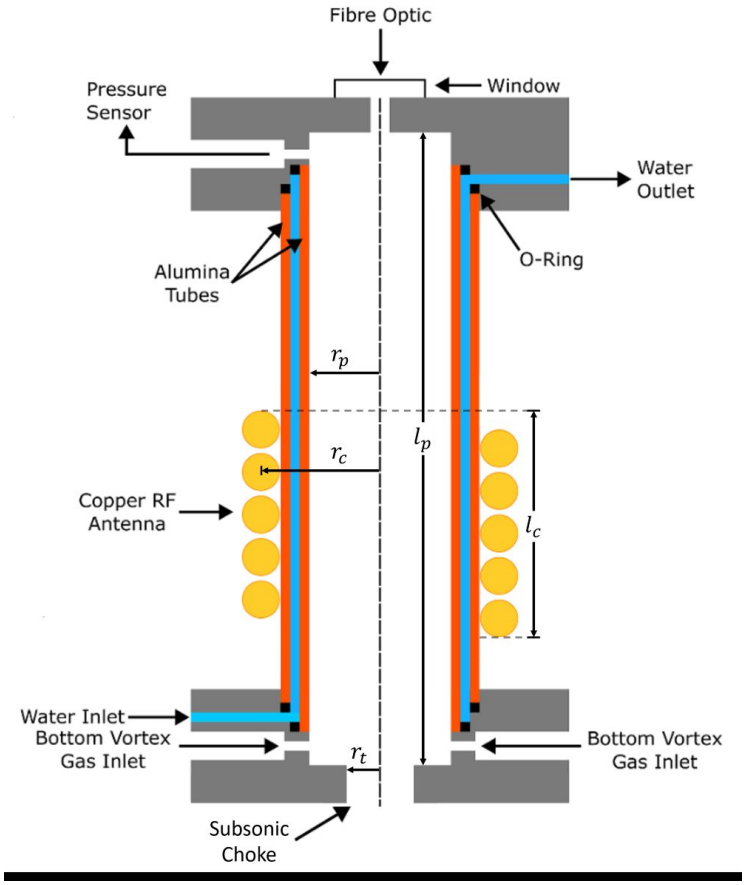

Figure 2.1: Schematic cross-section of the device source region. Key parameters of the discharge geometry are labelled, with the lengths used in this work provided in Table 2.1. Figure adapted from [11].

caps. A copper coil with five turns is wrapped around the outer dielectric tube and connects to an RF power supply. Water is supplied to an inlet in the lower end cap, where it flows between the two dielectric tubes before expelling from the top cap. This serves to cool the inner plasma-facing walls. The lower cap also hosts four gas inlets, angled tangentially to the interior wall of the inner tube, through which the plasma feed gas is supplied. Four similarly angled gas inlets are also present on the top cap, though in this work three were unused and thus blocked by solid fittings, while the remaining inlet hosts a pressure sensor. A sapphire-glass window in a KF-25 fitting is mounted to an axially-aligned circular recess of the same diameter at the top of the device, providing optical access to the plasma forming region via a 19 mm diameter portal in the upper cap. The entire source sits atop a vacuum chamber, expelling plasma through the device throat- an axially aligned circular hole in the lower cap with a radius smaller than the inner dielectric tube.

Using tangential gas injection and a throat radius smaller than that of the inner walls is necessary for establishing a reverse vortex flow in the plasma forming region. As

Parameter	Length (mm)
r_p	9.5
r_c	16.25
r_T	5
l_p	105
l_c	35

Table 2.1: Values used in this work for key parameters of the source region geometry presented in Figure 2.1.

discussed in Section 1.2.2, such a flow allows incoming feed gas to also operate as a sheath gas, helping to insulate the inner wall from the hot plasma bulk and thus reduce convective heat losses in the device.

2.1.2 Power Supply Frequency

In Section 1.3 the collision cross section of molecular nitrogen is compared with that of argon and shown to be as much as two orders of magnitude larger in the 0-6 eV range. Due to this difference, electron-neutral collisions that transfer energy into the feed gas are significantly more frequent in nitrogen plasma than in argon for the same temperature and pressure conditions. As a result, the electron mean-free-path- the distance travelled by an electron on average before a collision- is lower in nitrogen. The effective resistivity of a nitrogen plasma will therefore be higher than that of an argon plasma of the same electron density. To screen out the external electric fields of the coil and thus couple energy out of them and into the plasma, an azimuthal current must flow through the plasma. The magnitude of this current is determined by the geometry of the antenna and plasma and is independent of the feed gas used. Therefore, by $P = I^2R$, higher powers would be required for the same current to flow through higher resistivity nitrogen plasma compared to argon plasma. The geometry of the source and antenna are unchanged from previous iterations of the device operated with argon, suggesting higher powers are necessary to achieve similar power transfer efficiencies in the device using nitrogen.

To mitigate the impact that changing feed gases has on required power, the frequency of the AC power supplied to the coil can be increased. This increases the effective reactance of the coil and plasma load, as the reactance of a circuit with inductance L is given by $X_L = 2\pi fL$. As a result the Q factor of the coil, given by $Q = X_L/R$ where R is the DC resistance of the coil, increases with frequency. A coil with a higher Q factor more efficiently converts between energy stored in magnetic fields within the inductor and current flowing through it than those with lower Q factors. As power is delivered to a plasma in inductive mode via such magnetic fields,

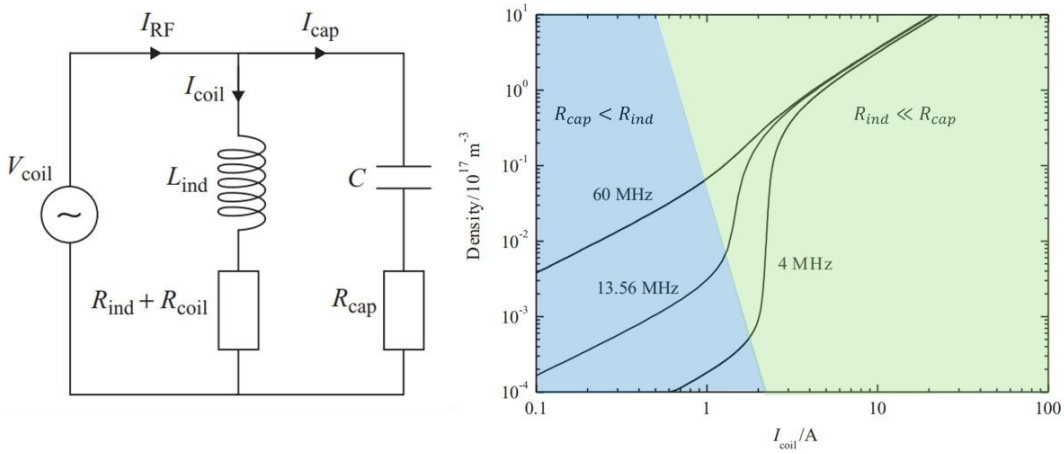

Figure 2.2: Left: Circuit diagram model of an RF discharge, showing the inductive and capacitive modes in parallel. Right: Modelled electron density of a low-pressure inductive discharge against coil current. Higher driving frequencies produce higher electron densities when the capacitive mode dominates the discharge. Figures adapted from [12].

increasing the Q factor therefore increases energy transfer efficiency into the plasma [12]. As the transition to nitrogen feed gas would already increase the thermal load on the walls compared to known performance in argon for a given operating power, operating at higher powers than previous experiments risked necessitating a redesign of the device geometry. Thus, it was decided to increase the frequency of the supplied power from 13.56 MHz, which was used in all prior experiments with argon, up to 27.12 MHz, while maintaining the maximum operating power of 1 kW.

Increasing the frequency of the current driving the coil fields has an additional benefit of facilitating easier plasma ignition compared to lower frequencies. This results from the reactance of a capacitor being inversely proportional to frequency, $X_C = \frac{1}{2\pi f C}$. Low electron densities, like those present when attempting to ignite the plasma, cannot support high induced currents and thus experience weak coupling to the inductive mode. In such conditions a lower capacitive reactance leads to a lower impedance for the capacitive branch of the circuit, encouraging a greater share of I_{RF} to flow through it. This results in a greater share of the power deposition in the capacitive branch occurring within the plasma (R_{cap}) rather than in the capacitor itself. The result of this is evident in the plot included in Figure 2.2, which shows that at low coil currents (ie. low input powers), where capacitive coupling is dominant, higher electron densities are achieved when higher power supply frequencies are used. These higher electron densities lower the resistivity of the plasma, allowing the transition into the inductive mode to occur at lower applied powers. This improved capacitive coupling allows for the device developed in this work to ignite nitrogen

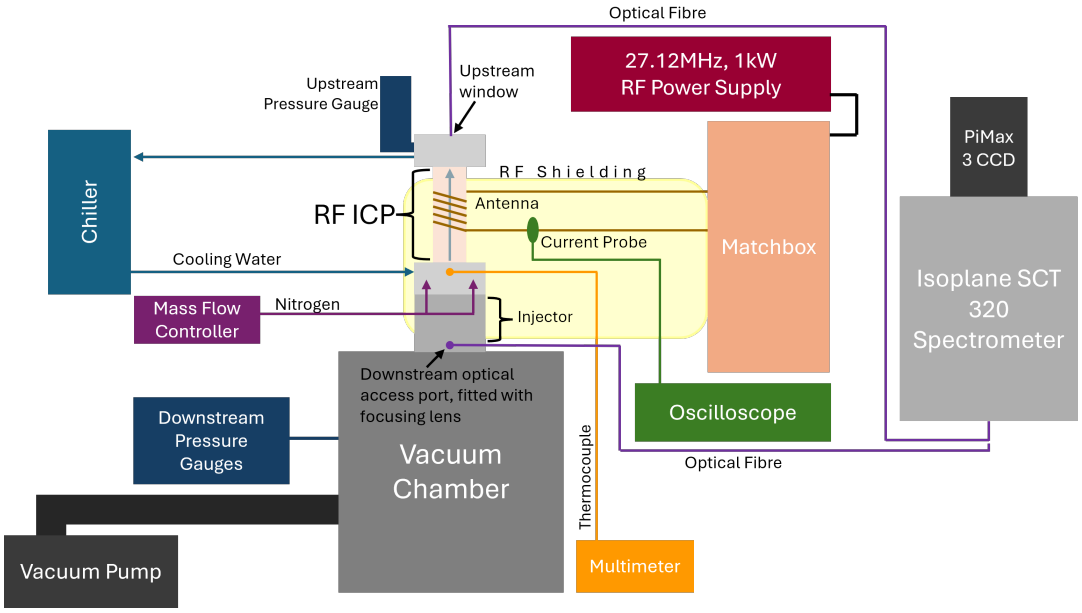

Figure 2.3: Schematic diagram of the experimental set-up.

plasma at similar pressures and input powers as argon plasma is ignited in 13.56 MHz devices with the same geometry, despite nitrogen plasmas experiencing higher energy losses and thus lower electron densities.

2.2 Experimental Set-up

This section provides a detailed overview of the experimental set-up used to operate and test the plasma device. This is followed by an examination of the matching network, in which results of modelling performed to determine the necessary components is provided.

2.2.1 Overview

A schematic view of the experimental set-up is shown in Figure 2.3. A Coaxial Power Systems RFG-1K-27 1000 W, 27.12 MHz power supply produces a voltage that drives a current through the 5-turn coil made of 1/8" (3.125 mm) diameter copper wire. This current runs via a matching network, which is detailed in the following section. To limit arcing observed between the coil and outer alumina tube, a layer of teflon 2 mm thick is placed between them. The low-voltage arm of the coil runs through a Pearson Electronics model 7427A current monitor before entering the matchbox. Feed gas is supplied via a Kofloc 8750MC-O mass flow controller calibrated for nitrogen gas. The output of the mass flow controller is split four ways, each connecting to one of the four gas injection inlets of the bottom cap.

Pressure in the source is measured by a gauge mounted to an elbow joint fitted into one of the gas inlets of the top cap.

RF shielding, consisting of a sheet of metal mesh and sections of aluminium foil, encircles the space between the matchbox and plasma source to limit emissions from the antenna. This is necessary to minimise emanation of EM fields produced by the antenna, which would otherwise produce stray voltages that can impact readings from the current probe and pressure gauges or cause the mass flow rate to fluctuate. Additional aluminium foil surrounds the oscilloscope, pressure gauges and the cables connecting them to their readers in order to further limit the risk of interference. These pressure readers, the mass flow controller and the RF power supply are placed in a grounded metal cabinet to further shield from interference from the coil.

Cooling water is supplied by an SMC HRS012-A-20 thermo chiller. The chiller provides up to 7 litres of water per minute, which first runs into the lower cap of the plasma source, travels up between the two alumina tubes and exits from the top cap. The water then runs through the hollow coil wire, entering along the top arm and exiting from the bottom before returning to the chiller to be cooled. For all discharges studied the target temperature of the chiller is set to 25°C and the output temperature reported by the in-built thermometer is recorded.

The plasma source sits atop a prototype gas injector, also made of aluminium, which was developed to study the thermal behaviour of the plume and the impact of mixing it with cold gas flows downstream. Such experiments proved to be beyond the scope of this work, however, and the gas inlets were unused in the experiments detailed in this thesis. This injector was nonetheless vital for studying the plume as a 5 mm diameter portal on the plasma-facing wall provides optical access transversely across the injector. This access port is located $\sim$1 cm below the bottom of the source region throat, allowing imaging of the recombining plasma present in the plume. The internal diameter of the injector matches that of the inner alumina wall in the source, and at the downstream end another throat of the same diameter as in the source is present. Unlike the source region, the injector is not water-cooled and instead relies on conductive heat losses to the water-cooled end cap or the high thermal mass vacuum chamber to prevent overheating. Temperature of the component is monitored using a thermocouple placed in a slot in the outer wall, 2 mm in diameter and 12 mm deep. This allows the measurement to better reflect the temperature of the plasma-facing walls. A similar slot is present on the bottom cap of the plasma source.

Both the plasma source and injector sit atop a 6-faced vacuum chamber. Plasma is expelled from the injector through a 10 mm diameter throat. Two steel rods with

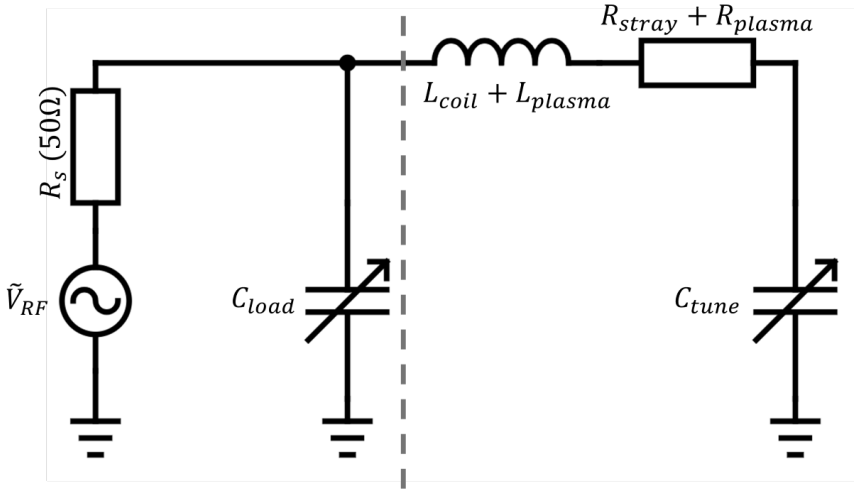

Figure 2.4: Circuit diagram of the modified Pi-type matching network.

threaded ends are mounted on either side of the source-injector assembly, running through an aluminium cross bar that sits across the top of the top cap. Nuts atop the rods are tightened to press down on this crossbar, applying a downward force that both attaches source-injector assembly to the vacuum chamber and causes the various O-rings in the assembly to expand and seal, preventing atmospheric infiltration. A 25 mm diameter hole in the crossbar maintains optical access to the plasma through the upstream window.

Several KF-25 attachment points are present on a vertical face of the vacuum chamber, one of which hosts a T-piece onto which two pressure gauges are mounted. The same face also hosts the connection to an Edwards nXDS20i roughing/backing pump. The pump is capable of pumping rates up to 22 m^3/hour, and is able to reduce the background pressure of the chamber and ICP assembly to below 40 millitorr. A gate valve and two ball valves are connected along the line between the pump and vacuum chamber. The gate valve isolates the pump from the chamber, allowing adjustments or maintenance to be performed on the device without shutting down the pump. The two ball valves can be adjusted to constrict flow out of the vacuum chamber, and are used to control the pressure present within the device.

2.2.2 Matching Network

Figure 2.4 shows a circuit diagram of the matching network employed in this device. It is an adaption of the widely-used Pi-type network, which uses an inductor and two variable capacitors to match a variable load resistance to a steady source resistance. Compared to the typical Pi-type network, that employed here places the resistive load in series with both the inductor and load capacitor, rather than in series with

the former and parallel to the latter. This is because the antenna coil is used as the inductor of the matching network, which removes the need for an additional resistive component in the circuit, minimising the power lost in the matchbox rather than in the plasma.

Prior to assembling the matchbox, it was necessary to determine the capacitance ranges of the variable capacitors required to match the plasma impedance to the 50 Ω output of the power supply. A simplified electromagnetic model of an inductively coupled plasma is developed in Ref. [12], which provides expressions for the resistance and inductance of the plasma. Such expressions were also later used to develop a global model of the discharge, which is detailed in Section 4.1 of the following chapter. To avoid repetition, they are not presented here. Using these expressions the resistance of the plasma (R_{plasma}) and the inductance of both the plasma and coil ($L_{ind} = L_{coil} + L_{plasma}$) can be expressed as a function of electron density (n_e), given known values for the plasma parameters electron temperature, neutral gas density and electron momentum-transfer collision rate. In the global model, these values are determined using experimental data which was not available prior to device assembly. Thus, to model the matchbox, some assumptions were made. An electron temperature of 1 eV was assumed, based on global model results [65] and measured excitation temperatures [5] for similar devices. Gas density was determined using the ideal gas law for pressures of 10 Torr and temperatures of 300 K, as these conditions approximate those at which the plasma is ignited. Finally the electron momentum-transfer collision rate was calculated considering only an estimate of the elastic collision cross sections, as these cross sections are at least an order of magnitude larger than those of other collision types for both nitrogen [6] and argon [7] at incident energies of 1 eV. These cross sections were estimated as 10^{-19} and 10^{-20} m^2 respectively. Substituting these values into Equations 4.6-4.9, R_{plasma} and L_{ind} could be calculated for a given electron density.

Examining Figure 2.4 shows a value of R_{stray} is required before matching capacitances can be solved for. This resistance corresponds to that of the coil and matchbox with no plasma present. This was measured to be 0.6 Ω in the 13.56 MHz device of Ref. [5]. Given that the impedance of a capacitor decreases with increasing frequency, R_{stray} of this device at 27.12 MHz was estimated as 0.4 Ω. Once the device was assembled, this assumption was validated by measurements of R_{stray} falling between 0.35 and 0.375 Ω.

With values for the load resistance and inductance determined, expressions for the capacitances required for matching can be derived by equating the admittances of the circuit components on either side of the dashed line in Figure 2.4, in line with

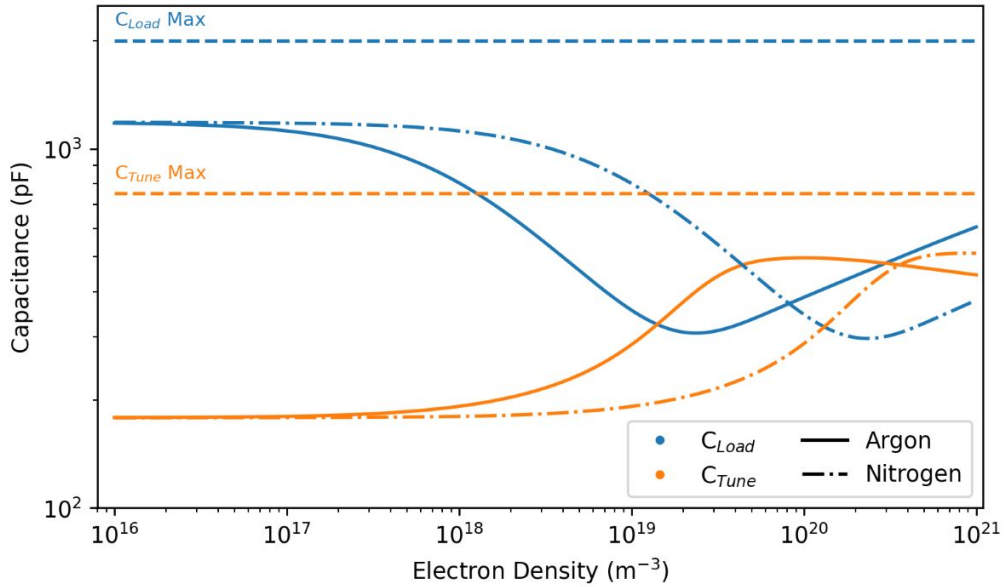

Figure 2.5: Matchbox model results showing capacitance required for perfect matching against discharge electron density for discharges in argon and nitrogen. Dashed lines indicate the maximum capacitances of the variable capacitors selected.

the method outlined in Section 6.3 of Ref. [87]. These expressions were evaluated for electron densities between 10^{16} and 10^{21} m^{-3} and are presented in Figure 2.5. The range of capacitances required for matching is similar between the two examined feed gases, with nitrogen following a very similar curve to that of argon, simply offset toward higher electron densities. This aligns with a given electron density corresponding to greater skin depths in nitrogen compared to argon. Dashed lines indicate the maximum capacitance of the variable capacitors selected for the matchbox, which were chosen such that a comfortable margin is left between it and the highest matching capacitance predicted by the model. Both exhibit a minimum capacitance of 50 pF, well below the lowest modelled values.

With the necessary ranges of capacitance identified, the matchbox was assembled. A Menivac SCV 520-M 5 kV 2000 pF variable capacitor was selected for the load capacitor and a Comet CVIC-750 15 kV 750 pF variable capacitor for the tune. These were mounted in a copper box with a small opening in one face to allow a connection between the coil and the capacitors. An N-type 50 Ω cable carrying current from the power supply connects to an electronically isolated socket on the exterior of the device. A copper bracket soldered onto the interior-facing socket component delivers this current to the top of the load capacitor. Copper arms connected to the tops of each capacitor extend out of the aforementioned opening in the matchbox, onto which the coil arms are affixed using a copper saddle clip. This mounting arrangement allows the coil to close the matchbox circuit while leaving

the ends of its arms free to host fittings that connect the coil to the water-cooling system.

2.3 Diagnostics

This section details the diagnostic tools employed to examine the thermal behaviour and plasma parameters of discharges generated in the device. The methods relying on principles other than optical emission from the plasma, namely measurements of pressure and coil current, are described first. Following this, the optical diagnostic methods are detailed. This includes both the optical emission spectrometry set-up used to capture plasma spectra, as well as that of time-resolved measurements of source region emission intensities.

2.3.1 Non-Optical Diagnostics

Pressure

A Vacuum Research diaphragm manometer pressure gauge, capable of operating between 0.5 and 1500 Torr, measures the pressure in the source region of the device during operation. The two downstream pressure gauges consist of a Thyracont VSC43MV piezoresistive sensor and a Pfeiffer Vacuum TPR pirani gauge. The former uses a reader and operates between 10^{-3} and 100 mbar. It is used to determine the minimum pressure the device can achieve, which is necessary for detecting and fixing leaks that would otherwise allow cooling water or air to enter the plasma region. The latter uses a Thyracont VD12 reader and operates between 0.75 and 1050 Torr. It is used to measure the downstream chamber pressure during operation.

Electrical Measurements

The current through the coil is measured using a Pearson Electronics model 7427A current monitor, connected to a Aligent Technologies DSO-X 2014A digital oscilloscope via BNC cable. The voltage output of the probe read at the oscilloscope using an input resistance of 1 MΩ and converted to current using the 0.01 V/A measurement ratio specified by the manufacturer. The peak-to-peak measurement of this signal is equal to $2I_{coil}$, where I_{coil} is the peak current through the coil. In an AC circuit, the peak current through a component is a factor of $\sqrt{2}$ larger than the time-averaged current. Net power delivered to the plasma is given by the difference between forward (P_f) and reflected (P_r) power, both of which are reported

by the RF generator. Combining these two measurements allows the total effective resistance of the system (R_{eff}) to be determined:

$$P_f - P_r = \frac{1}{2} I_{coil}^2 R_{eff} \tag{2.1}$$

As R_{eff} is the sum of the resistance of the plasma (R_p) and that of the antenna and matching network (R_{vac}), measuring the effective resistance of the system under plasma-free conditions allows for R_{vac} to be determined and subtracted from later R_{eff} measurements to determine R_p. Before each run of measurements, a flow rate of 15 slpm was used to increase the pressure in the source while I_{coil} was measured for 40, 50, and 60 W net delivered powers. These conditions prevent plasma ignition, allowing the average of the corresponding resistances to be taken as measurements of R_{vac}. Subsequent measurements of R_{eff} with plasma present can then be used to determine the power transfer efficiency (η_{rf}, given by the ratio of plasma resistance to total system resistance:

$$\eta_{rf} = \frac{R_p}{R_{eff}} = \frac{R_{eff} - R_{vac}}{R_{eff}} \tag{2.2}$$

2.3.2 Optical Diagnostics

As outlined in Section 2.2.1, the device was designed with two optical access ports: one at the top of the source region allowing imaging of the peak plasma heating region along the torch axis, and another in the downstream injector region angled across the diameter of the device, allowing imaging of the plume 1 cm downstream of the bottom of the end cap. Both of these ports host a sapphire window, a material often utilised in optical systems due to its high transmittance of UV, visible and infrared light. An appropriately sized notch in the upper face of top cap hosts a KF-25 fitting with a central 20 mm diameter sapphire window for the upstream optical access. For the downstream access, the walls of the port nearer the injector exterior are threaded, allowing a screwed fitting with a KF-16 adaptor to be mounted. A corresponding fitting with a 20 mm diameter sapphire window is attached.

Optical fibre is used to carry light emitted at these optical windows to measuring devices. For the upstream window, the fibre is secured by Thorlabs CP02/M holder with a threaded metal adaptor which is positioned centrally atop the crossbar securing the torch to the vacuum chamber. The intensity of the source region emissions means lensing is not required for strong signals to be measured. This is not the case for the downstream optical access port, which has a smaller diameter and looks onto a dimmer region of plasma. For imaging through this port, the fibre is connected

to an optical fibre holder with a built-in 15 mm diameter lens which is held against the sapphire window using a retort stand. Using these fibres, light captured at these windows are carried to one of two measuring devices: a spectrometer and CCD for optical emission spectrometry, or a photo-diode and oscilloscope for time-resolved intensity measurements.

Optical Emission Spectrometry

Light emitted from the active plasma was channelled into a Princeton Instruments Isoplane SCT 320 spectrometer, with a focal length of 320 mm and slit width of 17 μm. The light was diffracted using a holographic grating with 2400 grooves per mm before being captured by a Princeton Instruments PiMax 3 CCD. consisting of 1024 $\times$ 1024 12.8 μm wide pixels. The system's slit function had a full width at half maximum of 0.12 nm. The spectra captured by this set-up spanned $\sim$13 nm with a resolution of $\sim$0.013 nm per pixel. Both devices were controlled using a PC running Princeton Instrument's Lightfield application, which also received and processed data outputted by the camera.

Wavelength calibration of the spectrometer was performed using the mercury lamp of a Princeton Instruments Intellical USB light source. The in-built calibration process in the Lightfield software was used with a custom peak selection of the 365.0 and 435.8 nm lines. These peaks were selected as they span the portions of the First Negative and Second Positive emission systems of interest in this work while being within $\sim$13 nm of other peaks, which allows the calibration program to more accurately measure and correct for dispersion within the range captured in a single spectrum. As the Isoplane rotates the grating every time it is powered on or off, this calibration was performed every time the spectrometer was powered on to maintain accurate alignment.

Relative intensity calibrations across the examined wavelength ranges were performed to correct for wavelength-dependant variations in optical efficiency present in the components used in this set-up. These calibrations were performed using the Avantes AvaLight Hal-Cal-Mini lamp, a halogen calibration lamp with a known emission intensity curve. The optical fibres used for both windows were connected to a cosine-corrector mounted within the lamp, which ensured all of the emitted light passed into the fibre with the same phase. This light is then passed through the Isoplane, which is set to examine an experimentally-relevant wavelength range, and imaged by the CCD. The resulting observed emission intensity curve can be compared to the known emission curve of the lamp to find a wavelength-dependant correction factor for each data point. Interpolating these factors provides a relative

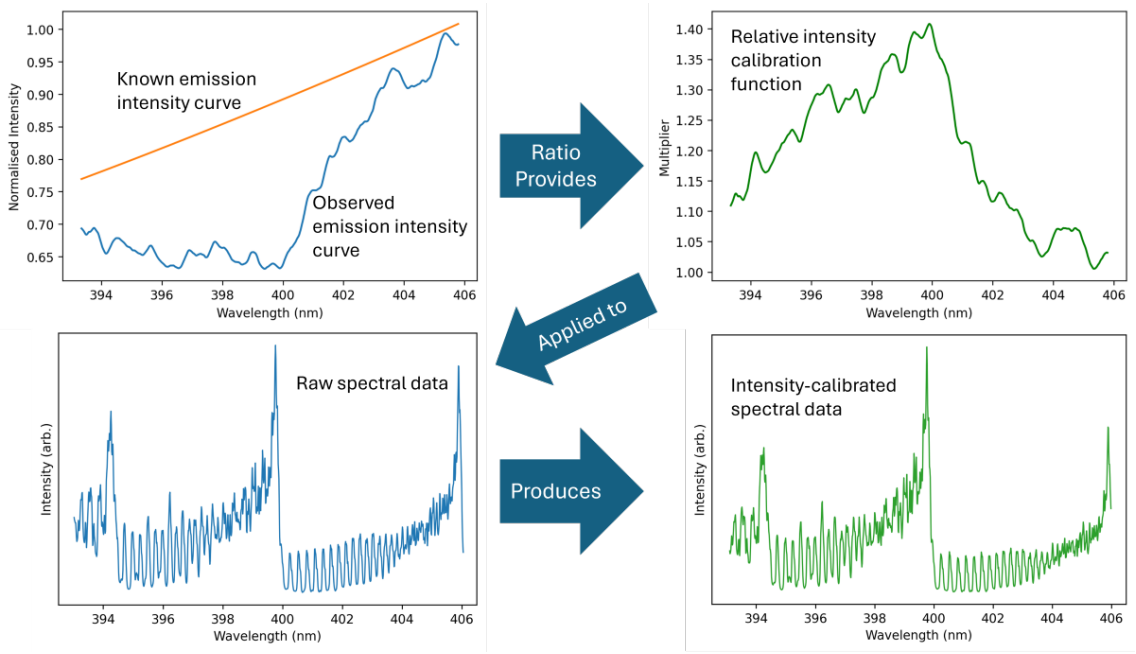

Figure 2.6: Relative intensity calibration procedure with example curves for the wavelength region centred on ∼400 nm. Experimental spectrum captured in the source region of a 950 W, 5 slpm discharge at 9 Torr.

intensity calibration function that can then be applied to experimental spectra to correct for the instrument function. This process is shown in Figure 2.6 for the wavelength range centred around 399.8 nm. These calibrations were performed for both of the wavelength regions examined, using the optical fibres leading to both the upstream and downstream windows.

To maintain the validity of these calibrations, the intensifier setting of the CCD was kept constant across calibration measurements and experimental captures from the same optical access window. These values were 15x for upstream captures and 100x for downstream captures. On-CCD accumulations, the number of times the CCD is exposed before data is read off of it, was also held constant for each window, at 15 and 5 for the upstream and downstream respectively. The only value varied between captures was the gate-width, or the time for each exposure, in order to ensure a sufficient photon count is measured to maximise the signal-to-noise ratio. As the output of any given capture is a time-averaged measurement of incident photons, the validity of the relative calibration function is preserved across gate widths.

Once raw spectra are captured and processed to apply the relative intensity calibration, the resulting spectra can be used to determine the rotational and vibrational temperatures of the metastable states of molecular nitrogen that produced them.

This process involves fitting simulated emission spectra to experimental captures, and is detailed in Section 2.4 below.

Time-resolved Intensity Measurements

In order to capture sufficient data and minimise the impact of noise amid significant changes in discharge conditions, the exposure time of spectral emission captures varied between 75 ms and 50 s, depending on the gas flow rate, discharge pressure and optical access used. As a result, even under the most favourable conditions, the highest frequency of oscillation the optical emission spectrometry set-up could detect is ∼6.66 Hz. Thus almost any evidence of oscillation or instability in plasma parameters will be obscured in OES measurements by the effective time-averaging such measurements apply. Pascale observed instabilities and oscillations with frequencies on the order of 100 Hz in argon plasma in a device of the same dimensions as used in this work [88], suggesting a technique with higher time-resolution will be required to fully characterise plasma behaviour.

This higher time resolution is achieved using a ThorLabs DET10A/M Si detector, a photo-diode that outputs a voltage roughly proportional to the intensity of incident light with wavelengths between 200 and 1100 nm. The diode exhibits a rise-time of ∼1 ns, meaning its limit of detectable oscillation frequency is determined by the sampling rate of the oscilloscope used to read its voltage output, which in this work is up to 10 GHz. The photo-diode was used to take time-resolved intensity measurements of the optical output from the source region, the output of which was run through a fast Fourier transform (FFT) on the oscilloscope to determine whether oscillations were present across a range of discharge conditions and, if so, the dominant frequency and amplitude of those oscillations. As such measurements required optical access to the source, the corresponding optic fibre was redirected from the spectrometer to the photo-diode for these experimental runs. Due to this, simultaneous time-resolved intensity and optical emission spectrometry measurements were not performed.

Time-varying oscillations in the intensity of emissions from the plasma were observed across a wide range of discharge conditions. These results are presented in Section 4.3.

2.4 Temperature Determination from Experimental Spectra

This section details the considerations and processes necessary to extract rotational and vibrational temperature values from nitrogen spectra captured using OES. First, the criteria involved in the selection of wavelength ranges to investigate are introduced, and the nitrogen emission spectrum is examined to find suitable ranges that allow temperatures of the N_2(C) and N_2^+ (B) states to be resolved from the overlapping Second Positive and First Negative emission systems. Next, the two programs used in this work to simulate nitrogen emission spectra and fit them to experimental data are introduced. Fittings to the First Positive and Second Negative systems are produced using both programs to assess and compare their fitting quality.

2.4.1 Examined Wavelength Ranges

Significant overlap exists between emissions of the First Negative system, produced by molecular nitrogen ions in the second excited state, N_2^+ (B), and the Second Positive system, produced by neutral molecules in the third excited state, N_2(C). Therefore, when both species are present in a discharge, careful selection of suitable wavelength ranges over which spectra are captured is vital to being able to produce accurate fittings and thus extract meaningful temperature values from OES measurements.

The experimental spectrum shown in Figure 2.7 spans the wavelength range where the strongest emissions for both relevant emission systems occur. It was captured using Lightfield's 'step-and-glue' method, which stitches spectra captured across several smaller wavelength regions together to form a single spectrum over a wide range of wavelengths. Fittings were attempted to spectra captured with this method, however the dispersion defects caused by stitching spectra together, coupled with high-intensity peaks necessitating short exposure times that limit the resolution of lower-intensity peaks, lead to poor fits. It was therefore determined that each fitted spectrum should correspond to one $\sim$13 nm wide capture, and would ideally contain peaks of similar heights to maximise the signal to noise ratio. Additionally, the examined ranges must contain at least three vibrational band structures. Two vibrational levels are needed to determine a vibrational temperature, which can then be confirmed by a third. Thus, while not used for temperature determinations, the step-and-glue spectrum is nonetheless helpful in examining the relevant wavelength range to determine which 13 nm wide regions best fulfil these criteria.

From Figure 2.7 it is evident that the entire relevant wavelength region has contri-

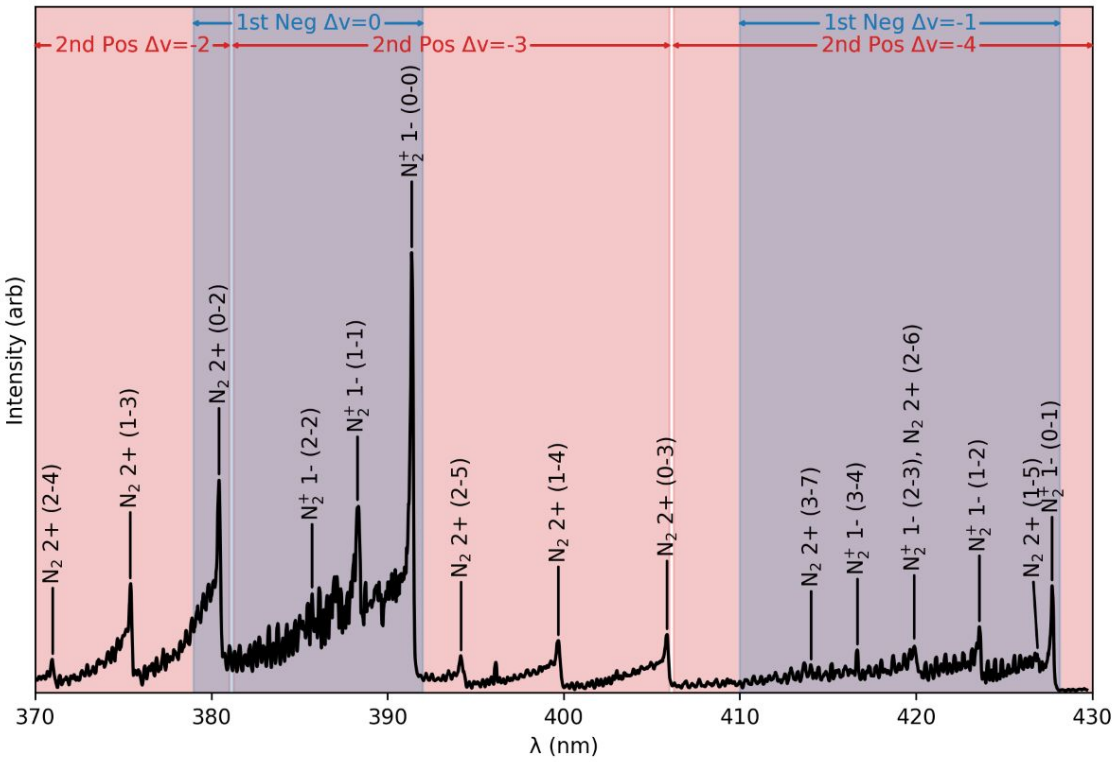

Figure 2.7: Example step-and-glue spectrum with major peaks and vibrational band structures of the First Negative and Second Positive systems labelled. Experimental data captured along the device axis of a 950 W, 5 slpm discharge at a pressure of 200 T. Emission system peaks and contribution regions labelled according to Ref.[8].

butions from the Second Positive system. The contribution of the neutral spectrum will therefore need to be accounted for and subtracted from any captured spectra to allow measurement of the temperatures of N_2^+ (B). This process requires N_2(C) temperatures to be known accurately. This indicates that N_2(C) temperatures should be determined using a wavelength range corresponding only to emissions from the Second Positive system in order to avoid needing to remove ionic spectral contributions. Additionally, a portion of the wavelength range selected for capturing the First Negative system needs to correspond only to Second Positive system contributions, so that the intensity of the simulated neutral spectra can be accurately scaled relative to that of the experimental spectra before subtraction.

Considering these requirements and referring to Figure 2.7, an obvious range centred on ∼400 nm emerges. Three vibrational peaks and two rotational bands of the Second Positive system can be captured between ∼ 393 and 405.5 nm without contribution from the First Negative system. The heads of the vibrational band structures are of roughly similar height, allowing the entire range to be captured with

a low signal-to-noise ratio. Fittings of spectra captured in this region would provide temperatures of $N_2(C)$, which can then be used to simulate and subtract the Second Positive system contributions from captures of the First Negative system.

Regarding the First Negative system, the high peak at ∼391 nm rules out imaging the Δv=0 system, as it will limit the resolution with which the other vibrational peaks will be measured. Therefore, wavelengths between ∼418.5 and 431 nm were selected as the second range to be studied. This region captures most of the Δv=-1 vibrational system, including three vibrational peaks, as well as a small region above ∼429 nm in which contributions come only from the second positive system. The Second Positive system peaks present in the overlapping region are produced by transitions originating in the same vibrational levels of $N_2(C)$ as those measured in the pure-neutral spectrum, ensuring accuracy of the subtracted simulated spectrum. Finally, the relative intensity of the (0-1) peak is low compared to the other vibrational peaks in the region and their rotational band, allowing measurements with high counts across the entirety of the measured structure. This includes the unobscured Second Positive system contributions, allowing for the simulated neutral spectra to be accurately scaled and subtracted.

2.4.2 Fitting Software

Two programs were used for spectral fitting in this work, Specair and MassiveOES.

Specair

Specair is a proprietary software for modelling several spectra produced by a variety of atomic and molecular species relevant to atmospheric pressure plasma, including the First Negative and Second Positive systems of N_2. The model is based on the Non-EQuilibrium Air Radiation (NEQAIR) code, a NASA-developed radiative heating code for predictions of atmospheric conditions in flight [89]. It is widely used as a standard in the field of high-pressure plasma [78–81].

Unlike most spectral simulation programs, Specair does not utilise pre-calculated databases of state-energies based on approximate polynomial expansions to produce spectra. Instead, state energies are calculated within the spectral modelling process by Hamiltonian inversion. This process allows the model to account for perturbations in peak intensities arising from the plasma being out of thermal equilibrium [89]. These perturbations occur in several emission systems, including the First Negative and Second Positive systems[90], meaning Specair may produce more ac-

curate values for peak wavelength and intensity in its simulated spectra, allowing more accurate fitting of non-equilibrium plasma than other models.

Spectral fitting is performed in Specair by using Brendt's method to minimise the root mean square of residuals produced by the subtraction of a simulated spectrum from the fitted data. Spectra simulated by Specair follow Boltzmann distributions of four temperatures: excitation, vibrational, rotational and translational. A single temperature is varied at a time, for which minimisation is performed. Cycling between temperatures to minimise allows the residual space to be explored and a minimum located. While the minimisation process is performed by the program, the cycling of parameters is performed manually.

MassiveOES

MassiveOES is an open-source Python program for spectral fitting of several molecular species relevant to laboratory plasma discharges, particularly those in air [77]. The program uses databases of transition lines, their Einstein A (spontaneous emission) coefficients, and upper state energies to calculate relative peak heights generated by a population represented by separate rotational and vibrational single-temperature Boltzmann distributions. Line broadening is included in the model as two free parameters, permitted to vary to overcome the model not explicitly defining pressure. The use of tabulated spectroscopic data and indirect accounting for pressure means that the model does not account for line position and intensity perturbations that are considered by Specair.

Unlike Specair, however, MassiveOES includes dispersion correction as part of its modelling, as well as batch processing of spectra. These factors combine to allow large sets of individual spectra to be fit both more quickly and potentially more accurately using MassiveOES than they could be in Specair. This is especially the case for higher pressure discharges, in which plasma is closer to thermal equilibrium, meaning perturbations accounted for by Specair are less common.

Comparison

As Specair is the model largely considered the standard for fittings of nitrogen plasma, a comparison was performed between it and MassiveOES to assess if the quality of fits and temperature data was similar between the two. These comparisons were performed for both emissions systems examined. The same experimental data was used in both programs.

Figure 2.8 shows an example of the fittings produced by the two programs for a

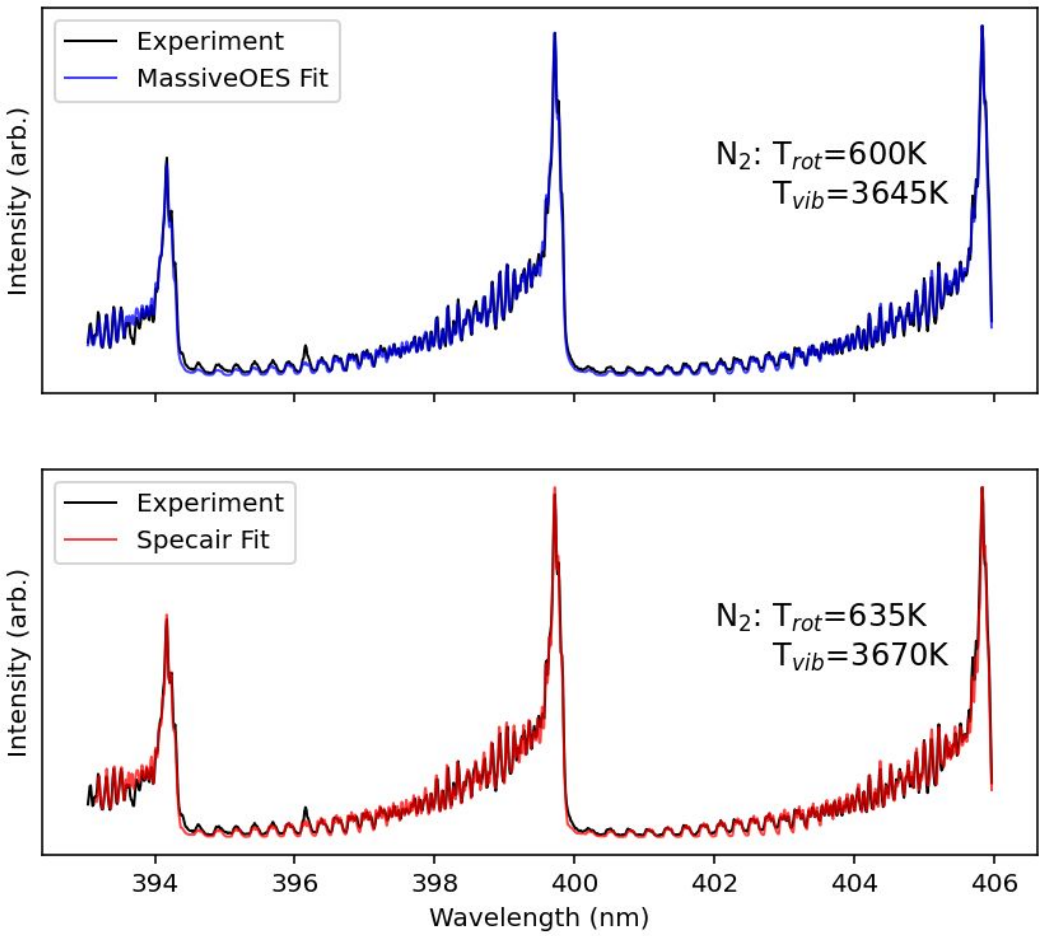

Figure 2.8: Comparison of neutral spectral fitting produced using MassiveOES (top) and Specair (bottom). Experimental spectrum captured downstream of a 950 W, 7.5 slpm discharge at 13 Torr.

spectrum captured in the plume of a low-temperature, low-pressure discharge. The rotational temperature determined by MassiveOES is within 6% of that produced by Specair. The vibrational temperatures are far closer, within less than 0.1% of each other. The agreement in vibrational temperature is unsurprising, as only three data points directly pertaining to it- the relative heights of the three vibrational peaks- are included in the data. Over the much wider variable space of the rotational bands, however, the agreement between the two programs is promising. MassiveOES performs adequately, with only the lower-wavelength sections of the two rotational bands seeing noticeably worse fittings compared to Specair. Both models accurately fit the complicated rotational structures near the vibrational band heads for the 399.8 and 406 nm peaks, and both struggle to fit an apparently unexpected trough in the rotational band below the 394 nm peak. Finally, neither model is thrown-out by the interference from an atomic peak visible near 396 nm.

In the case of the Second Positive system, MassiveOES performs well against the standard set by Specair, producing values for temperature within a reasonable estimate for error of those produced by Specair. Fittings produced by the two programs vary only marginally, especially at higher pressures, where peak broadening obscures some finer structures of the captured rotational spectrum. Thus, given its agreement with Specair, MassiveOES was used for temperature determination of captures of the Second Positive system, to allow for use of its batch processing and automatic dispersion correction.

The uncertainty of temperatures fitted using MassiveOES were estimated by trimming small segments off of the ends of spectra, between approximately 0.25 and 0.5 nm, and re-running the fitting procedure. This trimming and re-fitting was performed twice per captured spectrum, thus three values were determined for both rotational and vibrational temperatures for each captured spectrum. The final temperatures reported for these spectra correspond to the mean of these three values. The uncertainty of these final temperatures are estimated to be equal to the standard deviation of the three values, given the low number of samples.

Regarding the First Negative system, however, MassiveOES produced fitted temperatures much less in-line with those of Specair. Figure 2.9 shows an example of this, where MassiveOES fits a capture of the Δv=0 structure of the First Negative system to a rotational temperature 800 K higher than Specair. This wavelength range was selected for this comparison instead of the range primarily used for First Negative system temperature determination in this work in order to maximise the number of available rotational peaks for the fitting, to best elucidate the capabilities of the models.

It can be seen that MassiveOES is less capable of matching the experimental peak shapes in the 382-386 nm range compared with Specair. Between 382 and 388 nm, the MassiveOES fit fails to reflect the relative height of the alternating even-odd rotational levels, underestimating the heights of the lower peaks while generally fitting the higher peaks. Specair's fit is reliably able to match this ratio. The few peaks in this range underestimated by Specair align with similar underestimates in the MassiveOES spectrum, which may indicate inaccuracies in the subtraction of neutral contributions rather than fitting. Finally, MassiveOES cannot account for an apparently missing rotational peak near 390 nm, while Specair simulates its absence relatively accurately. This last example may be a reflection of Specair's ability to calculate perturbations in the First Negative system that cannot be accounted for by pre-calculated database values. Such perturbations may also account for the rotational peak height and shape matching issues experienced by MassiveOES, or

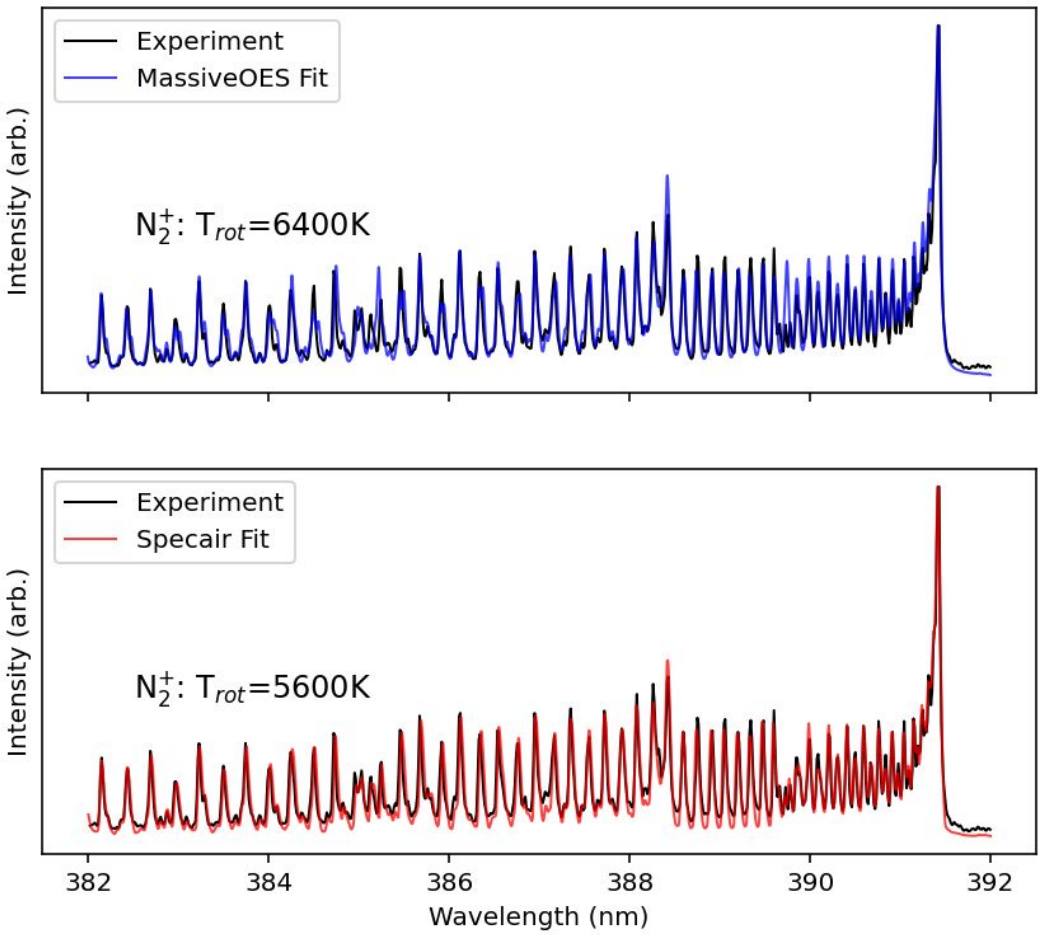

Figure 2.9: Comparison of ion spectral fitting produced using MassiveOES (top) and Specair (bottom). Experimental spectrum captured in the source of a 950 W, 5 slpm discharge at 204 Torr.

may simply indicate that the spectroscopic data used in the Specair model is more accurate for this region compared to those used by MassiveOES. Due to its comparatively stronger performance, Specair was used for modelling of the First Negative system to ensure the N_2^+ (B) rotational temperatures determined in this work are accurate and not affected by unaddressed perturbation of rotational lines.

Chapter 3

Thermal Characterisation

In this chapter, results of temperature fittings of experimental spectra performed using MassiveOES and Specair are presented. First, the conditions for which rotational temperatures of the $N_2(C)$ state are in equilibrium with the neutral gas temperatures are determined for both the source region and plume. This is performed using calculations of the neutral gas density and collision frequency. Following this, the vibrational population distributions of the $N_2(C)$ state are presented and discussed, before vibrational temperatures are reported. Trends in these temperatures are assessed with respect to the gas temperature results. Possible evidence of vibrational-translational relaxation is identified. Next, rotational and vibrational temperatures of the $N_2^+(B)$state determined from fittings to the First Negative emission system are reported. These results are compared to the neutral gas and $N_2(C)$ vibrational temperature. Finally, an assessment of the thermal characteristics of the examined discharge is performed, in which the flow of enthalpy between rotational and vibrational excitation modes is evaluated. Measurements indicating vibrational-translational relaxation rates vary across discharges of differing flow rates are used to determine the likely mechanism producing trends in the gas temperatures. The results of this chapter are then synthesised into an estimate for overall thermal efficiency of the torch, the assumptions of which are assessed with respect to flow velocity results and the temperatures sustained by the water cooling system.

3.1 Neutral Gas Density and Collision Frequency

The gas temperature of nitrogen discharges are often determined in the literature by measurement of the $N_2(C)$ state rotational temperature using fittings to the Second Positive system [73]. This is due to the high rotational-translational energy coupling in molecular nitrogen, which results in rotational and translational temperatures equilibrating after only a small number of collisions. Therefore, before measured

N_2(C) rotational temperatures can be taken as equal to overall gas temperatures, it is necessary to determine whether molecules in the excited state experience a sufficient number of collisions on average before emitting the measured light. Otherwise the measured rotational temperature will overestimate the actual gas temperature, as the process of exciting a molecule up to the C state is likely to also produce some ro-vibrational excitation.

The neutral gas collision frequency was calculated for all discharge conditions studied in order to determine which exhibit sufficiently high collision rates for equilibration between the measured rotational temperature and the gas temperature to occur. To do this, the rotational temperatures were first assumed to be accurate measurements of gas temperature and used to calculate the neutral gas density of the discharge according to the ideal gas law:

$$n_g = \frac{P}{k_b T} \tag{3.1}$$

where n_g is neutral gas density (m^{-3}), P is measured pressure (Pa), k_b is Boltzmann's constant and T is the gas temperature (K). While not an ideal gas itself, nitrogen behaves sufficiently similarly to one at the temperature and pressure ranges examined in this work for the ideal gas law to accurately model its behaviour [91].

Next, the gas density and assumed temperature were used to calculate the average collision frequency experienced by a molecule in the discharge according to [92]:

$$Z = \sqrt{2}\pi d_{N_2}^2 n_g \sqrt{\frac{8k_B T}{\pi m_{N_2}}} \tag{3.2}$$

where d_{N_2} is the kinetic diameter of molecular nitrogen, equal to 0.364 nm [93], and m_{N_2} is the mass of a nitrogen molecule, equal to $4.6518\times\ 10^{-26}$ kg.

In the following section, the calculated neutral gas densities and collision frequencies are reported for all discharges examined. Density results are evaluated in light of differences between the pressure measured in the source region and the plume, yielding insight into gas flow behaviour in the source. Collision rate results are evaluated against the N_2(C) state radiative lifetime and equilibration rate to determine in which discharge conditions the measured N_2(C) rotational temperatures can be taken as equal to the overall gas temperature.

3.1.1 Neutral Gas Density

By adjusting the two ball valves between the device chamber and the vacuum pump, operating pressure in the device can be independently varied. Figure 3.1 shows

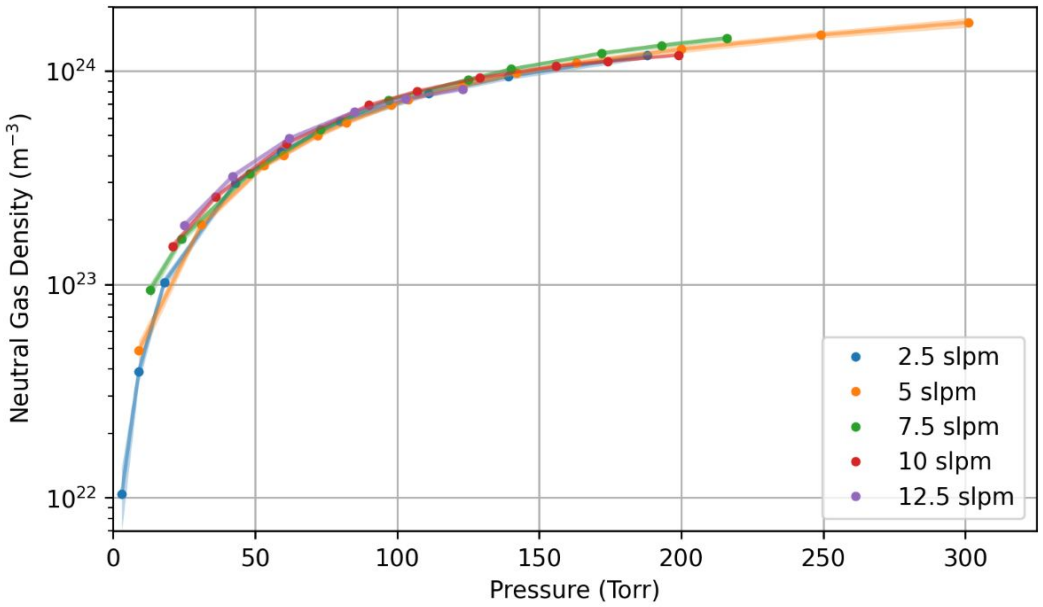

Figure 3.1: Neutral gas density calculated for the source region against pressure for all examined discharge conditions.

the source region neutral gas density against pressure for the five examined flow rates, calculated using pressure measurements and spectrally determined $N_2(C)$ state rotational temperatures collected for plasma in the device source.

The variation in temperature between flow rates can be seen to produce small differences in density at low pressures. The relative size of such differences decreases with increasing pressure. Comparing results among each data set suggests neutral gas density exhibits a relatively weak correlation with temperature and a strong correlation with operating pressure. This gives rise to relatively consistent densities with respect to pressure across the examined flow rates.

Gas Density in the Source Region Throat

Pressure measurements of the source and downstream regions (detailed later in this section) agreed within uncertainties for most conditions. Statistically significant pressure differences were observed only for the lowest examined pressures of the 10 and 12.5 slpm discharges. The ratio of downstream to upstream pressure is related to the Mach number of an isentropic flow by:

$$M = \sqrt{\frac{2}{\gamma - 1}\left(1 - \left(\frac{P_d}{P_u}\right)^{\frac{\gamma-1}{\gamma}}\right)} \tag{3.3}$$

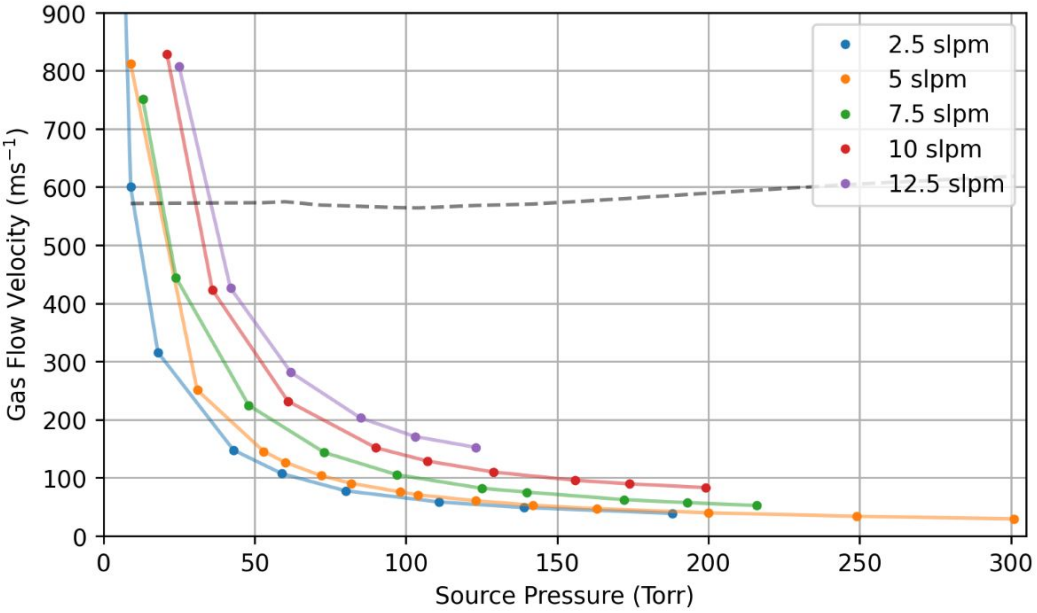

Figure 3.2: Average axial flow velocity against pressure for all flow rates, calculated assuming an incompressible flow using calculated values of average source density. The dashed grey line corresponds to the local speed of sound, calculated using average temperatures calculated from 5 slpm flows. Other flow rates yield similar speeds of sound.

where M is the Mach number, γ the ratio of specific heats ($\approx$1.4 in nitrogen [94]) and P_d and P_u the downstream and upstream pressure, respectively. The insufficient resolution of pressure measurements prevents using this equation to determine gas flow velocity directly, however it can be used to show the flow is incompressible, allowing simplifying assumptions to be made. Gas flows with Mach numbers below 0.3 can be treated as incompressible, which, using Equation 3.3, corresponds to pressure ratios of approximately 0.95 and above. This describes all but two data points.

By assuming an incompressible flow, a continuity equation can be applied across the device throat, which yields the average axial velocity of gas in the source. This gives:

$$v = \frac{\dot{N}}{n_g A_t} = \frac{\dot{m}}{M_{N_2} n_g A_t} \tag{3.4}$$

where $\dot{N}$ is the particle flow rate entering the source, given by the mass flow rate $\dot{m}$ divided by the mass of a nitrogen molecule M_{N_2}, n_g is neutral gas particle density and A_t is the area of the throat. The results of solving Equation 3.4 using the calculated average density in the source is presented in Figure 3.2.

The calculated velocities significantly exceed the assumed Mach 0.3 at low pressures for all flow rates. In fact the lowest pressure data point of all flow rates correspond

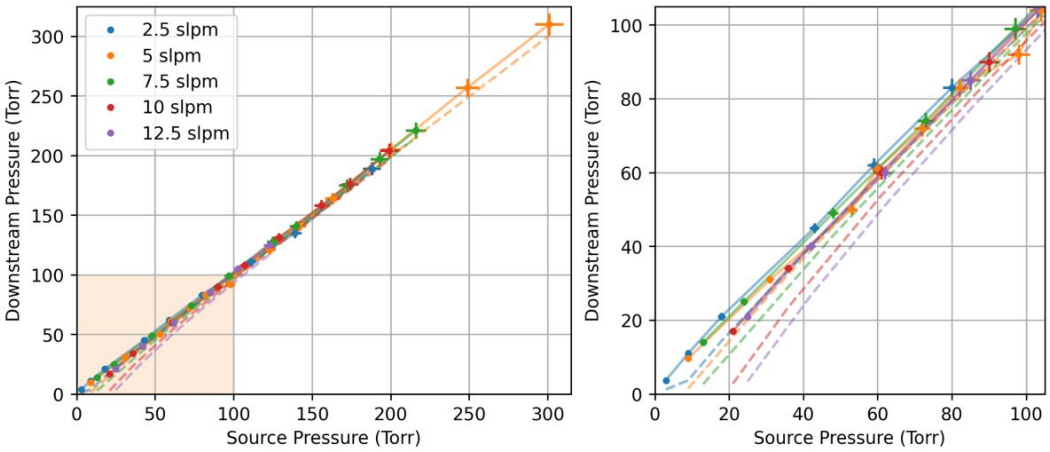

Figure 3.3: Downstream pressures against upstream pressures, measured for all discharges and flow rates. Left: full pressure range examined, Right: detailed view of lower pressures, corresponding to the highlighted region of the full range plot. Dashed lines indicate the downstream pressure required for the pressure ratio to produce the velocities shown in Figure 3.2.

to velocities well in excess of the local speed of sound. By Equation 3.4 it can be determined that such velocities would necessitate pressure ratios below 0.5, corresponding to pressure differences well outside of the uncertainty of even the smallest pressure measurements. These measurements are presented in Figure 3.3, alongside the pressures required to sustain the velocities depicted in Figure 3.2.

The pressure measurements show poor agreement with those predicted using the calculated velocities at low pressures, which correspond to the highest predicted velocities. This divergence indicates that the density used in the velocity calculation is lower than the actual average density of gas passing through the throat. Such discrepancy likely results from a significant share of cold, freshly injected gas passing immediately through the throat, instead of spiralling up the walls as part of the reverse vortex.

This behaviour varying with flow rate could also account for the similarity in downstream pressure measurements between high and low flow rates at higher upstream pressures. For these pressures the continuity equation indicates that high flow rates should see meaningfully higher velocities and thus lower downstream pressures compared to low flow rates. If high flow rates see a greater share of injected gas immediately lost downstream, the average gas density through the throat would increase with flow rate for a given pressure. Higher densities allow a given velocity and thus pressure ratio to sustain a greater mass flow rate, thereby allowing higher flow rates to exhibit pressure ratios similar to low rates.

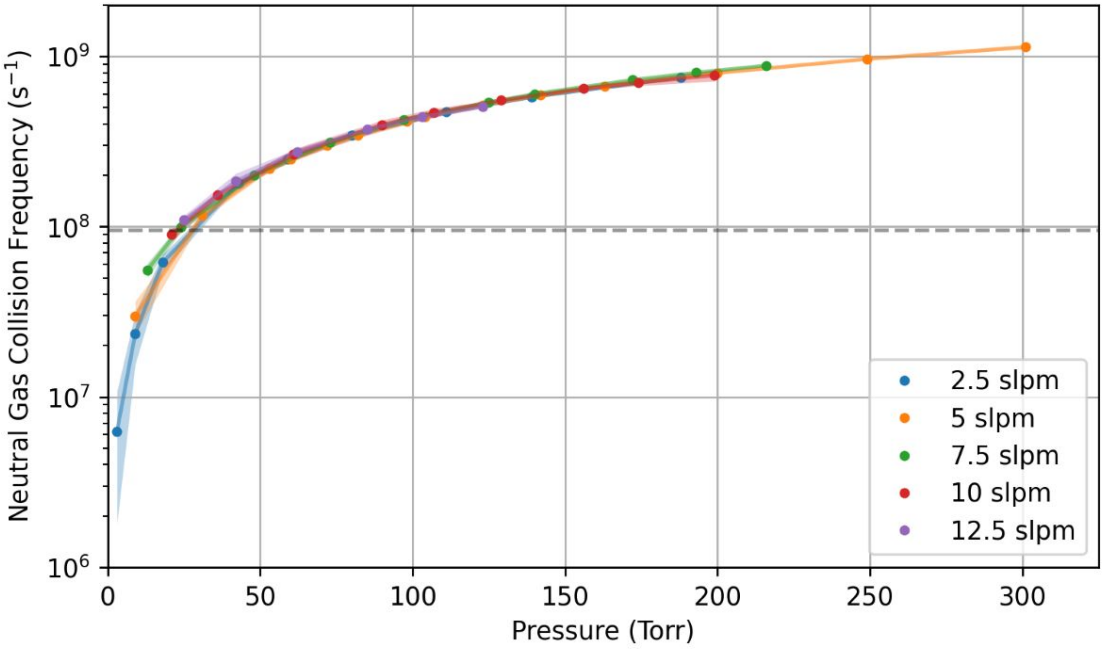

Figure 3.4: Neutral gas collision frequency against pressure, calculated using pressures and $N_2(C)$ rotational temperatures captured in the source region. The dashed grey line marks the rate corresponding to a collision interval one-quarter of the radiative lifetime of the $N_2(C)$ state. The rotational temperature determined using the Second Positive system cannot be assumed to be in equilibrium with gas temperatures for discharges exhibiting collision frequencies below this value.

3.1.2 Neutral Gas Collision Frequency

Collision rate is strongly dependent on gas density, meaning it too is dominated by discharge pressure. Figure 3.4 plots the source region collision rate against pressure for all examined discharge conditions. For pressures above 50 Torr, all flow rates see very similar collision frequencies, with differences between them being largely within the ranges of uncertainty. Therefore, for most of the examined pressure range, the collisionality of a discharge can be accurately approximated as independent of flow rate and solely a function of operating pressure.

The $N_2(C)$ state has a radiative lifetime of is 41 ns [95], and requires approximately 4 collisions to equilibrate with the ground state [96]. The minimum collision frequency for which the average $N_2(C)$ molecule equilibrates prior to undergoing radiative decay therefore has a collision interval of $41/4 = 10.25$ ns. This corresponds to a collision frequency of $\sim 9.76 \times 10^7$ s^{-1}, indicated by the dashed grey line in Figures 3.4 and 3.5. Density and collision frequency were calculated using possibly overestimated temperatures equal to the $N_2(C)$ rotational temperature, therefore we can confidently conclude that the gas temperature of any discharge with a colli-

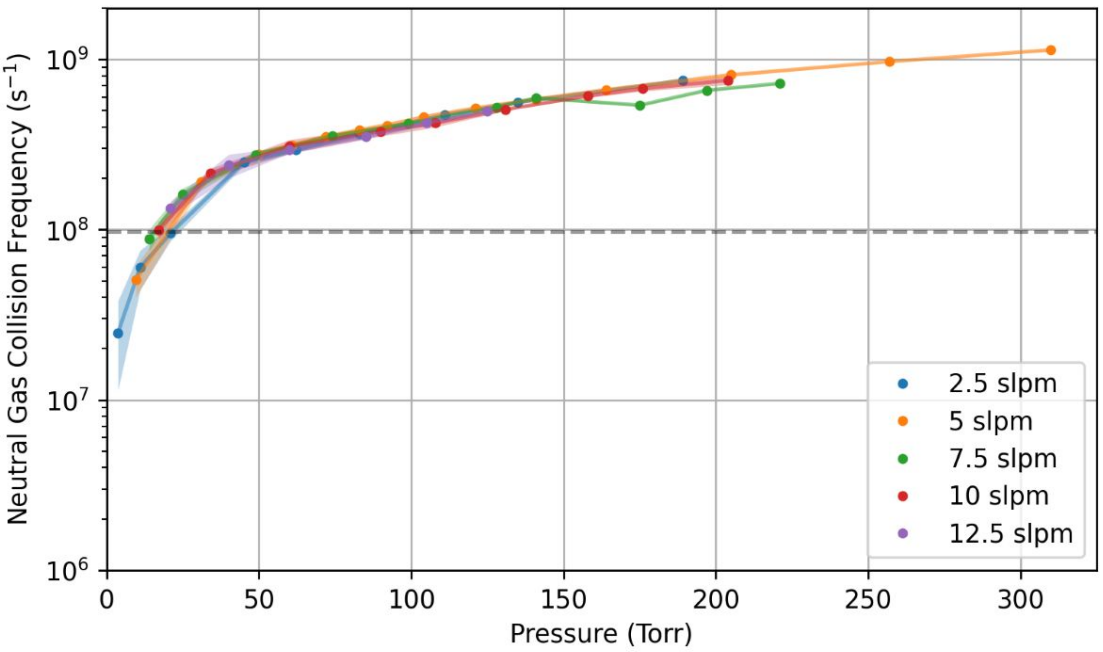

Figure 3.5: Neutral gas collision frequency against pressure, calculated using pressures and $N_2(C)$ rotational temperatures captured in the plume. The dashed grey line marks the rate corresponding to a collision interval one-quarter of the radiative lifetime of the $N_2(C)$ state. The rotational temperature determined using the Second Positive system cannot be assumed to be in equilibrium with gas temperatures for discharges exhibiting collision frequencies below this value.

sion frequency calculated to be lower than this value is not in equilibrium with the measured rotational temperature. These discharges are thus excluded from analyses of gas temperature.

Examining Figure 3.4, all source region plasmas below ∼22 Torr can be see to have collision rates below the cut-off frequency required for equilibration of the $N_2(C)$ state. This includes the three lowest pressures examined for the 2.5 slpm flow rate, as well as the lowest examined pressures for the 5, 7.5 and 10 slpm flow rates. Temperatures determined from spectra captured at these conditions are therefore skewed by the excitation processes producing $N_2(C)$ molecules, and do not reflect the actual gas temperature of the discharge. They are therefore not included in the gas temperature results presented in the following section.

Figure 3.5 reports the collision frequency in the plume calculated for all examined discharge conditions. Discharges with pressures ≤17 Torr, as well as the 2.5 slpm discharge at 21 Torr, all exhibit collision rates below the cut-off value. As was the case in the source region, this includes the three lowest pressures examined for the 2.5 slpm flow rate, and the lowest examined pressures of the 5, 7.5 and 10 slpm

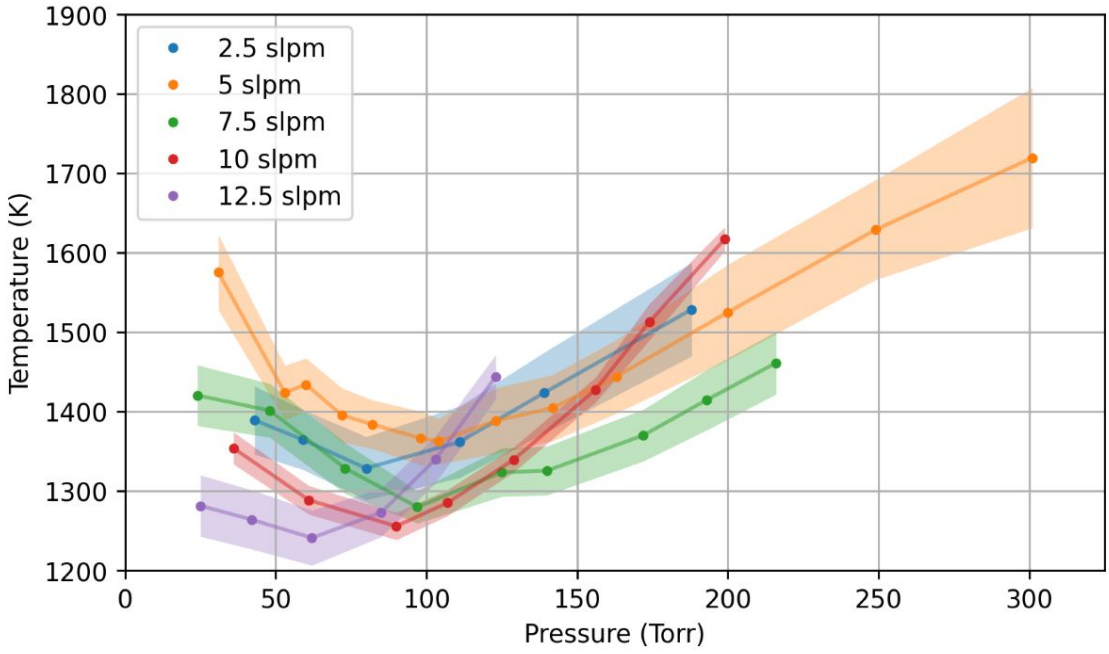

Figure 3.6: Gas temperatures measured in the source region against pressure, for all examined discharges where equilibration between $N_2(C)$ rotational temperatures and gas temperature occurs.

flow rates. These conditions see insufficient equilibration and are therefore excluded from the following gas temperature analysis.

3.2 Neutral Gas Temperatures

In the previous section, the examined conditions in which the rotational temperature of the $N_2(C)$ state is equilibrated with the neutral gas temperature were identified. This section presents the $N_2(C)$ rotational temperatures measured for those conditions, and uses them to evaluate variations in neutral gas temperature with respect to feed gas flow rate and discharge pressure.

3.2.1 Source Region Gas Temperatures

Figure 3.6 presents neutral gas temperatures determined from fittings of Second Positive system emissions captured in the source region. These temperatures show a relatively consistent general trend with respect to pressure across flow rates. Starting at low pressures, the temperature declines slightly with increasing pressure before reaching a minimum, after which it climbs with pressure at a rate substantially faster than its initial decline.

At pressures below ∼75 Torr, temperature generally decreases as flow rate increases. This aligns with simple energy balance considerations: as roughly the same amount of energy is dissipated in the plasma regardless of flow rate, increasing the flow rate will decrease energy density, as the same amount of energy is spread across a greater number of particles. The incompleteness of such an explanation is evident, however, as despite moving double the number of particles through the device, the 12.5 slpm case is only ∼250 K or 20% cooler than the 5 slpm case around 50 Torr. Instead gas flow behaviours, such as the likely significant share of gas not passing under the coil in high flow rate discharges identified in Section 3.1.1, play a significant role in the source temperatures achieved. This is demonstrated by the 2.5 slpm flow rate, which, at low pressures, sees temperatures lower than the 5 slpm case and, below ∼60 Torr, the 7.5 slpm case. This is likely caused by a weak or even absent reverse vortex flow in these conditions, leading to increased heat loss to the source region walls. This is examined in more detail in Section 3.5.1.

As pressure increases above 75 Torr, higher flow rates exhibit temperature minima at lower pressures than lower flow rates. Additionally, the gradient of the subsequent temperature increase with respect to pressure is higher for higher flow rates. These behaviours result in inversions of the temperature dependence at higher pressures, with both the 10 and 12.5 slpm cases exhibiting the highest temperatures of any flow rate at the pressures immediately prior to their extinction. This does not extend to the 7.5 slpm case, however, as its temperature does not eclipse that of the 5 slpm case before extinction, despite exhibiting a comparatively higher gradient.

As established by Figure 3.1, discharges of all flow rates exhibit similar neutral gas densities in the source region at any given pressure above 50 Torr. Thus, for the increased heating observed in higher flow rates to originate from an increase in collisions and thus energy transfer between neutral particles and electrons, higher flow rates would need to exhibit higher electron densities than lower flow rates. Under this assumption the lower temperatures experienced at lower pressures would similarly require lower electron densities.

Alternative explanations for the increasing temperatures include heat losses to the walls decreasing due to stronger reverse vortex formation, and increased coupling of energy directly into the rotational mode within the source.

Regarding the former explanation, the insulation effect provided by the reverse vortex flow would be expected to scale with the speed of the gas flow against the walls. This is because faster-flowing gas experiences a stronger centripetal force pushing it against the wall, creating a stronger barrier between it and the heated gas inside the plasma core. Additionally, faster gas spends less time underneath the coil when

part of the outer upwelling vortex, minimising the heating experienced and subsequent thermal losses while closest to the wall. As indicated in Figure 3.2, velocity is expected to increase with flow rate and decrease with pressure, which does not align with the observed source region temperature trends. Given the indications that a lower share of injected gas actually joins the reverse vortex presented in Section 3.1.1, insulative benefits may only manifest at higher pressures, when a sufficient share of the flow transits the source region before flowing downstream. This possibility is further examined in Section 3.5.1.

Regarding the latter explanation, energy can be coupled into the rotational mode via several paths. The rate of electron-neutral collisions resulting in translational or rotational excitation may increase due to increases to the relevant collision cross-sections. An increase in electron temperature would result in an increased elastic scattering cross section and likely produce a higher electron density, however electron temperature is generally inversely correlated to density for a given input power and is therefore unlikely to increase with pressure. A decrease with pressure is instead more plausible and may result in energy previously coupled into electronic excitation instead making its way into rotational excitation. However, given that rotational energy levels are small compared to vibrational energy levels, a decrease in electron temperature would lead to an increase in vibrational coupling more than rotational. An increase in the neutral gas collision rate would result in more energy being coupled out of the vibrational mode and into translational energy. Collision rate was found to not vary significantly across flow rates at higher pressures, meaning to account for the gas temperature trends observed in the source, vibrational temperatures exhibited by higher flow rates would need to be far higher than those of lower flow rates. This is further examined in Section 3.3.2.

3.2.2 Plume Gas Temperatures

Figure 3.7 shows the gas temperature-pressure relationships observed in the device plume. Interestingly all flow rates exhibit similar temperatures at low pressures, between 600 and 700 K for pressures around $\sim$25 Torr. They also follow similar trends, with temperature increasing rapidly with pressure up to around 100 Torr. Beyond this pressure, temperature increases are smaller, though the 7.5 slpm case sees a significant jump. Similar to the results from the source, high flow rates saw greater temperature increases than low flow rates. At these higher pressures, the 2.5 and 5 slpm cases exhibit very similar temperatures, while the higher flow rates have diverged both from the lower flow rates and from each other. This may be indicative of a mechanism that grows with flow rate, but must overcome a threshold between

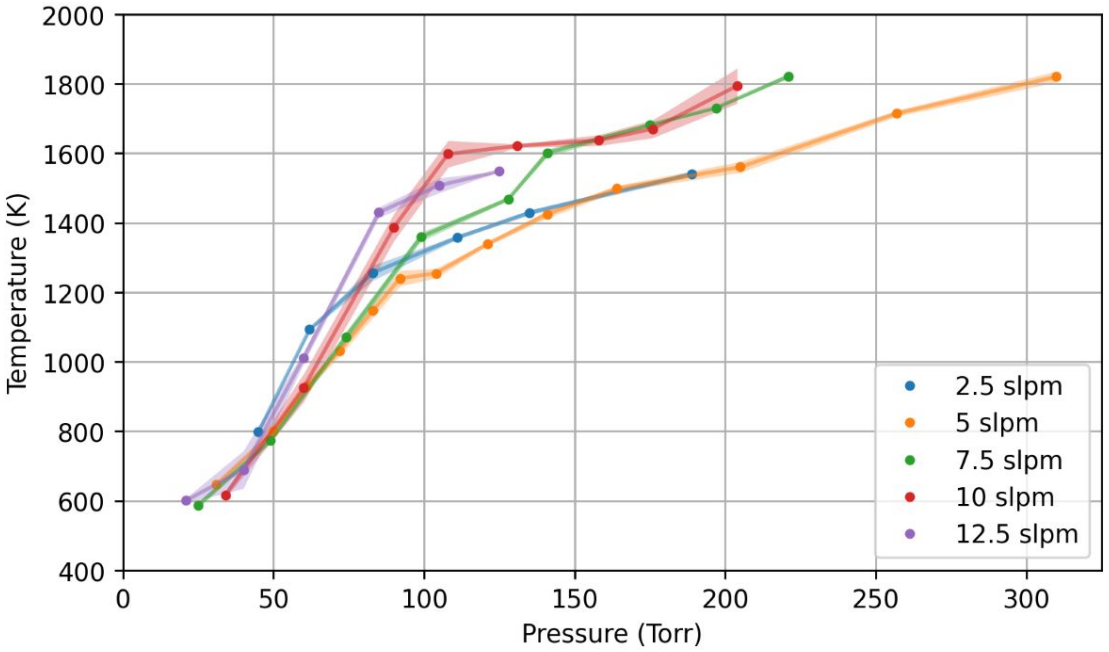

Figure 3.7: Gas temperatures measured in the plume against pressure, for all examined discharges where equilibration between $N_2(C)$ rotational temperatures and gas temperature occurs.

5 and 7.5 slpm before producing notable impacts on the plume temperature.

The low temperatures measured for all flow rates and low pressures may be attributable to adiabatic expansion of plume gas as it leaves the throat. The largest differences between upstream and downstream pressures were observed at low pressures, indicating that, in such conditions, the gas flow through the device would likely see greater expansion upon entering the injector compared to higher pressure discharges. This expansion results in the velocity of the gas increasing, with the increase in kinetic energy offset by a commensurate decrease in thermal energy.

Alternatively, these low temperatures may indicate that, at low pressures, discharges of all flow rates see most injected gas lost immediately downstream. The much higher temperatures measured in the source may correspond to only a small fraction of the total mass flow through the device, which, upon leaving the source region, mixes with cold gas in the throat to produce the low plume temperatures observed downstream. Centripetal forces pushing gas to the walls as a result of high flow velocities may contribute to this effect, as the high speeds with which gas is injected into the source at low pressures may result in hot gas under the coil being more likely to reach the walls, joining the upwelling vortex and recirculating under the coil rather than being expelled downstream. As pressure increases and gas flow speeds decrease,

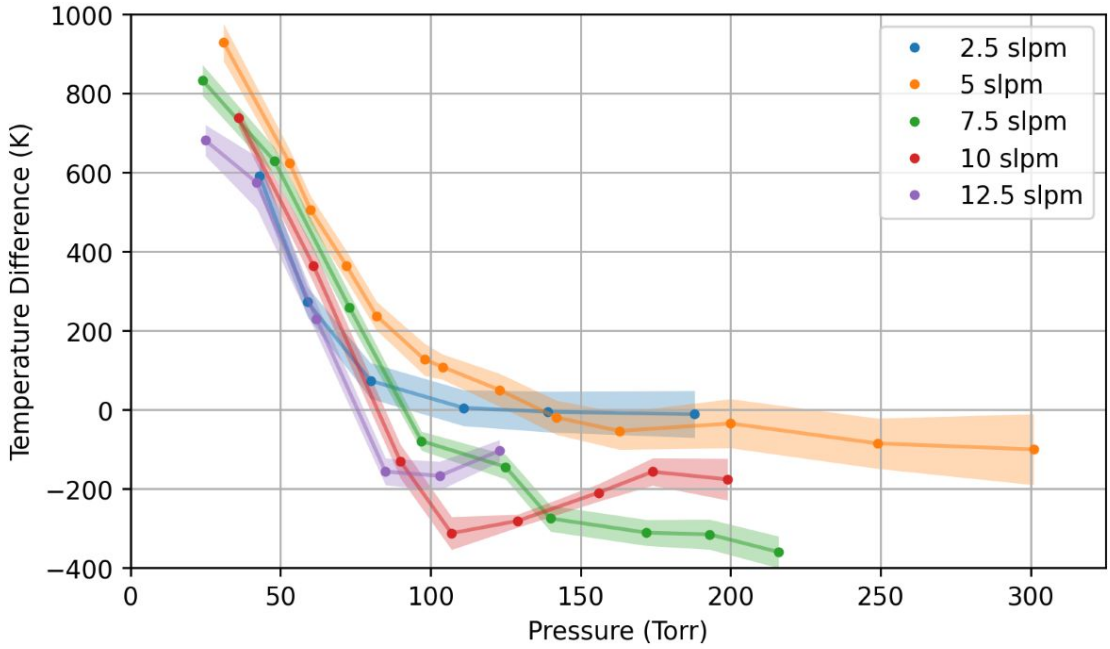

Figure 3.8: Difference between the measured gas temperatures in the source and plume, plotted against pressure for all examined discharges where equilibration between $N_2(C)$ rotational temperatures and gas temperature occurs. Positive values indicate the source is hotter, negative indicate the plume is hotter.

the share of cold, fresh gas in the upwelling vortex would then also increase, potentially accounting for the decreases in source temperatures with pressure observed at lower pressures in Figure 3.6, and the increase in plume temperatures with pressure over the same range in Figure 3.7. This possibility is discussed further in Section 3.5.1.

Figure 3.8 plots the difference between source and plume gas temperatures against pressure. At higher pressures and flow rates, the temperatures achieved in the plume exceed those reported in the source. Both the scale of this difference and the pressure at which it is first observed appears sensitive to flow rate. The 5 slpm discharge reaches equilibrium between the source and plume at a source pressure of ∼140 Torr, and by 300 Torr the difference between the two temperatures reaches approximately 100 K. The 10 slpm case sees plume temperatures exceed source temperatures between 60 and 85 Torr, and reaches a maximum difference of over 300 K by 110 Torr. Interestingly the temperature difference of the 10 slpm case decreases for further pressure increases, a behaviour mirrored by the 12.5 slpm case at lower pressures. Meanwhile, the jump up in temperature observed for the 7.5 slpm case in Figure 3.7 produces an opposite effect, causing its temperature difference to increase with increasing pressure, reaching a maximum of just under

400 K at 220 Torr. This large difference is also supported by the unusually low source temperatures observed in Figure 3.6.

Conservation of energy dictates that excess thermal energy in the plume compared to the source must correspond to energy coupled into an alternate form of excitation within the source. This implies that, in discharges with higher flow rates, an additional mechanism is present that couples energy into the translational or rotational mode as gas flows out of the source and into the injector. As outlined in Section 3.2.1, relaxation of vibrational excitation can lead to increased gas temperatures. To assess the contribution of this pathway to the observed downstream temperature increase, values for vibrational temperature are required. The following section reports the vibrational temperatures measured for the N_2(C) state. Section 3.5.2 uses these results and those reported here to assess whether vibrational-translational relaxation can account for the observed increase in temperature.

3.3 N_2(C) Vibrational Temperatures

Due to molecular nitrogen exhibiting poor energy coupling out of the vibrational mode, the spectrally-determined vibrational temperatures of the N_2(C) state cannot be equated to those of other species in the same manner as the N_2(C) rotational temperatures were equated to gas temperatures in the previous sections. Nonetheless, such results can provide valuable insight into prevailing excitation mechanisms in the plasma, which is impacted by factors such as electron temperature and density.

3.3.1 Vibrational Population Distributions

Evidence of non-Boltzmann vibrational population distributions is present in spectra emitted by plasma in the source region under all examined discharge conditions. An example is shown in Figure 3.9, which presents an experimental spectrum and three emission curves simulated assuming vibrational equilibrium.

As shown by the fittings, the relative heights of the three peaks and their rotational bands are inconsistent with a single vibrational temperature, which suggests the vibrational levels from which these peaks originate (v=2,1,0 from left to right, respectively) are not populated according to a Boltzmann distribution. This is further elucidated by Figure 3.10, which shows that relative populations of the three vibrational levels examined cannot be fit by a single linear trend-line. A Boltzmann distribution is of the form $\frac{n_k}{n} = \frac{g_k}{Z(T)} \exp\{(-\frac{E_k}{kT})\}$, where $Z(T)$ is the partition function and n_k, g_k and E_k are the number density, degeneracy and energy of an upper

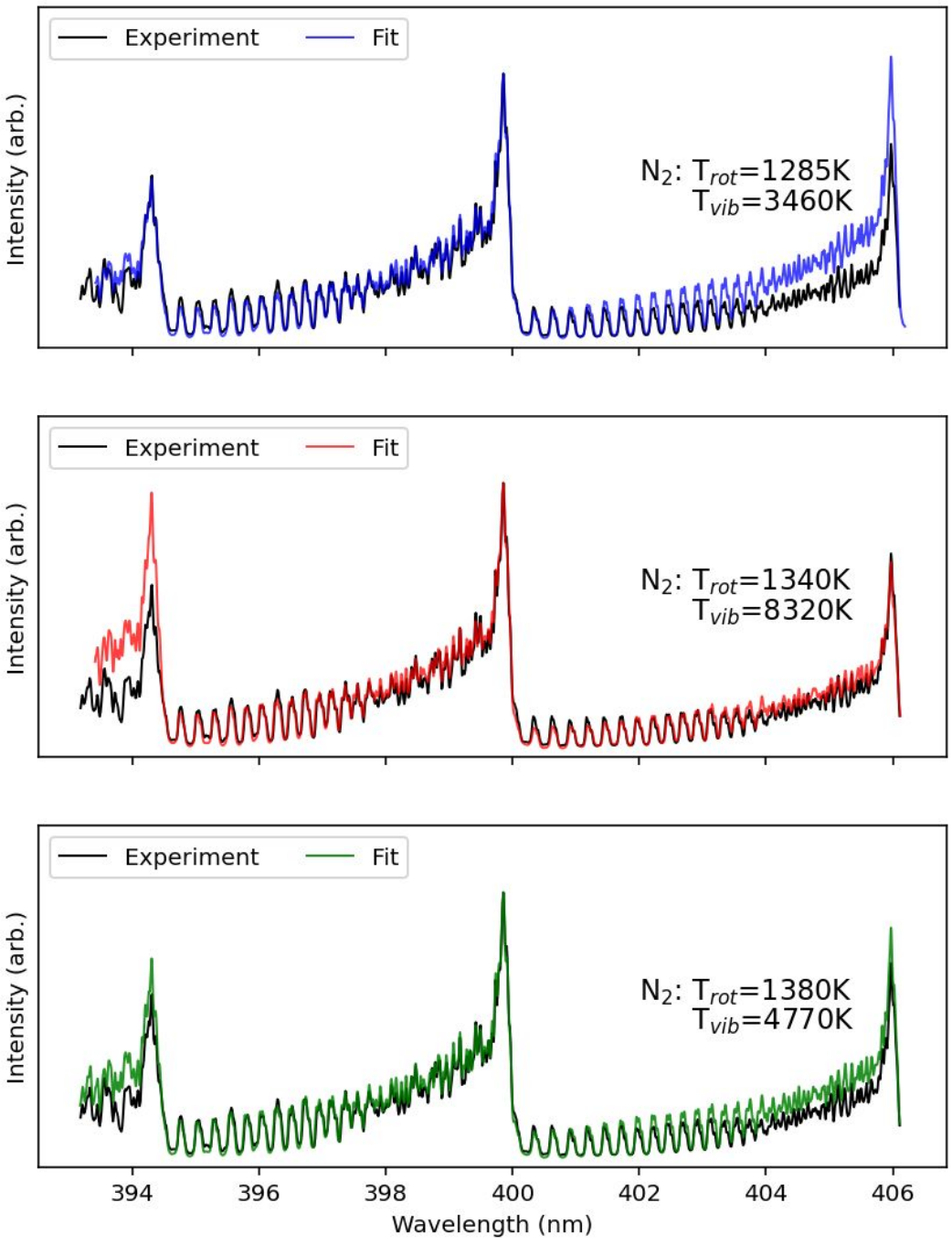

Figure 3.9: Comparison of neutral spectral fitting of the (2-5) and (1-4) peaks (top), the (1-4) and (0-3) peaks (middle) and all three peaks (bottom). All fitted spectra were produced using MassiveOES. Experimental spectrum captured in the source of a 950 W, 7.5 slpm discharge at 14 Torr.

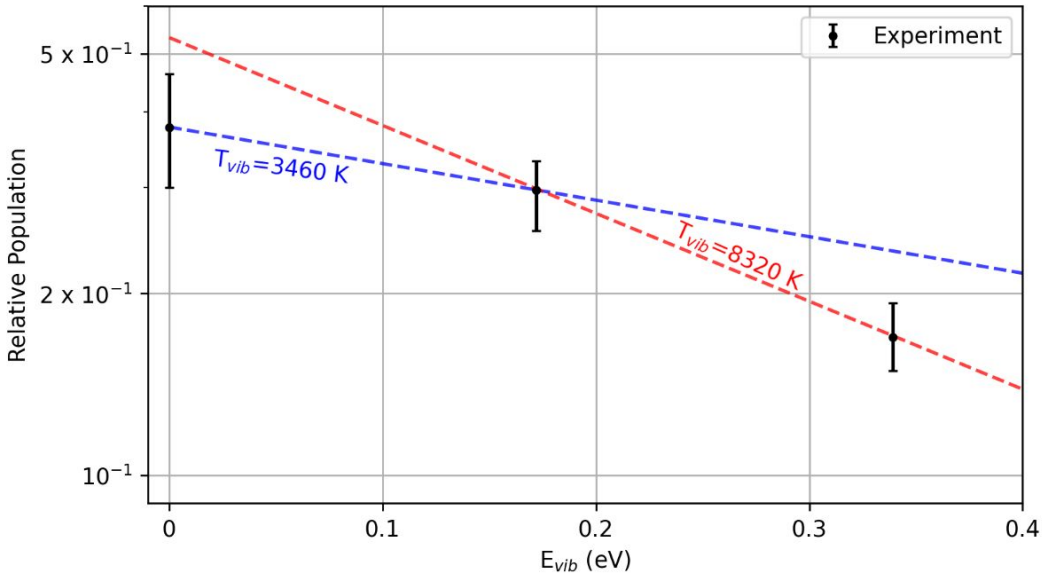

Figure 3.10: Calculated relative populations of the v=0,1,2 vibrational states plotted against vibrational energy for data captured in the source of a 950 W, 7.5 slpm discharge at 14 Torr. Dashed lines show the trend-lines expected for Boltzmann distributions with vibrational temperatures corresponding to the fittings shown in Figure 3.9. See below for details on the calculation method.

state k, respectively. As the figure plots the relative population of these states logarithmically against energy, a Boltzmann distribution would follow linear trend with a slope given by $-1/kT$. The observed population distribution instead shows significant deviation from a single trend-line. Two temperatures are therefore reported for these captured spectra, produced using fittings of the peaks corresponding to neighbouring vibrational levels: v=0,1 and v=1,2.

Due its slow vibrational relaxation time, non-equilibrium vibrational distributions are frequently observed in molecular nitrogen. Studies using Raman spectroscopy to observe the vibrational distribution of ground-state nitrogen molecules often report a Treanor distribution [97–99], which exhibits a significant overpopulation of higher-energy states compared to a Boltzmann distribution [100]. When examining only lower vibrational levels, these distributions can be approximated using two Boltzmann distributions with different temperatures; a high temperature distribution that relates the ground state to the first excited vibrational state, and a lower temperature distribution relating the first vibrational state to all higher states [101]. This approximation aligns with fittings to source region spectra in this work, suggesting the $N_2(C)$ state may exhibit a Treanor distribution.

The relative population share of these vibrational levels can be calculated using a two-temperature population model detailed in Ref. [99], in which the upper vibra-

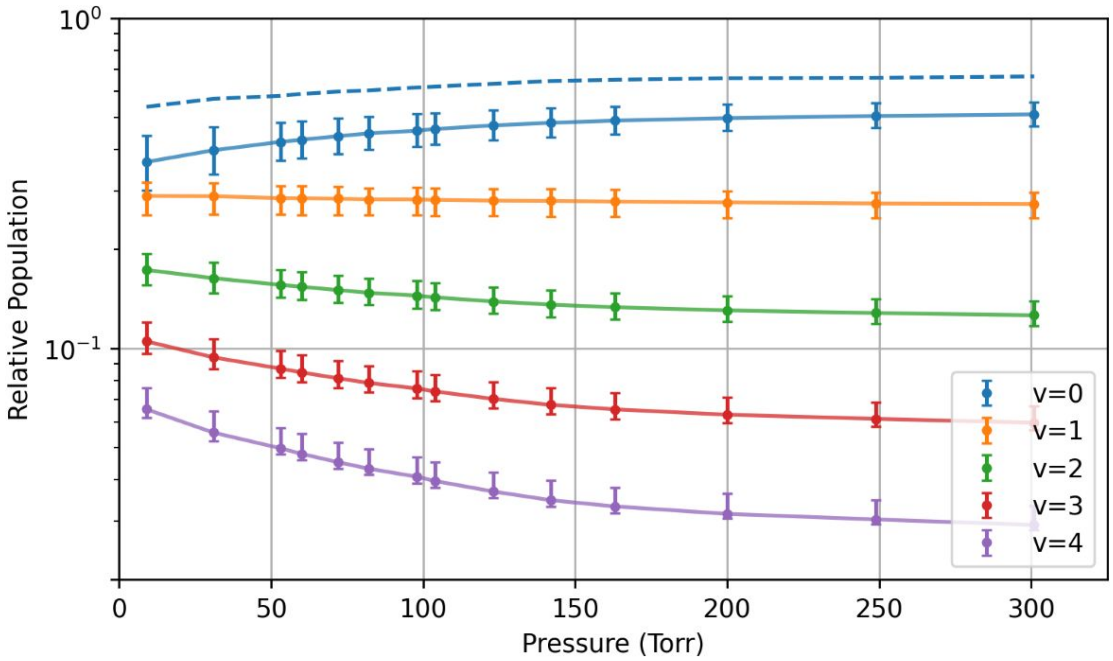

Figure 3.11: Calculated relative populations of the vibrational levels of the N_2 $C^3\Pi_u$ state against pressure in the source region of a 950 W, 5slpm discharge. The expected ground state population based on the temperature of the upper vibrational levels, scaled to match the upper state populations of the measured spectra, is indicated with a dashed line. Uncertainties propagated from the error of measured vibrational temperature.

tional energy levels are taken to be in a Boltzmann distribution. Unfortunately, the wavelength range selected for these experiments means that such a distribution cannot be confirmed, as to do so requires measurements of peaks corresponding to transitions from the v=3 and 4 levels. Given that the Treanor distribution appears regularly in molecular nitrogen due to vibrational properties that do no change for the N_2(C) state, such an assumption is not unreasonable. Thus, for each captured spectrum, two vibrational and one rotational temperature, all fitted using MassiveOES, were input into the aforementioned model, alongside values for the N_2(C) vibrational and rotational energy levels sourced from the MassiveOES spectral database. This allowed the relative population levels of the N_2(C) vibrational states to be calculated. An example of these populations are presented against discharge pressure in Figure 3.11 for a 5 slpm flow.

The deficit in the vibrational ground state is evident when comparing the observed v=0 population to the population projected by the vibrational temperature fit to the v=1,2 levels. Such underpopulation of the vibrational ground state has been observed in low-power, low-pressure discharges in pure-nitrogen in the literature. It appears that this device exhibits higher operating powers and pressures than any

Reaction	Threshold Energy
Electron Excitation of the ground state	
$N_2(X,v) + e^- \rightarrow N_2(C,v') + e^-$	$E_{threshold}$=7-11 eV
Electron Excitation of the first excited state	
$N_2(A,v) + e^- \rightarrow N_2(C,v') + e^-$	$E_{threshold}$=4-6 eV
Energy pooling of the first excited state	
$N_2(A,w) + N_2(A,w') \rightarrow N_2(C,v') + N_2(X,v)$	

Table 3.1: N_2(C) production mechanisms assessed in the kinetic model of Ref. [13]

other in which this behaviour has been reported.

In their study of the second positive system emissions of low-power(10-100 W), low-pressure (<1 Torr), radio-frequency capacitively coupled nitrogen plasma, Fatima *et al.* [76] reported vibrational temperatures of the second positive system determined using two methods: spectral fitting of four vibrational peaks assuming a Boltzmann distribution, and calculation using the intensity ratio between the v=0 and v=1 peaks. For all examined pressures and powers, the peak ratio temperature was found to be higher than the fitted Boltzmann temperature, indicating an overpopulation of the ground state, as observed in this work. The relative difference between the two temperatures appears inversely correlated to electron temperature, with higher electron temperatures yielding more similar vibrational temperatures.

A similar non-equilibrium vibrational distribution was also observed by De Benedictus and Dillece [13] in their study of a pulsed low-pressure RF capacitively-coupled discharge. Interestingly, however, such a distribution appeared only in the afterglow plasma between pulses; while the discharge was active the vibrational population followed Boltzmann distributions. This is despite the discharge operating with maximum electron temperatures of 2.5 eV, well within the energy range where electron-neutral collisions resulting in vibrational excitation of the ground state have the greatest cross-section. Compared with the discharges studied by Fatima *et al.* , which exhibited a minimum electron temperature of 6.6 eV, these discharges are more likely to exhibit a Treanor distribution in the ground state. Despite this, the development of a non-Boltzmann distribution was observed only in the afterglow, when electron temperature drops significantly.

De Benedictus and Dillece used a kinetic model of N_2(C) production to fit the observed vibrational distributions. The model considered three production processes, listed in Table 3.1. Assuming electrons in the discharge follow a Maxwellian distribution, dominance of the first process would produce a vibrational distribution similar to the ground state, while the latter two involving the N_2(A) state would

skew the vibrational distribution toward higher levels. This is due to the potential energy wells of the A and C states seeing poor alignment with respect to internuclear distance (see Figure 1.8), resulting in low Frank-Condon factors and thus low probabilities for transitions between N_2(A) state molecules and the N_2(C) ground state.

The modelling showed that while the plasma was active N_2(C) state production was dominated by direct excitation from the ground state by electron collision. This dominance weakens as pressure increases and electron temperature decreases, dropping from ∼99% of production at an operating pressure of 0.1 Torr and T_e=2.5 eV to ∼93% at 3 Torr and T_e=1 eV. The difference in production at higher pressure shifts almost entirely to collisional excitation of the first excited state. Fittings for distributions measured in the afterglow, when the electron temperature had decayed to between 0.2 and 0.3 eV, found significantly reduced contribution from direct collisional excitation from the ground state. The largest increases were found for collisional excitation of the first excited state, and all examined pressures saw contributions from energy pooling collisions between N_2(A) molecules significantly increase compared to the active discharge at the same pressure.

The importance of the N_2(A) state in producing an underpopulated N_2(C) v=0 level evident from the results of Ref. [13] can be used to account for the observation of population inversion in Ref. [76] despite the much higher electron temperatures present in that discharge. In a discharge where T_e= 2.5 eV, the vast majority of nitrogen molecules remain in the electronic ground state. As a result, electron collisions primarily occur with ground state molecules, a small share of which involve enough energy to produce N_2(C). As the electron temperature increases it approaches the excitation energy of the N_2(A) state, 6.17 eV [102], meaning an increasing large share of neutral nitrogen exists as N_2(A) state molecules. At the electron temperatures present in Ref. [76], the density of the N_2(A) state is far higher, allowing collisional excitation of the state, either by another N_2(A) molecule or an electron, to dominate the production of N_2(C) molecules and skew the vibrational distribution toward higher levels. As electron temperature increases further, the equilibration between vibrational levels improves as a larger share of electrons colliding with ground state molecules have enough energy to directly populate the v=0 level of N_2(C). Finally, at the low electron temperatures of the afterglow of Ref. [13], the long radiative lifetime of the N_2(A) state (∼1.27 s [102]) allows its density to remain high even after input power is cut, while its higher starting energy compared to ground state molecules means N_2(A) molecules require fewer electron collisions to undergo vibrational energy pooling, and thus dominate N_2(C) production.

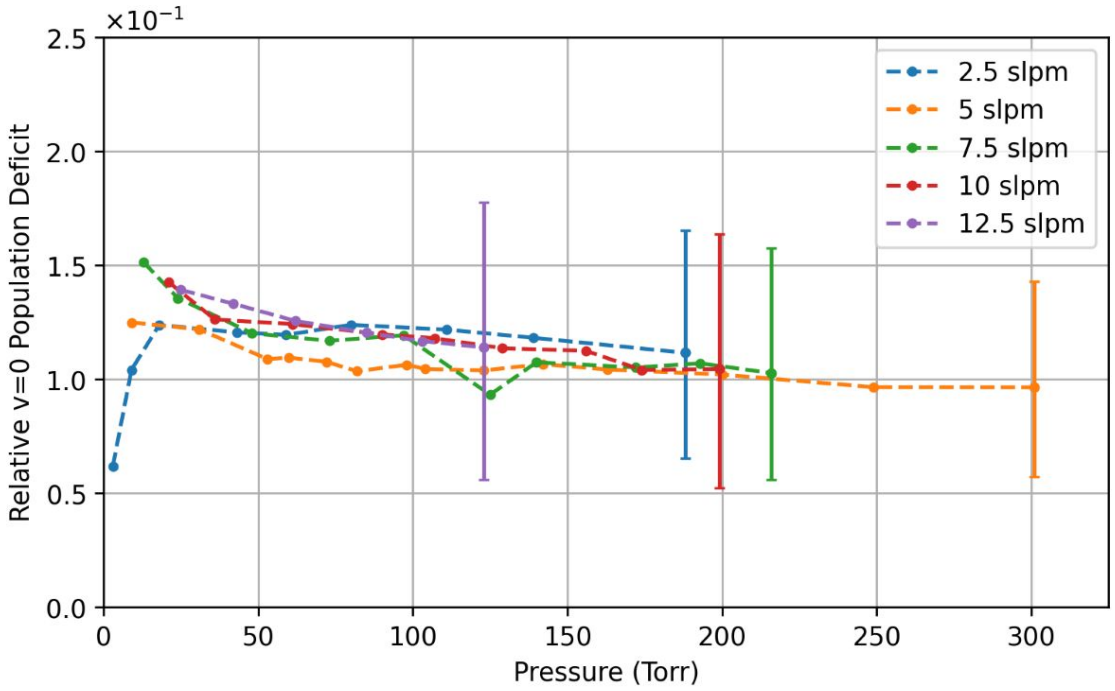

Figure 3.12: Deficit in the calculated relative population of the v=0 state compared to a Boltzmann distribution of temperature T_{vib}(v=1,2) against pressure for all examined flow rates. Uncertainties propagated from the error of measured vibrational temperature.

To assess the contribution of these $N_2(A)$ state pathways, Figure 3.12 plots the deficit caused by the underpopulation of the $N_2(C)$ state v=0 level against pressure for all examined flow rates. At low pressure, high electron temperatures likely experienced by the 2.5 slpm discharge are evidenced by the remarkably lower vibrational ground state deficit compared to higher pressures and flow rates, corresponding to a greater share of $N_2(C)$ molecules produced by direct excitation of the $N_2(X)$ ground state. For the rest of the examined pressure range, the deficit exhibited across flow rates agree within uncertainties, though given the consistently similar values for all flow rates these uncertainties are likely overestimated. The deficit trends slightly downward with increasing pressure, despite the electron temperature following a similar decay. Such a trend in electron temperature would favour production via the $N_2(A)$ state and thus an increased population deficit according to the model presented above. This indicates an additional factor influences which pathways dominate $N_2(C)$ production in the discharges studied here compared to the low pressure, low power discharges previously examined.

An additional factor is also necessary to explain the vibrational equilibrium observed in the plume. Lacking the driving fields of the antenna, the electron temperature in the plume is expected to decrease until it reaches equilibrium with the vibrational

temperature [97, 98]. These temperatures range from ∼0.2-0.4 eV, significantly lower than those modelled for the source region (see Section 4.1.1 in the following Chapter) and similar to those present in the afterglow in Ref. [13].

The N_2(A) state is very long lived with a radiative lifetime of 1.27 s [102]. The share of molecules in the N_2(A) state in the afterglow is therefore determined by the electron temperature of the active discharge rather than the instantaneous electron temperature alone. Thus, the plume of this device sees a lower share of molecules in the N_2(A) state than the afterglow of Ref. [13], and so sees lower rates of N_2(A) molecules colliding with either another of the same state or an electron. Instead, the metastables experience frequent collisions with ground state molecules, resulting in vibrational quenching or, less frequently, dissociation [103]. This reduces the contribution of N_2(C) production mechanisms that skew the vibrational population distribution away from equilibrium, likely accounting for the slight decrease in population deficit with increasing pressure in Figure 3.12.

In order for this factor to account for an equilibrium vibrational distribution being present in the plume but not the source, the latter must experience a significantly higher electron density and thus electron-N_2(A) collision rate.

3.3.2 Source Region N_2(C) T_{vib}

Figure 3.13 shows vibrational temperatures fitted from spectra captured in the source. The most significant finding from these results is the presence of a non-Boltzmann population distribution across vibrational energy levels, necessitating a fitting using several temperatures. Section 3.3.1 examines this behaviour in more depth.

The figure shows that both vibrational temperatures fitted to the captured spectra increase with flow rate for almost all examined pressures. This is especially true of the high temperatures corresponding to the v=0 populations, which sees only the lowest pressure 12.5 slpm data point buck this trend. As the power available per molecule is expected to decrease with increasing flow rate, such a correlation is noteworthy. At low pressures, high flow rates exhibiting high vibrational temperatures supports the previously presented evidence that these flow rates see less gas flow actually passing through the peak heating region compared to lower flow rates. At high pressures, however, this inversion in effective flow rate is no longer clearly evident, and thus cannot account for the greater vibrational excitation observed.

One possible explanation for these trends is that electron temperature increases with flow rate. The typical electron temperature of a high-pressure inductively-coupled

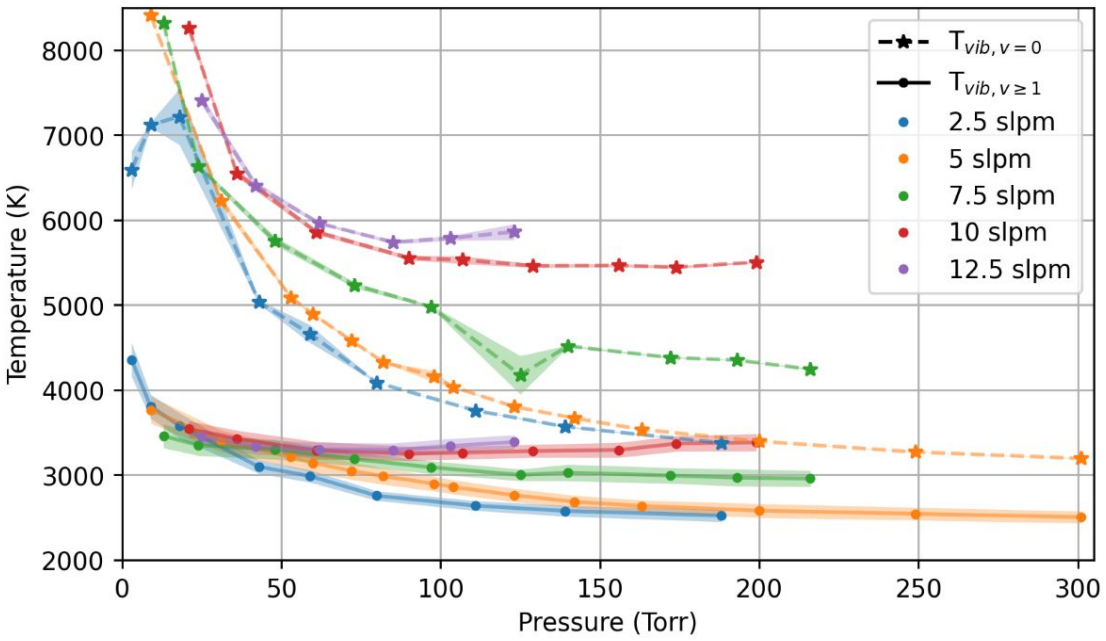

Figure 3.13: N_2(C) vibrational temperatures measured in the source region against pressure. Two temperatures are used to describe the non-Boltzmann population distribution observed across vibrational states.

discharges sits around 1 eV. In molecular nitrogen this is most resonant with the spacing of vibrational energy levels, producing strong coupling into the vibrational mode. Thus, a higher vibrational temperature can be indicative of higher electron temperature. This partially aligns with a mechanism suggested to account for source region gas temperature trends in Section 3.2.1, which required electron temperature to increase with flow rate at higher pressures. Higher electron temperatures may arise in higher flow rates due to increased ion loss fluxes, which is discussed in Section 4.1.1.

The population of the v≥1 levels is dominated by contributions from the N_2(A) state. As this is an already excited state, and its potential curve is offset relative to those of the ground and (C) state, the temperature of the v≥1 levels will therefore significantly overestimate the vibrational temperature of the ground state. This allows N_2(C) $T_{vib,v\geq1}$ to serve as an upper bound on the average vibrational temperature of the discharge. Comparing the temperatures measured for the 10 and 12.5 slpm cases at pressures above ∼75 Torr with this in mind, the suggestion made in Section 3.2.1 that increased vibrational mode relaxation may account for increases with pressure observed in source region gas temperature, provided higher flow rates exhibit significantly higher vibrational temperatures, does not hold.

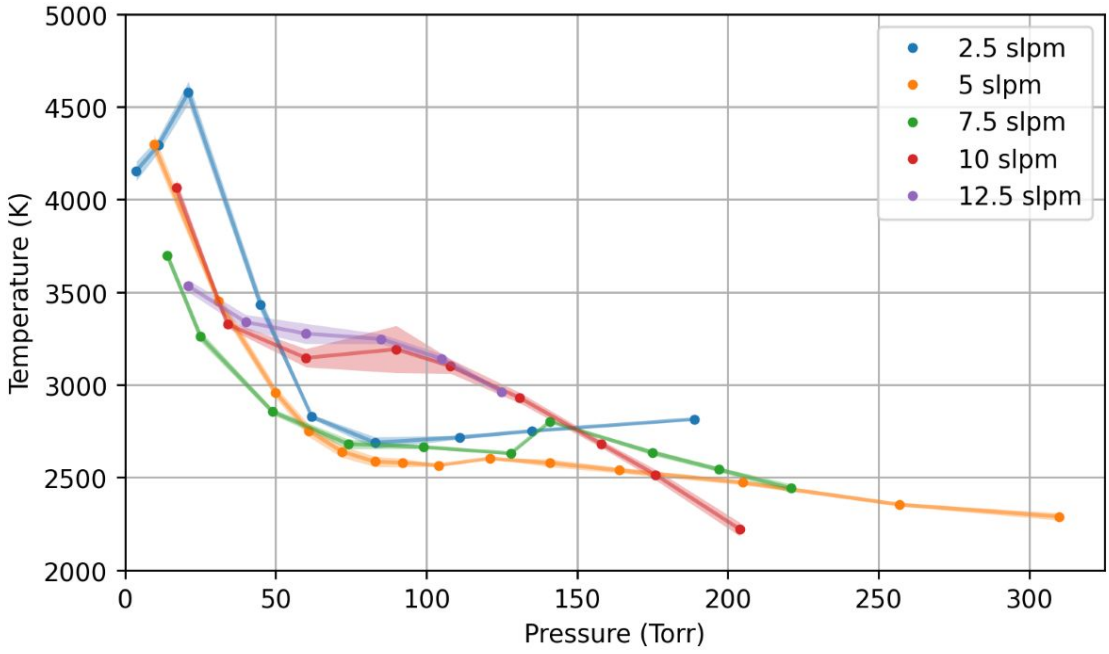

Figure 3.14: $N_2(C)$ vibrational temperatures measured in the plume against pressure.

3.3.3 Plume $N_2(C)$ T_{vib}

$N_2(C)$ state vibrational temperatures captured in the plume are presented in Figure 3.14. Importantly, unlike in the source region, the vibrational population downstream follows a Boltzmann distribution, allowing for a single-temperature fitting. The results of these fittings are closer to those found in the source for the higher vibrational levels rather than lower. Given that the $N_2(C)$ vibrational temperature correlates with that of the ground state when not dominated by contribution from the $N_2(A)$ state, this result aligns with the previously discussed expectation that $T_{vib,v\geq1}$ provides an upper limit to the ground state vibrational temperature.

The 10 and 12.5 slpm discharges exhibit trends with respect to pressure that differ significantly from those of lower flow rates. Both groups of flow rates exhibit a plateau behaviour, though for the higher rates this occurs between ∼40 and ∼80 Torr while the lower rates continue declining until ∼70 Torr. After their plateau the temperatures of the 10 and 12.5 slpm discharges decrease with similar rates and values, while the other flow rates diverge following gentler gradients. Due to these differing gradients, by 200 Torr the 10 slpm case exhibits the lowest downstream vibrational temperatures of all flow rates despite having the highest upstream vibrational temperatures at the same pressure. This poor correlation between temperatures in the two regions indicates that the electron temperature of the plume follows a different trend to that of the source region, which is unsurprising given the lack of a driving

field accelerating electrons in the plume.

The plateau exhibited by the 10 and 12.5 slpm cases occur in the same pressure range as, and thus may correlate to, plume gas temperatures that exceed those present in the source. Both results may emerge from the same underlying mechanism, one which elevates all downstream temperatures, rather than from energy coupled out of the vibrational mode. The lack of a similar plateau in the vibrational temperatures of the 7.5 slpm case is notable, given that it exhibits the same evidence of gas heating in the plume as the 10 and 12.5 slpm flow rates. The similarity in both the values and trends of downstream vibrational temperatures across the two flow rate groups, higher and lower, suggests this lack of a plateau may be due to these temperatures being strongly sensitive to some discharge parameter, producing a step function-like response. This is supported by the rapid increase in temperature between 130 and 140 Torr exhibited by the 7.5 slpm case, which takes the flow rate from temperatures in line with the 5 slpm case up to those of the 10 slpm case. Following this change, the 7.5 slpm flow rate sees stronger declines in vibrational temperature with pressure compared to the 5 slpm case, also in line with, though not as strong as, the response exhibited by the 10 slpm case.

The strong decreases of vibrational temperature with pressure evident in the 10 and 12.5 slpm cases above ∼100 Torr and the 7.5 slpm case above ∼150 Torr differ significantly from the slight increase and slight decrease with pressure exhibited by the 2.5 and 5 slpm cases, respectively. This divergence occurs over pressure ranges where the collision rate is calculated to stay relatively constant. This suggests the differences between flow rates cannot be attributed to differing rates of energy coupling out of the vibrational mode, as that is facilitated by intermolecular collisions. Instead, it may be evidence of vibrational quenching. In this discharge, this would most likely occur through the presence of atomic nitrogen, which has been observed to significantly increase the vibration-translation relaxation times of molecular nitrogen flows [104]. This possibility is assessed in Section 3.5.2.

3.4 N_2^+(B) Temperatures

Captured spectra including the First Negative system were used to determine the rotational and vibrational temperatures of the N_2^+(B) state of the molecular nitrogen ion. The results of these temperature fittings are presented in this section, starting with the source region, followed by the plume.

3.4.1 Source Region

Figure 3.15 shows the rotational and vibrational temperatures determined for $N_2^+(B)$ molecules in the source along the device axis. Once again, the 2.5 slpm case sees very high temperatures at the lowest examined pressures, where RF efficiency and electron density are notably higher than other flow rates. These high temperatures quickly drop as pressure increases to ∼12 Torr, where both temperatures are comparable with the values measured in higher flow rates. These results are likely correlated to the high electron temperatures the low flow rate experiences due to the low densities it achieves, as well as the low collision rate of the examined pressures allowing $N_2^+(B)$ states to decay before equilibration occurs between rotational and translational temperatures. Interestingly, however, the rotational temperature of the 2.5 slpm case at ∼6 Torr remains notably higher that that measured in the 5 slpm case despite the predicted electron temperature being slightly higher for the higher flow rate discharge. rate exhibits higher temperatures, despite having a lower predicted electron temperature. This may indicate that uncertainties were significantly underestimated for temperatures determined from spectral fitting, or that the densities determined using measured pressure and neutral temperatures may be inaccurate, impacting the accuracy of predicted electron temperatures. The latter possibility may be especially likely in this case as ion density would be expected to concentrate in the hottest portions of the plasma more strongly than $N_2(C)$ states, thus the temperature determined using emissions of the latter may overestimate the density in the plasma core.

By ∼12 Torr, the 2.5 slpm discharge sees both temperatures fall below those of the 5 slpm discharge, and both follow a similar trend line for the remainder of pressures examined. Beyond ∼100 Torr, the vibrational temperature trend line increases with increasing pressure, despite both the electron temperature and $N_2(C)$ vibrational temperatures declining with pressure. This is in contrast to the 7.5 slpm case, which sees a reduction in vibrational temperature over the same pressure range that results in significant convergence of the two temperatures of the discharge. The difference in behaviour between the lower and higher flow rates and the pressures at which these differences occur align with the electron density plateauing and its subsequent impacts on plasma parameters identified in the previous chapter. Higher electron densities facilitate greater energy flow into the vibrational modes of molecules due to seeing more frequent collisions. This effect is not reflected in the $N_2(C)$ vibrational temperature results previously examined however, thus is unlikely to account for the differences presented here.

Another notable difference between the temperatures determined for the $N_2^+(B)$

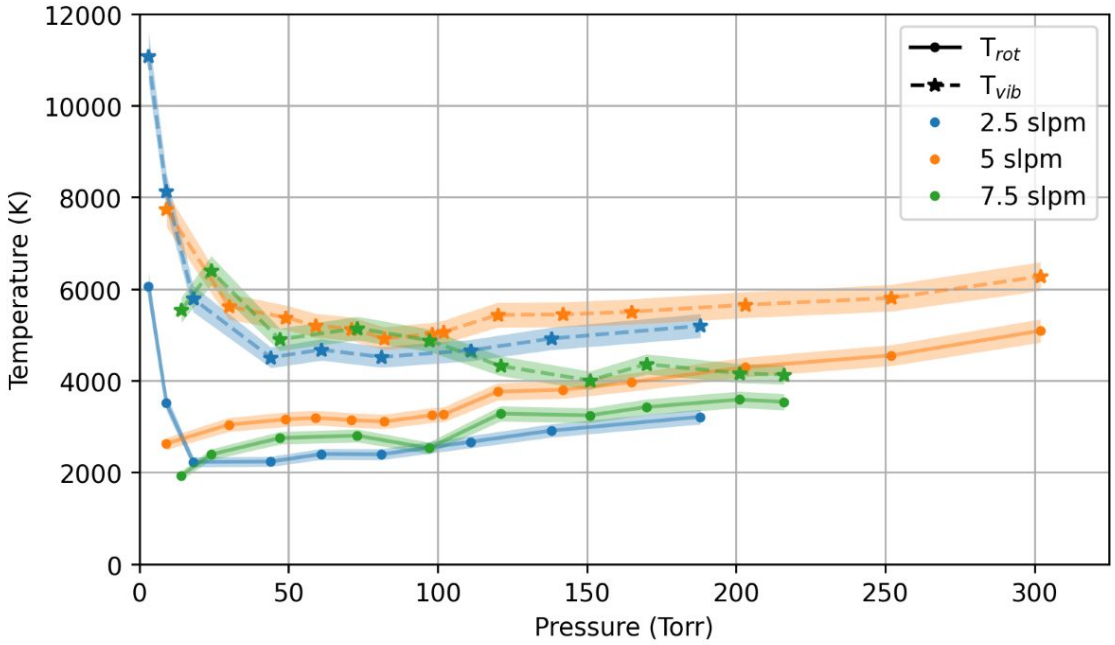

Figure 3.15: Source region N_2+(B) rotational temperatures (circles) and vibrational temperatures (stars) against pressure.

and N_2(C) states is the former's significantly higher rotational temperatures, which range from 2 to 3 times those of the latter. The two states exhibit very similar rotational constants, meaning that their rotational temperatures would be expected to equilibrate with gas temperature in approximately the same amount of time [73]. Both states exhibit similar radiative lifetimes, with N_2^+(B) taking approximately 50% longer to decay, allowing gas temperatures to be determined using its rotational bands in discharges at lower pressures than the N_2(C) state. The rotational temperature of N_2^+(B) is commonly used in the literature to determine gas temperatures in plasmas with relatively high ionisation rates [73], and has been compared to N_2(C) state rotational temperatures from the same discharge to evaluate the difference between peak and bulk plasma temperatures [105].

The significantly higher temperatures found with the N_2^+(B) state in this work cannot be attributed purely to the correlation between ion density and peak plasma heating, however. In the previously cited works, nitrogen was used as a trace gas in the discharges studied, the bulk of the feed gas being another species. In such conditions very few collisions occur between nitrogen ions and molecules. This is necessary to preserve the validity of the N_2^+(B) rotational temperature as a measure of gas temperature, as the state experiences significant quenching through collisions with neutral nitrogen molecules. When such quenching occurs, an N_2^+(B) ion undergoes

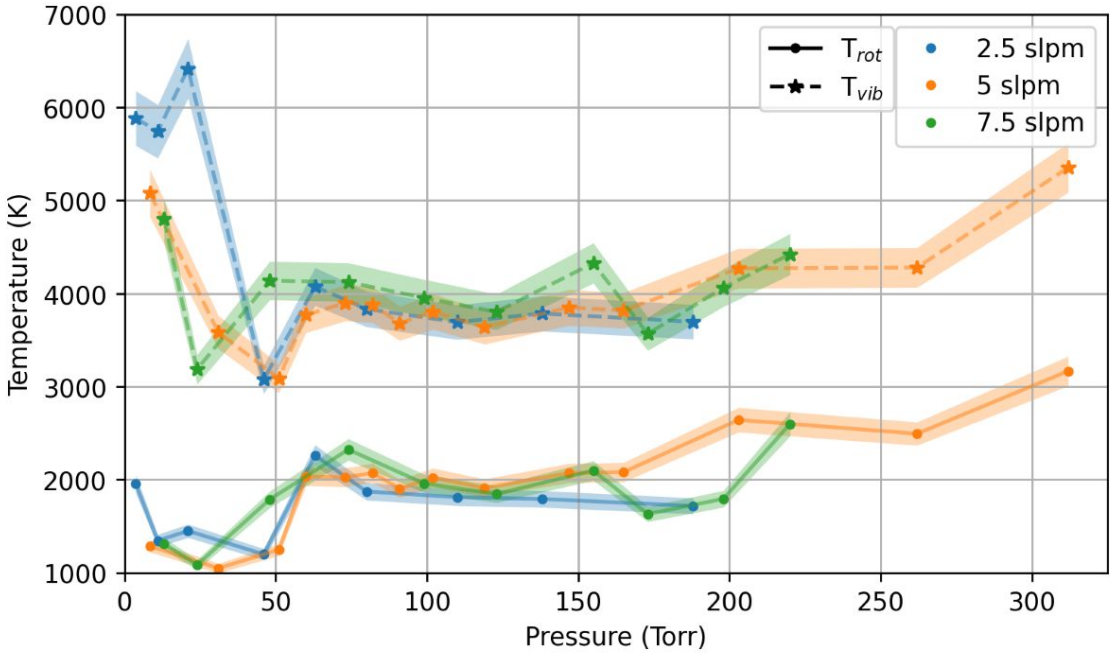

Figure 3.16: Plume N_2+(B) rotational temperatures (circles) and vibrational temperatures (stars) against pressure.

non-radiative de-excitation, preventing it from contributing to the First Negative system emissions. Therefore, in a pure nitrogen plasma, the same collisional processes that is necessary to equilibrate the state's rotational temperature with the gas temperature has a significant chance of preventing any emission occurring at all. As a result, the spectrum emitted is skewed toward the contributions of the small population of ions that decay prior to experiencing such collisions [106]. Fittings of these emissions therefore overestimate the gas temperature, with the degree of overestimation increasing as collisionality increases. Such an effect is not present for Second Positive system emissions in pure nitrogen discharges because while the radiative lifetimes of the upper states are similar, the quenching rate of the $N_2(C)$ state by neutral molecules is significantly lower than that of the $N_2^+(B)$ state: the quenching rate factors at 300 K are 1.1 $\times 10^{-17}$ $m^3s{-}1$ for $N_2(C)$ [107] compared to 8.8 $\times 10^{-16}$ $m^3s{-}1$ for $N_2^+(B)$ [108].

3.4.2 Plume

Figure 3.16 shows the temperature trends for ions in the plume across flow rates and with respect to pressure. Compared with upstream ion temperatures, both the trends and the temperature values themselves are very consistent across flow rate. Once again a low pressure spike is present in the 2.5 slpm vibrational temperature,

though interestingly the high values persevere and even strengthen with initial increases in pressure, diverging from the behaviour exhibited in the source. A similar behaviour of an initial high temperature for the lowest examined pressure is repeated in the 5 and 7.5 slpm cases, before a sharp decline with pressure followed by another sharp increase up to a steady value. While all three flow rates exhibit this trend, the pressure at which it occurs differs between them, with the 7.5 slpm case seeing both a decline and increase at lower pressures than the 2.5 and 5 slpm cases. This behaviour is somewhat repeated in the rotational temperature, with the 7.5 slpm case seeing an increase of almost Kelvin before 50 Torr, while the lower flow rates see the same increase slightly above 50 Torr.

Due to the brief radiative lifetime of the N_2^+(B) state and the effect of quenching discussed in the previous section, the excited ions producing the First Negative system emissions captured in the plume must be generated in the plume. Thus the low temperatures present across flow rates in low temperatures may be reflective of a low downstream electron temperature. The pressures at which steep temperature increases and subsequent plateaus are present correspond to relatively steady increases in neutral temperatures measured in the plume. Thus the ion temperatures observed do not reflect underlying changes in collision rate that would rapidly vary quenching rates. It is possible this difference corresponds to a sudden rise in downstream electron temperature, which could be produced due to changes in flow behaviour ejecting electrons rather than constraining them. However, any such increase would likely also be reflected in the N_2(C) state vibrational temperature, no evidence of which can be seen. Alternatively, if electron temperature stayed relatively steady while the population of N_2^+(X) ions increased, the dominant production mechanism of N_2^+(B) in the plume may shift from simultaneous ionisation and excitation of neutral molecules toward excitation of the ground state ion. Such a change would leave more energy for excitation of vibrational and rotational modes, producing increases in N_2^+(B) state temperatures without impacting N_2(C) state temperatures.

Beyond ∼50 Torr, both the vibrational and rotational temperatures of the ion remain relatively steady. This plateau behaviour suggests the non-thermalised rotational temperatures of newly excited N_2^+(B) states decrease at a rate that largely offsets the increasingly strong selection effect favouring these temperatures produced by increased quenching rates. This could emerge due to decreasing electron temperatures. Alternatively it could be a result of the exhaust velocity decreasing with pressure, resulting in the transverse optical access imaging an older and thus more recombined portion of the plume that has thermalised to a greater degree.

Beyond small divergences, the temperatures observed across flow rates differ little

for the entire examined pressure range. Some variability is evident in the 7.5 slpm case, especially from 150 Torr and up, though this is may be due to uncertainty in the subtraction of neutral contributions from the First Positive system emissions. Some divergence between the 2.5 and 5 slpm cases may be present between 150 and 200 Torr, as the rotational and vibrational temperatures of the 2.5 slpm case remain steady, while both 5 slpm case temperatures increase. Without higher pressure data points, little can be concluded regarding this divergence, however it may indicate that the departure of the 5 slpm case from the steady temperature values correlates to surpassing the pressure at which peak RF efficiency for the flow rate occurs. Such analysis would suggest that the variation in temperatures of the 7.5 slpm case above ∼120 Torr is evidence of a similar behaviour.

3.5 Evaluation of Thermal Characteristics

This section presents measurements of coolant water temperatures, and calculations of rotational/translational enthalpies, vibrational enthalpies, and thermal efficiency. The mechanisms suggested throughout this chapter to explain observed trends in temperatures are assessed in light of these measurements and calculations. The most likely source of the excess energy resulting in gas heating in the plumes of high flow rate discharges is determined.

3.5.1 Coolant Water Temperature

A proxy for heat lost to the walls was measured by recording the steady-state cooling water outlet temperature achieved by the chiller for each examined discharge. Upon ignition the plasma was run at its starting pressure until the chiller output temperature stabilised. While scanning pressure, for each discharge condition this temperature was once again allowed to stabilise before spectra were captured and recordings taken.

Figure 3.17 shows the chiller output temperature against pressure for the examined flow rates. The 2.5 slpm and 5 slpm flows see sharp increases in chiller output temperature with pressure at low pressures. Additionally, the initial chiller temperature of the 2.5 slpm case is notably higher than the other examined flows. This occurs while that flow rate sees the highest observed power transfer efficiency (see Section 4.2.2 in the following chapter) of any examined conditions in the device (85%), thus any abnormally high heating contribution from the coil itself can be ruled out.

The other flow rates, by comparison, have significantly lower chiller temperatures at ignition. Among them, higher flow rates increase notably more slowly with pressure

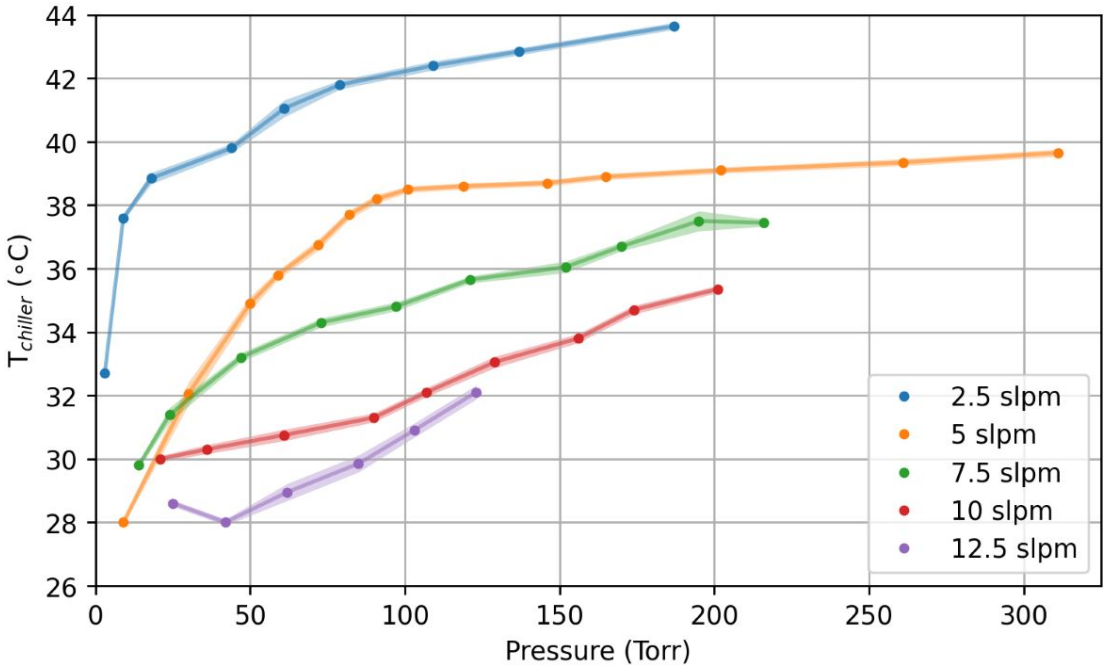

Figure 3.17: Steady-state coolant water output temperatures achieved by the chiller, plotted against pressure.

than the lower flow rates. The 5 slpm case increases quickly and consistently with pressure initially, before slowing down considerably around 100 Torr, with a only small transitionary curve between the two trends. The 7.5 slpm case, by comparison, starts with a gentle curve, increasing more slowly with pressure before also levelling off to a roughly linear trend at 100 Torr, though one steeper than that of the 5 slpm case. Of the pressure range examined in the 10 and 12.5 slpm cases, no curves are evident, instead the produced temperatures increase approximately linearly with pressure. This diversity in trends yields an especially large difference in chiller temperatures in the range of 50-100 Torr, after which the higher flow rates see chiller temperatures increasing faster than the 5 slpm case, thus partially closing the gap.

These chiller output temperatures are strongly correlated to the heat load to the walls of the source region. Thus, figure 3.17 suggests that the conductive and convective heat losses in the device increase with gas flow rate and decreases with pressure. This rules out the suggestion made in Section 3.2.1 that the trends in source region gas temperature could be produced by high flow rates experiencing significant heat losses at low pressures that decrease as pressure increases.

3.5.2 Vibrational-Translational Relaxation

With evidence of equilibration between the vibrational and rotational modes identified, the measurements finding higher gas temperatures in the plume than the source can be revisited. Contributions to total gas enthalpy from the rotational and vibrational modes can be calculated for both examined regions and compared in order to assess the approximate share of energy originating as vibrational excitation that is transferred into thermal energy. The rotational enthalpy flow is given by

$$\dot{H}_{rot} = \dot{n}_{N_2} \left(\int_{T_{in}}^{500} c_{p,1}(T)\, dt + \int_{500}^{T_{rot}} c_{p,2}(T)\, dt \right) \tag{3.5}$$

where $\dot{n}_{N_2}$ is the gas flow rate in mols^{-1} and T_{in} is the temperature of injected gas, taken to be equal to the temperature of the inner source tube and thus the cooling water. $c_{p,1}(T)$ and $c_{p,2}(T)$ are specific heat capacity functions for molecular nitrogen gas above and below 500 K, respectively, constructed using fittings provided in Ref.[109]. T_{rot} is the rotational temperature of the plasma, measured in either the source or plume.

Vibrational enthalpy flow was calculated by assuming it to be equal to the change in vibrational energy of a quantum harmonic oscillator, given by [71]

$$\dot{H}_{vib} = \dot{E}_{vib} = \dot{n}_{N_2} \frac{R\Theta_v}{e^{\Theta_v/T} - 1} \tag{3.6}$$

where R is the gas constant and Θ_v is the characteristic vibrational temperature for nitrogen gas, equal to 3352 K, calculated according to $\Theta = \frac{hv}{k}$ where h is the Planck constant and v is the natural frequency of vibration for nitrogen gas, sourced from Ref. [110].

Two assumptions are employed: the entire gas flow is heated to the measured rotational and vibrational temperatures, and the v≥1 vibrational temperature of the $N_2(C)$ state reflects the overall vibrational temperature for neutral particles in the source. While the first assumption is unlikely to reflect reality, it is applied to both enthalpy contributions, meaning even if the enthalpy values produced are inaccurate the ratio between them is valid for each flow rate. The second assumption likely overestimates the overall vibrational temperature, as studying $N_2(C)$ states select for molecules that have experienced ro-vibrational excitation. However, given that the electron temperature is far lower than excitation or ionisation energies and the propensity for nitrogen to undergo vibrational energy pooling, it is possible for ground state molecules to achieve similar levels of vibrational excitation.

Figure 3.18 shows the enthalpy difference between upstream and downstream mea-

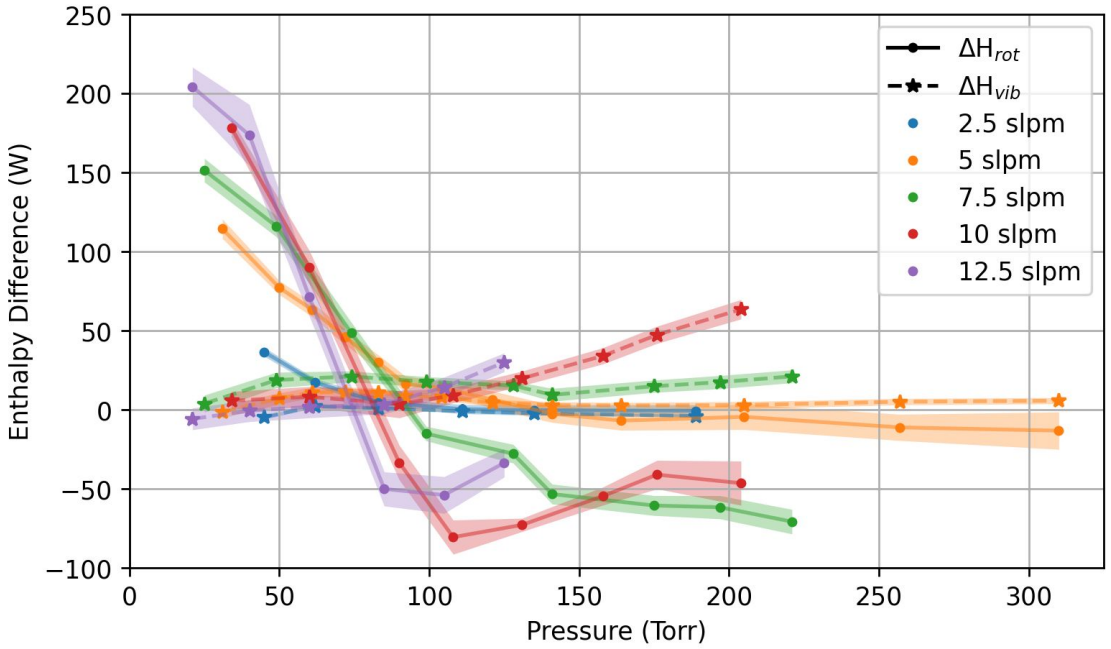

Figure 3.18: Difference between the source region rotational and vibrational enthalpies and those of the plume, plotted against pressure. Positive values indicate enthalpy is higher in the source region, negative values indicate the plume enthalpies are higher.

surements against pressure, separated by excitation mode. Positive values indicate higher source enthalpies and negative values higher plume enthalpies. If equilibration accounted for all energy flow into the plume neutral gas temperature for a given flow rate, its negative rotational enthalpy difference values would be offset by positive vibrational enthalpy differences of the same magnitude. Examining the figure this is clearly not the case for most flow rates, as only the 10 slpm discharge sees positive vibrational enthalpy differences of the same order as its rotational enthalpy differences, and only at the highest examined pressures. This is despite the likely overestimation of vibrational enthalpy differences by using the $N_2(C)$ temperatures. The pressures which see the most significant imbalances of rotational enthalpy toward the plume see comparatively minute differences in vibrational enthalpy, indicating that the large bulk of downstream heating must originate from an energy mode other than vibration.

The results of the 10 slpm case nonetheless suggest that at higher pressures (or perhaps in portions of the plume more distant from the source) high downstream rotational temperatures may be maintained by equilibration from the vibrational mode. The slight increase in rotational temperature observed for this flow rate at ∼200 Torr reverses a consistent downward trend, at a pressure where a strong

upward trend in the vibrational temperature difference is present. This suggests that as pressure increases, heat flow from vibrational equilibration may rise to offset and potentially exceed thermal losses. This could be caused by the time-of-flight for the imaged portion of the plume increasing with pressure, allowing more nitrogen molecules to experience vibrationally-relaxing collisions with atomic nitrogen.

These findings further support the possibility of vibrational quenching occurring in the plume, suggested in Section 3.3.3. Revisiting the results of this section, the observed trends indicate that the density of atomic nitrogen increases with flow rate at high pressures. Atomic nitrogen can be produced by electron-ion recombination reactions [111]:

$$N_2^+ + e^- \rightarrow N + N,$$

or by collisions between vibrationally excited neutral molecules [103]:

$$\begin{aligned} &2N_2(14 \leq v \leq 25) \rightarrow N_2 + N + N, \\ &N_2(A) + N_2(14 \leq v \leq 19) \rightarrow N_2 + N + N, \\ &N_2(43 \leq v \leq 45) + N_2 \rightarrow N_2 + N + N \end{aligned}$$

Its is plausible that atomic nitrogen production through either pathway increases with flow rate. Ions in the source region are subject to inertial forces produced by the gas flow, and therefore are more likely to be carried into the plume by the higher velocities present in higher flow rates. Similarly, the population of highly vibrationally excited molecules is determined by the vibrational temperature of a discharge, which was measured to be higher for higher flow rates in both the source and the plume. A key consideration, however, is that the electron-ion recombination pathway also provides a source of excess energy to the plume, which could also account for some portion of the gas heating observed in the plume. Each recombination reaction releases a minimum of 5.74 eV [103], equal to the difference between the ionisation and dissociation energies of molecular nitrogen. This energy is stored in ions in the source, and only becomes available for thermal excitation after recombination in the plume.

Unfortunately, direct evidence of electron-ion recombination, by way of the presence of atomic nitrogen in the plume region, could not be captured using the employed OES set-up for conditions examined in this work. This is due in part to the low ionisation rates present in such RF ICPs, leading to low concentrations of atomic nitrogen after recombination. These low concentrations couple with comparatively low electron densities, particularly in the plume, to result in the rate of collisions between nitrogen atoms and electrons being negligible and effectively preventing

the creation of nitrogen ions. This rules out any spectral contributions originating from atomic nitrogen within the examined wavelength ranges [112]. Near-infrared emission lines originating from electronic transitions of the neutral atom could not be imaged due to both overlap with the first positive system of molecular nitrogen and a significant, unexplained drop in optical efficiency of the OES system. Future work may be able to overcome these limitations, or use a higher-resolution set-up to examine low-intensity atomic transition lines in the near-UV range [113]. This work, however, must assess the impact of electron-ion recombination through the indirect evidence present in the temperature results presented in this chapter.

Energy released in electron-ion recombination reactions may account for the gas heating observed in the plume across all flow rates between 50 and 100 Torr. In this pressure range vibrational enthalpy holds relatively steady, ruling out significant equilibration from the vibrational mode. Therefore, this pressure range may image the portion of the plume undergoing recombination, during which ionisation energy is released as heat energy and the density of atomic nitrogen increases. As pressure increases and gas flow velocities decrease, the portion of the plume being imaged comes to reflect older, more fully recombined plasma with an increasingly large share of its vibrational energy coupled into translational energy via collisions between molecular and atomic nitrogen. As the total concentration of molecular ions in the plasma is low, so too is the concentration of atomic nitrogen. Thus the odds of collisions between nitrogen atoms are also low, resulting in these free atoms surviving well into the plume.

As vibrational equilibration is facilitated far more rapidly through collisions between molecular and atomic nitrogen than between only molecular nitrogen, the rate at which vibrational relaxation occurs in recombining plasma is therefore dependant almost exclusively on the number of nitrogen atoms formed during electron-ion recombination. Comparing the gradients exhibited by each flow rate in Figure 3.14 indicates that this relaxation rate and therefore the possible concentration of nitrogen atoms in the plume would be highest for the 10 and 12.5 slpm cases. In this case, the data indicates concentration would decrease with decreasing flow rate. This aligns with expectations of source region gas velocity, and thereby inertial forces in the source, decreasing with flow rate and expelling fewer ions into the plume.

3.5.3 Thermal Efficiency

An estimate for thermal efficiency of the device was calculated for all examined pressures and flow rates. Temperatures measured in the plume are used to calculate the enthalpy change of the working gas. Downstream temperatures are used due to the

additional heating observed compared with the source due to possible contributions from electron-ion recombination and vibrational-rotational relaxation. Using plume temperatures also serves to evaluate the device in line with its intended use as a source of heat in industrial applications.

As the spatial distribution of temperature in the plume is not known, the experimentally measured rotational and vibrational temperature values are used as an average temperature for all gas flowing through the device. This almost certainly results in an overestimation of thermal efficiencies for all flow rates, as the portions of gas flow nearest the device walls will exhibit lower temperatures as heat is lost to conduction. The closest and most consistent temperature fits were observed in the spectra captured downstream, however, which points toward one of two possibilities: either only a portion of the exhausted flow is hot enough to emit light and that portion exhibits a relatively flat distribution of temperature across it, or the temperature distribution of the entire flow is relatively flat with the measured temperatures likely corresponding to the highest present temperatures. The findings of this chapter suggest at low pressures the former is more likely the case, while at higher pressures the latter becomes and increasingly valid assumption.

Both the use of a reverse vortex gas injection and the design of the downstream injection region in which the optical access to the plume is located should encourage gas mixing and thus thermal equilibration across the flow. The vorticity of the fluid flow introduced by the reverse vortex is almost certainly preserved after the gas is exhausted, as a double-helix effect can be observed in the plume through the chamber window at low pressures, when the visible plume extends the furthest distance downstream. Thus, after expulsion from the source region, the azimuthal velocity of the gas provides a centrifugal force radially outward towards the walls, allowing at least a portion of the flow to hit the lower ledge of the injection region instead of passing immediately through the secondary choke. This gas could then form a second reverse vortex effect as it is pushed up the walls of the injector, insulating the rest of the flow from the walls and encouraging recirculation and potentially turbulence with the exhaust flow due to the difference in axial velocity, encouraging mixing and, with it, thermal equilibration. Thus, while optimistic, the assumption of a single representative temperature for the entire flow is not without justification.

Figure 3.19 presents these calculated thermal efficiencies. Significant correlation between thermal efficiency and both pressure and flow rate is evident. All flow rates see efficiency improve with pressure, though the 2.5 slpm case shows an early peak around 20 Torr that is not eclipsed by higher pressures. The higher flow

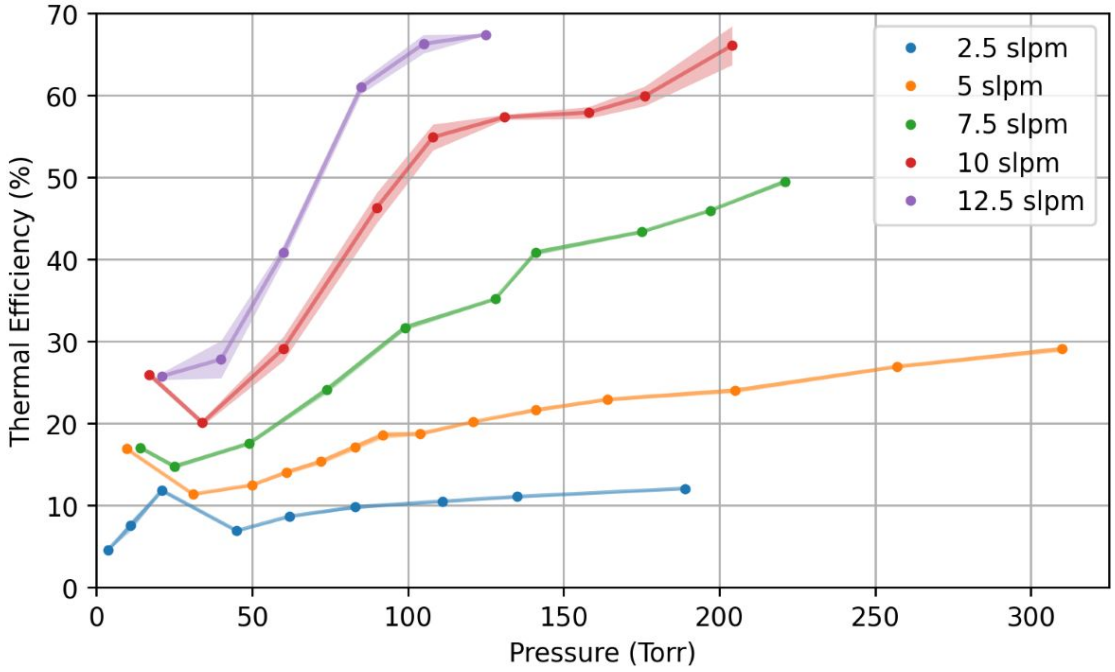

Figure 3.19: Estimated thermal efficiency of the device against pressure. Calculated assuming the entire flow through the torch is heated to the temperatures measured in the plume.

rates see greater improvement with pressure, especially the 10 and 12.5 slpm cases between 50 and 100 Torr. This unsurprisingly aligns with the pressure range where these flow rates see electron density plateau and rotational temperatures significantly increase. All but the 2.5 slpm case see the steepest gradients in this pressure range, corresponding to the strong decline in the difference in rotational temperature and enthalpy between the source and plume evident in Figures 3.8 and 3.18.

The assumption of a flat temperature distribution does much to benefit the calculated efficiencies of the higher flow rates, though the same effect applies to lower flow rates too. Thus, the values in the range of 5 to ∼12% for the 2.5 slpm case and 10 to 30% for the 5 slpm case can essentially be taken as upper limits on the thermal efficiencies of these operating conditions. A larger portion of the energy coupled into them therefore goes into waste heat and radiative emissions compared to discharges with higher flow rates. This aligns with the correlation between coolant water temperature and flow rate observed in Figure 3.17.

In the context of thermal efficiency, the beneficial impact of downstream heating possibly provided by higher ion losses into the plume in high flow rate discharges is apparent. While possibly complicating plasma stability at higher pressures due to impacts on electron density in the source, a higher rate of ion-electron recombination

compared with lower flow rates would result in a larger share of the total energy dissipated in the plasma being converted into thermal energy in the plume, as seen with higher flow rates exhibiting higher efficiencies. While the values presented in Figure 3.19 are effectively upper limits, it is promising for high flow rates that these limits are well over double that of the 5 slpm case for most of the examined pressure range, with the highest value observed in the 12.5 slpm case of ∼68% generally in-line with the highest share of energy going into both thermal output and radiative losses measured for the 13.56 MHz electrothermal thruster device [11]. This is despite this device exhibiting significantly higher residence times, and molecular nitrogen having a higher thermal conductivity than argon gas.

3.6 Summary

- The neutral gas collision frequency was calculated for all examined plasmas in the source and plume regions to determine the pressure ranges in which equilibration between the $N_2(C)$ state and molecular ground state can be assumed. This was determined to be ≥ 22 Torr in the source and > 17 Torr in the plume.
- Gas temperatures in the source were found to initially decrease with pressure before reaching a minimum and increasing again. The pressure at which this minimum occurred and the slope of the subsequent temperature increase approximately correlated with gas flow rate. The 5 slpm flow rate reached the highest temperatures overall (∼1715 K at 300 Torr), however at lower pressures the 2.5, 10 and 12.5 slpm flow rates reached temperatures 50-100 K higher than the 5 slpm case before extinguishing.
- Plume region gas temperatures saw rapid increases at low pressures, jumping from ∼600 K to up to ∼1400 K between 25 and 75 Torr. Higher flow rates experienced greater increases than lower flow rates. As pressure further increased, plume gas temperatures saw comparatively smaller increases, however the 5, 7.5 and 10 slpm cases saw upticks around ∼200 Torr.
- At higher pressures, all but the 2.5 slpm case saw plume gas temperatures exceed source temperatures for the same pressure. The pressure at which this occurs was found to decrease with increasing flow rate. Enthalpy flow calculations were performed to determine whether this may be indicative of equilibration between the vibrational and rotational modes. The results of which showed that the drop in vibrational enthalpy was signficantly smaller than the increase in rotational enthalpy for all but the highest examined pressures of the 10 and 12.5 slpm cases. Energy released from electron-ion recombination in the plume

was suggested as the most likely origin of the excess thermal energy observed downstream. The correlation between this heating, pressure and gas flow rate would suggest that higher flow rates experience greater rates of charged particle expulsion into the plume. This will be further examined in the following chapter.

- The $N_2(C)$ state was found to be in vibrational equilibrium in the plume, however in the source a non-equilibrium distribution consistent with under-population of the vibrational ground state was found. It was concluded that this non-equilibrium is likely caused by the low electron temperature of the examined discharges, resulting in significant step-wise excitation of the $N_2(C)$ state via the $N_2(A)$ state, which favours the production of vibrationally excited $N_2(C)$ molecules. The lack of such a distribution in the plume region indicates that both the electron-$N_2(A)$ collision rate and electron temperatures are so low that direct excitation of the ground state dominates $N_2(C)$ production in the region.
- Upper estimates of thermal efficiency were calculated, showing higher flow rates to have significantly higher maximum thermal efficiencies than lower flow rates. The 10 and 12.5 slpm cases both achieve peak efficiencies of $\sim$68%, comparable to arc discharge torches currently seeing industrial use. The correlation between flow rate and thermal efficiency may be further evidence of increased rates of electron-ion recombination in the plume, as energy spent sustaining higher electron densities in the source is instead thermalised in the plume, resulting in increased thermal efficiencies.

Chapter 4

Plasma Behaviour

In the previous chapter, evidence was found that in discharges with high flow rates, the source region of the device likely experiences significant losses of electrons and ions into the plume at high pressures. In this chapter, an analytical model of the discharge is developed to enable key plasma parameters, including electron density, to be calculated using the discharge properties measured in this work. The calculated electron densities are presented and evaluated with reference to measured power transfer efficiency. They are assessed for evidence of charged particle losses that increase with flow rate in order to verify the findings of the previous chapter.

Following this, measurements of time-varying oscillations in plasma parameters of discharges generated in the device are presented. This behaviour is discussed with reference to the results of both this and the previous chapter. A production mechanism for the oscillation is proposed and linked to the previously identified charged particle loss enhancement exhibited by higher flow rates.

4.1 Analytical Model

A model of the inductive discharge was developed to estimate plasma parameters using available experimental data. Such a process is commonly necessary in thermal plasma research due to the difficulty in implementing diagnostic techniques in the high-temperature, high-heat flux flows examined [114, 115]. In this work, a model was required to determine the electron temperature present in the discharge, which was necessary to calculated electron density values from measured plasma resistances. For simplicity the model was developed to be time-invariant and volume-averaged, meaning spatiotemporal variation of parameters within the reaction volume was almost entirely neglected. This allowed the many excitation pathways of nitrogen to be included in the model without necessitating computationally intensive kinetic modelling.

4.1.1 Electron Temperature Modelling

Using values determined in the previous chapter for for the neutral gas density in the source region (see Section 3.1), the electron temperature is modelled. Assuming the discharge is in a time-invariant steady-state, the rate of change of ion density must be equal to 0, meaning ion production balances ion losses. This allows an ion particle-balance equation to be constructed, which can be solved for electron temperature [4]. Ion losses are assumed to occur due to diffusion to the walls, where local plasma sheath effects accelerate them to the Bohm velocity, $u_B = \sqrt{\frac{eT_e}{M}}$, where e is the charge on an electron, T_e is electron temperature in eV, and M is the mass of an ion in kg. The number of ions lost per second is thus equal to the product of the average ion density at the plasma-sheath interface, the surface area of the plasma, and the Bohm velocity:

$$\Gamma_{loss} = n_i(2h_L A_L + h_R A_R)u_B \tag{4.1}$$

where n_i is ion density, $A_L = \pi R^2$ is the area of the circular cross-section of the plasma source region with radius R, $A_R = 2\pi RL$ is the surface area of the plasma facing alumina tube with length L, h_L and h_R are empirically-determined heuristics for the edge-to-centre plasma density ratios of cylindrical ICPs for the axial and radial dimensions, respectively. These are evaluated using [12]:

$$h_L = 0.86\left(3 + \frac{1}{2}\frac{L}{\lambda_i} + \frac{1}{5}\frac{T_i}{T_e}\left(\frac{L}{\lambda_i}\right)^2\right)^{-\frac{1}{2}} \tag{4.2}$$

$$h_R = 0.8\left(4 + \frac{R}{\lambda_i} + \frac{T_i}{T_e}\left(\frac{R}{\lambda_i}\right)^2\right)^{-\frac{1}{2}} \tag{4.3}$$

where T_i is the ion temperature, taken to be equal to the average gas temperature, and $\lambda_i = \frac{1}{n_g \sigma_i}$ is the ion-neutral mean free path with the ion-neutral collision cross section, σ_i, taken to be equal to 1.77×10^{-18} m^2 for molecular nitrogen [116].

Next, an expression for ionisation rate in the plasma bulk is found. Molecular nitrogen exhibits many multi-step ionisation pathways due to its numerous electronic vibrational states [117]. These states themselves can be excited in multi-step processes thanks to the stability of the N_2(A) first excited state and the poor energy coupling out of the vibrational mode [73]. Accurate calculation of rate factors for all possible ionisation processes would require intensive kinetic modelling considering population levels of several excited states and the vibrational states within them. Instead, for our purposes we make two simplifying assumptions:

- the impact of vibrational excitation on ionisation and electronic excitation rate can be neglected, and;
- the populations of electronic energy levels follow a Boltzmann distribution, with a temperature equal to the electron temperature.

The first assumption will likely result in an underestimation of ionisation rates as the share of electron-neutral collisions with sufficient energy to produce an ion is increased by vibrational energy pooling in neutral molecules [118]. The assumption of excitation-electron temperature equilibrium is supported by the excitation temperature measurements of Ref. [11] agreeing with expected electron temperatures in argon. Results of detailed kinetic modelling and experiments for discharges in argon-nitrogen mixtures in Ref. [119] indicate, however, that for conditions outside of total thermal equilibrium the populations of electronic excited states significantly exceed those predicted by the electron temperature. Electron and vibrational temperatures were in equilibrium under the conditions examined by that work, however, which likely contributes strongly to the overpopulation. Thus in the examined device, where vibrational temperatures are likely significantly lower than electron temperatures, the impact of vibrational pooling on electronic state populations will be reduced, improving the accuracy of the assumption made.

Employing the two assumptions allows the ionisation rate calculation to include contributions from the ionisation of excited electronic states without requiring explicit calculations of the their densities. Instead, the state densities can be expressed in terms of the electron temperature and neutral gas density. Including the three dominant electronic states of nitrogen, an equation for the ionisation rate is given by:

$$\Gamma_{iz} = n_g \left(K_{iz,X}(T_e) + e^{\frac{-E_{iz,A}}{T_e}} K_{iz,A}(T_e) + e^{\frac{-E_{iz,B}}{T_e}} K_{iz,B}(T_e) + e^{\frac{-E_{iz,C}}{T_e}} K_{iz,C}(T_e) \right) n_e V \tag{4.4}$$

where $K_{iz,j}(T_e)$ is the ionisation rate factor for state j, a function of electron temperature, $E_{iz,j}$ is the vibrational ground state energy of electronic excited state j, equal to 6.167, 7.351, and 11.03 eV for the A, B and C states, respectively [102], and V is the volume of the discharge region.

The ground state ionisation rate factor was determined by convolving energy-dependent cross section data with Maxwellian electron energy distributions characterised by electron temperature. Cross section data was sourced from Ref. [120], allowing for the calculated ionisation rate to include contributions from transitions between the neutral molecule ground state and the ground and first three excited states of the molecular nitrogen ion. For the ionisation of the three examined excited

states, rate functions determined by fitting Arrhenius equations to experimental data were sourced from Ref. [117].

With expressions determined for the rate of ion loss (Equation 4.1) and ionisation (Equation 4.4), they can be equated. Due to quasineutrality, $n_e = n_i$, allowing these terms to cancel out. This yields an ion particle balance equation that is a function of neutral gas density, average gas pressure, and electron temperature. By substituting in known values of gas density and temperature for each datapoint, the particle balance equation can be solved numerically to determine electron temperature.

4.1.2 Electron Density Calculation

Once electron temperature is determined, electron-energy dependent rate factors for a range of electron-neutral collisional energy exchange processes can be calculated. Rate factors are calculated for collisions producing rotational, vibrational and electronic excitation, as well as elastic scattering using the same process as the ground state ionisation rate in Section 4.1.1. Cross-section data for 34 collision processes producing rotational, vibrational and electronic excitations was sourced from Ref. [120]. Elastic scattering cross sections were sourced from Ref. [6]. These rate factors, in addition to the previously determined ionisation rate factors, are used to calculate the electron momentum transfer frequency, ν_m, given by:

$$\nu_m = n_g(K_{iz}(T_e) + K_{rot}(T_e) + K_{vib}(T_e) + K_{exc}(T_e) + K_{el}(T_e)) \tag{4.5}$$

This frequency is used to evaluate the plasma permittivity, given by [12]:

$$\varepsilon_p(\omega) = 1 - \frac{\omega_{pe}^2}{\omega(\omega - i\nu_m)} = 1 - \frac{\omega_{pe}^2}{\omega^2 + \nu_m^2} - i\frac{\nu_m}{\omega}\frac{\omega_{pe}^2}{\omega^2 + \nu_m^2} \tag{4.6}$$

where $\omega = 2\pi f$ is the angular frequency of the applied power (in this work, f=27.12 MHz), and ω_{pe} is the electron plasma frequency, the characteristic frequency with which plasma electrons respond to perturbations in local electromagnetic fields. This quantity relates plasma permittivity to electron density:

$$\omega_{pe} = \sqrt{\frac{n_e e^2}{m_e \varepsilon_0}} \tag{4.7}$$

where m_e is the mass of an electron and ε_0 is vacuum permittivity.

Using the electromagnetic model of an ICP discharge presented in Ref. [12], plasma

permittivity can be related to R_p, the contribution to the total resistance across the device coil originating from the plasma [65]:

$$R_p = \frac{2\pi N^2}{l_c \omega \varepsilon_0} \mathrm{Re}\left(\frac{ik_0 r_p J_1\left(\sqrt{\varepsilon_p} k_0 r_p\right)}{\sqrt{\varepsilon_p} J_0\left(\sqrt{\varepsilon_p} k_0 r_p\right)}\right) \tag{4.8}$$

where N is the number of turns in the coil and $k_0 = \frac{\omega}{c}$ where c is the speed of light. The same model provides the combined inductance of the plasma and antenna in a similar form:

$$L_{ind} = L_{coil}\left(1 - \frac{r_0^2}{r_c^2}\right) + \frac{2\pi N^2}{l_c \omega^2 \varepsilon_0} \mathrm{Im}\left(\frac{ik_0 r_p J_1\left(\sqrt{\varepsilon_p} k_0 r_p\right)}{\sqrt{\varepsilon_p} J_0\left(\sqrt{\varepsilon_p} k_0 r_p\right)}\right) \tag{4.9}$$

where $L_{coil} = \frac{\mu_0 \pi r_c^2 N^2}{l_c}$ is the inductance of the coil.

Thus, by evaluating Equation 4.5, Equation 4.6 can be substituted into Equation 4.8 alongside experimental measurements of the plasma resistance to allow the equation to be solved numerically in terms of the electron-plasma frequency, ω_{pe}. These values can then be related to electron density by Equation 4.7.

As evidenced in Figure 4.1, any experimentally measured plasma resistance will produce two valid solutions to Equation 4.8. These solutions correspond to different electron densities that produce the same plasma resistance. This occurs due to the skin depth growing shallower as electron density increases. Starting from low electron densities and large skin depths, as electron density increases a stronger current is induced in the plasma and a greater share of the strength of the coil fields are attenuated by electron motion, increasing plasma resistance. Resistance increases with electron density until reaching a maximum where the skin depth equals approximately $0.57R$. At this point, the antenna fields are entirely screened out only precisely along the axis, meaning the induced current flows throughout the entire plasma radius. Increases in electron density beyond this value further shrink the skin depth and the region through which induced current flows, resulting in increasing electrical conductivity and therefore decreasing plasma resistance.

For all discharges studied in this work, the lower electron plasma frequency and thus electron density were taken to be the correct value. This was determined by calculating electron densities corresponding to both solutions and comparing them to values determined in argon discharges in a similar device [11]. For the reasons discussed in Section 1.3, the power required to support a given electron density in argon will be lower than that required to support that same density in nitrogen, thus densities higher than those measured in argon can be ruled out.

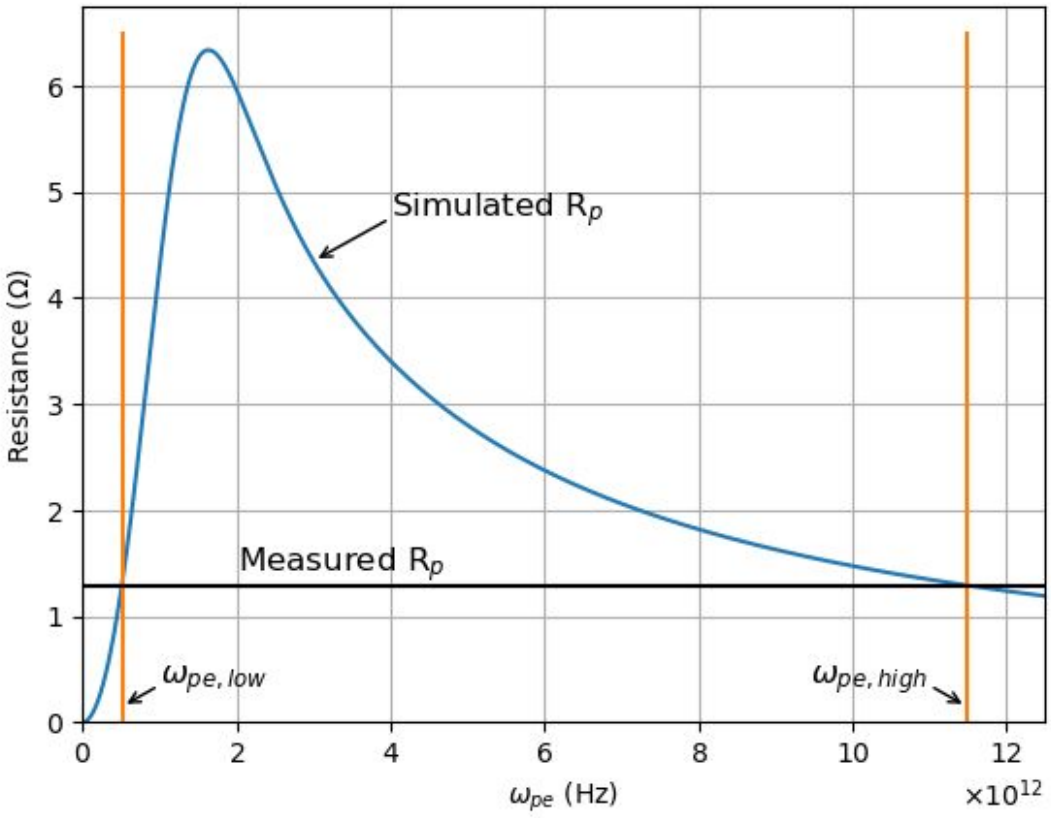

Figure 4.1: An example of solving for ω_{pe} using the measured plasma resistance. Two solutions exist where measured R_p equals R_p evaluated using Equation 4.8. These correspond to different electron densities that produce the same plasma resistance, the under-dense (low) and over-dense (high) scenarios.

This conclusion is supported by evaluations of the resistive skin depth, δ, which can be calculated for a known electron plasma frequency according to [12]:

$$\delta = \frac{c}{\omega_{pe}}\sqrt{\frac{2\nu_m}{\omega}} \tag{4.10}$$

Evaluating the skin depths of the higher frequency solutions to Equation 4.8 yields values smaller than 1 mm, which is not consistent with the axially-centred plasma ball observed in the device. Electron densities corresponding to the under-dense scenario are therefore taken to be accurate.

4.2 Plasma Parameters

This section presents the plasma parameters calculated for the discharges examined. Electron temperatures produced using the analytical model are reported and analysed with respect to flow rate and pressure. The measured power transfer efficiencies

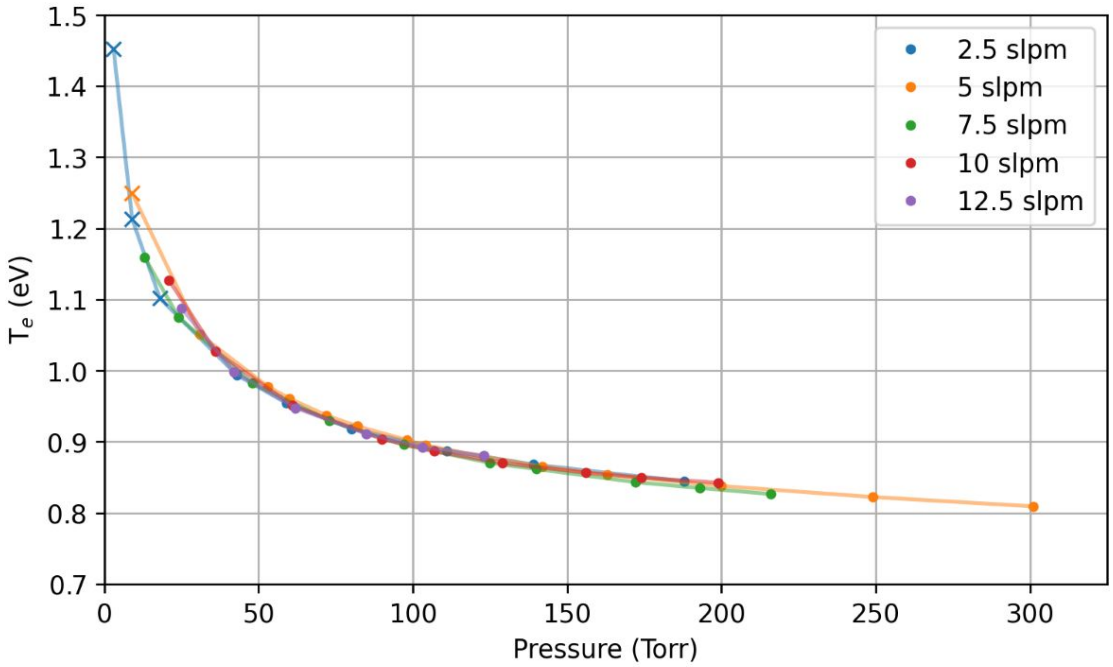

Figure 4.2: Electron temperatures determined by the model using experimental temperature and pressure measurements. Circles indicate values calculated using measured gas temperatures, crosses indicate values calculated assuming a gas temperature equal to that of the lowest pressure conditions for which a gas temperature could be measured for a discharge of the same flow rate.

are reported, followed by electron density. These results are evaluated for evidence of charged particle losses into the plume which increase with flow rate. The sensitivity of the observed electron particle balance equation on gas density is determined and compared to that predicted for discharges dominated by ion diffusion to the walls. The sensitivity of the modelled electron temperature and resulting electron densities to charged particle loss rates are assessed. Finally, values for the inductive skin depth for the discharge are presented and causality determined between power transfer efficiencies and achieved electron densities.

4.2.1 Electron Temperature

Electron temperature is determined by the balance of energy coupled into and out of free electrons. In a plasma with a low ionisation rate, the latter of these factors is largely determined by the neutral gas density by way of the electron-neutral collision frequency. It therefore follows that the electron temperatures calculated for the discharge, presented in Figure 4.2, see little variation across flow rates, similar to density and collision rate results. For pressures above 50 Torr, the electron

temperature can be taken as essentially constant across flow rate, though some slight deviations appear at higher pressures where the range of gas temperatures exhibited by discharges of different flow rates widen. At low pressures neutral density is more sensitive to temperature variations, and the modelled particle balance used to solve for electron temperature is more sensitive to temperature when neutral density is low. Pressures below 50 Torr thus produce the largest observed differences in electron temperature across flow rates with respect to pressure. These differences are relatively small, however, no greater than 0.05 eV.

Two sets of electron temperatures are presented, one calculated using the temperature measured on the device axis, the other using the average source temperature. For low pressure, non-thermal discharges with high mean free paths, electron temperature is typically relatively constant across varying radial distance to the axis. At higher pressures, increased collision rates reduce the mobility of electrons, allowing electron temperature to vary across the plasma radius. Nonetheless, the model used in this work assumes a single electron temperature is valid throughout the plasma bulk. In light of this, the electron temperatures calculated using the axial temperatures functions as an upper bound on overall electron temperature, rather than a localised value along the axis. The values calculated using average source temperature likely correspond more accurately to the electron temperatures present in the device.

The model determines electron temperatures using an ion particle balance, in which the only ion loss considered is thermal diffusion to the walls. Ions are subject to the inertial forces of bulk gas flow, however, and will therefore be ejected into the plume. This would result in higher ion loss rates that would necessitate higher electron temperatures to offset. Alternatively, the insulating layer of fresh gas established by the reverse vortex flow may result in fewer ions reaching the walls by thermal diffusion than predicted by the model. Neither the flow behaviour nor the ion density distribution are sufficiently well understood to allow the global model to quantify such changes to the loss mechanisms. It is most likely, however, that the changes to thermal diffusion would not offset the unaccounted for ion loss from plasma expulsion. Thus the calculated electron temperatures presented here are likely underestimates of those necessary to sustain the studied discharges.

4.2.2 Power Transfer Efficiency

Coil current, forward power and reflected power were recorded for every discharge, allowing calculation of the plasma power transfer (RF) efficiency over a range of gas flow rates and device pressures. Figure 4.3 shows efficiency against pressure in the

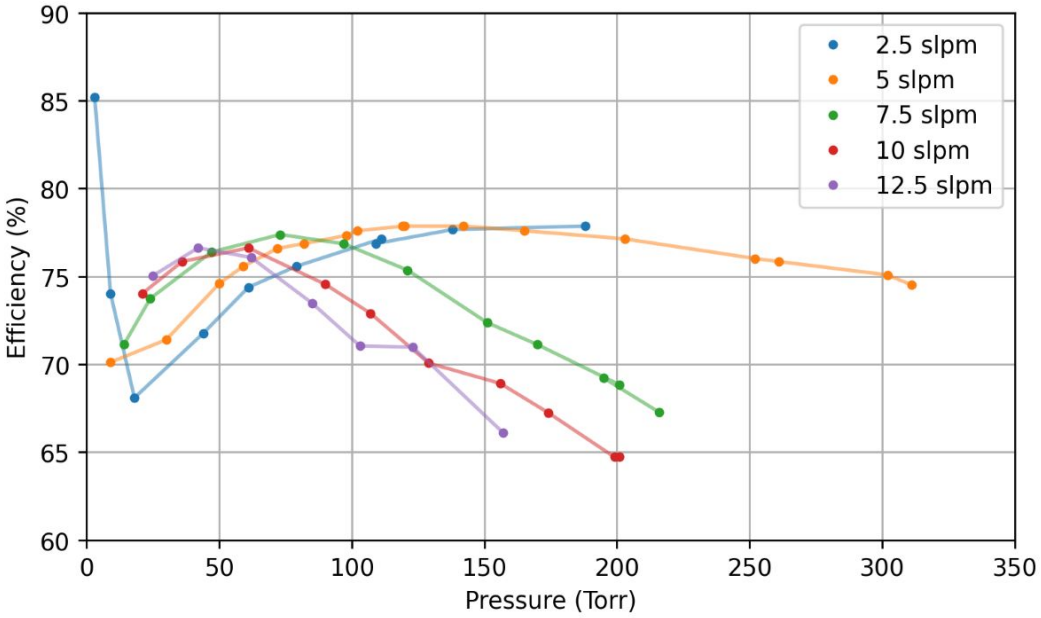

Figure 4.3: Measured RF efficiency against pressure in the source region.

source for all examined flow rates at 950 W applied power.

Both pressure and flow rate have significant impacts on RF efficiency. Across all flow rates, peak efficiency falls between ∼76% and ∼78%. Low flow rates see marginally higher maximum efficiency than high flow rates. The pressure at which this peak efficiency is achieved trends lower with increasing flow rate.

The 2.5 slpm case exhibits notably different behaviour at low pressures compared to its trend at higher pressures or the other flow rates. Interesting behaviour was observed in the source at this low flow rate and pressure, in which no visible plume was ejected downstream and light emission from the source was far brighter than in any other examined condition. As pressure was increased the brightness of the source notably dimmed, while downstream emission increased significantly and a visible plume formed. Reflected power increased significantly with increasing pressure and necessitated greater input into the matching network than similar pressure increases in other examined flow rates. This change is reflected in the RF efficiency of the discharge, dropping significantly from ∼85% to a minimum of ∼68% over less than 15 Torr. By ∼18 Torr the 2.5 slpm discharge appears to join the general trend of the other flow rates, once again trending upward with increasing pressure.

Of note is the emergence of two groups of lines. The 2.5 and 5 slpm cases see efficiency increase relatively slowly with respect to pressure below ∼100 Torr, and the 5 slpm case then trends slowly downward beyond ∼150 Torr while the 2.5 slpm case plateaus. Comparatively, while the 7.5 slpm case starts at a similar efficiency

and pressure as the 5 slpm case, it increases much more rapidly with pressure. By ∼30 Torr it joins the 10 and 12.5 slpm cases, and is ∼5% more efficient than the 5 slpm case at the same pressure. By 100 Torr, however, the 7.5 to 12.5 slpm lines have all peaked and are seeing efficiency decrease with pressure, while the 2.5 and 5 slpm efficiencies are still increasing. While the 5 slpm case has a slow decline in efficiency at higher pressures, 7.5 slpm and above see a sharper drop off after their peak efficiencies. The gradient of this decline appears to be correlated to the flow rate, with 7.5 slpm seeing a 10% decline in efficiency over ∼150 Torr, 10 slpm declining by the same amount in only ∼120 Torr, and 12.5 slpm needing only ∼95 Torr.

Interestingly all three of the high flow rates see similar efficiencies for pressures below 50 Torr, unlike the low flow rates which follow similar shapes but with a significant difference in value. This may be indicative of a saturation effect at low pressures, where higher flow rates produce better RF coupling up to a limit around 7.5 slpm, beyond which further increases have only small impacts on efficiency. As pressure increases, however, this saturation effect breaks down and efficiencies diverge strongly based on flow rate.

To determine the cause of this significant variation in power transfer efficiency, several key plasma parameters were calculated: the electron density, ionisation ratio and plasma skin depth.

4.2.3 Electron Density

Like the power transfer efficiency, electron density values were found to be strongly influenced by both the flow rate and pressure of a discharge. These results are presented in Figure 4.4. The overall shape followed by each discharge curve as pressure increases diverges between low (2.5, 5 slpm) and high (7.5, 10, 12.5 slpm) flow rate cases. All follow an initial near-linear rise at low pressures which gives way to either a decay in gradient for the former or a transition into a plateau for the latter.

Among the low flow rates, the 5 slpm discharge sees greater electron density increase with pressure compared to 2.5 slpm, though the difference between the two curves peaks around 140 Torr. At higher pressures, the electron density increase of the 2.5 slpm case outpaces the 5 slpm case, closing this gap.

Among the high flow rates, the pressure at which the transition to a plateau occurs decreases as flow rate increases. This results in significantly lower peak electron densities being achieved in higher flow rates, allowing the 5 slpm case to reach an electron

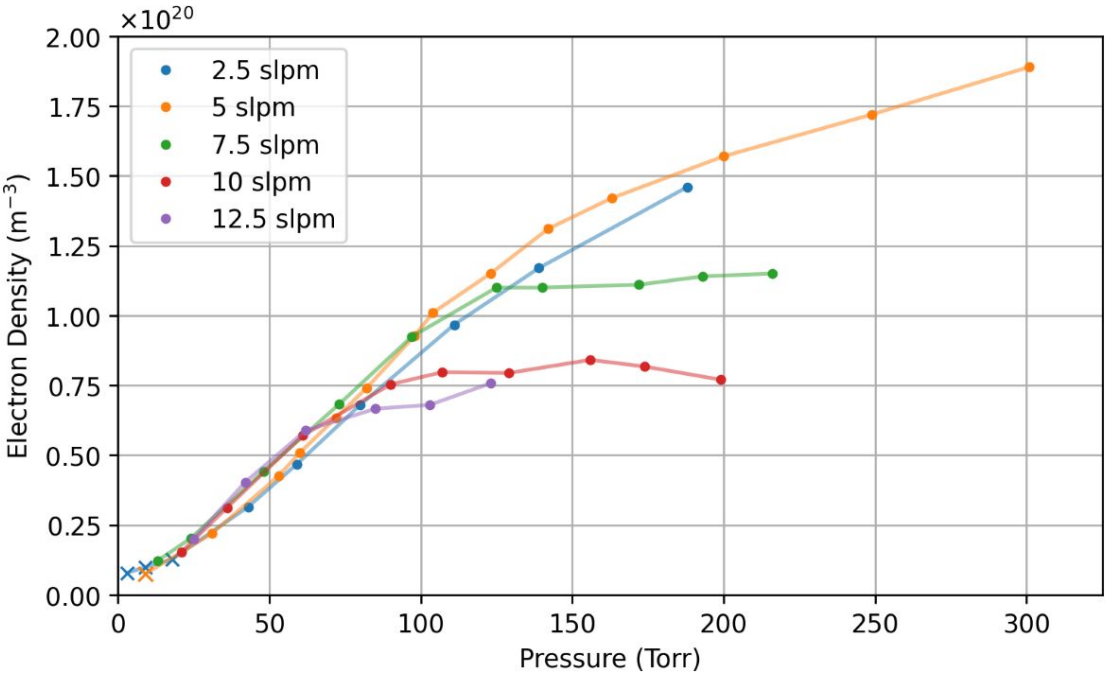

Figure 4.4: Electron density, calculated using measured plasma resistance and modelled electron temperatures, plotted against pressure in the source. Circles indicate values calculated using measured gas temperatures, crosses indicate values calculated assuming a gas temperature equal to that of the lowest pressure conditions for which a gas temperature could be measured for a discharge of the same flow rate.

density approximately 50% higher than the 12.5 slpm discharge at the same pressure of ∼120 Torr. Such differences yield an apparent correlation between electron density and maximum stable operating pressure, with discharges extinguishing in order from lowest peak electron density to highest (note that the 2.5 slpm discharge was not investigated beyond 188 Torr due to insufficient plume expulsion rather than plasma extinction). This suggests the extinction of high flow rate discharges at pressures that can sustain low flow rate discharges may arise from insufficient electron density in the source.

Interestingly, these electron density results align reasonably well with those determined using the same plasma impedance method reported by Pascale et. al. in [11]. This is despite Pascale's device operating in argon and using a supersonic nozzle. Discharges in both devices exhibit a rise with pressure that transitions into a plateau, with maximum electron densities reaching $\sim 2 \times 10^{20}$ m^{-3}. Of note is that in Pascale's work, the plateau occurs at lower electron densities for device configurations with wider nozzle diameters, which correspond to higher flow rates for a given pressure. This aligns with the trends observed in this work. As both devices employ reverse

vortex gas injection and use the same source region dimensions, this similarity in electron density results may be attributable to common gas flow dynamics.

Of particular note is that both devices achieve approximately equal electron densities despite operating using different gases. As discussed in Chapter 1, the higher electron scattering cross section of nitrogen compared to argon results in greater electron energy losses to neutral particles. Thus for a given operating power, an argon plasma should achieve higher electron densities than a nitrogen plasma. Pascale's results were captured in discharges with applied powers of 800 W, while the results presented here used 950 W. However, the power transfer efficiency of the nitrogen plasma was lower than that reported for Pascale's argon plasma. Accounting for this, slightly more power was coupled into the argon plasma than any of the nitrogen discharges studied in this work. The unexpected similarity in electron density therefore cannot be attributed to differences in power delivered to the plasma.

Electron Flux Balance

Such insensitivity to feed gas and weak correlation to coupled power may indicate that the balance between electron production and loss mechanisms in both devices is dominated not by available power, but by some other factor. Given that the value of electron density at which a plateau is observed varies with flow rate or nozzle diameter, gas flow dynamics likely plays a significant role in electron loss rates. A natural candidate for this contribution is the flow of plasma into the plume. As previously discussed, ion motion is influenced by the bulk gas flow and thus subject to being blown out of the plasma forming region. In order to maintain quasi-neutrality, any increase in ion loss rates due to expulsion necessarily produces a matching increase in electron loss rates. Due to the electric charges involved, this most likely results in electrons also being expelled downstream, driven by ambipolar diffusion. The rate of this electron expulsion varying with flow rate would result in variation in electron density, which may account for the trends observed.

The low pressure ratio results presented in Section 3.1.1 indicate that the velocity of gas flowing out of the source region is relatively constant across flow rates at low pressures, with the differences in flow rate instead accommodated by changes in the average density of gas in the throat. The source region gas density is approximately consistent across all flow rates for all pressures, meaning the gas momentum flow, given by $n_g A_t v^2$, is also similar across flow rates. This suggests ions in the plasma forming region would experience a similar force in the direction of the throat regardless of flow rate, leading to similar loss rates and thus electron densities. As pressure increases, the density of freshly injected gas increases, causing it to take up

a smaller volume at the throat and thus reducing the share of gas immediately lost downstream in higher flow rates. The resulting decrease in average gas density in the throat must be offset by higher gas speeds, which leads to an increased gas momentum flow compared to lower flow rates. This would result in stronger ion expulsion rates for higher flow rate discharges, leading to a lower electron density.

While this explanation accounts for a difference in electron density between flow rates emerging as pressure increases, it does not directly account for the plateauing observed. To address this, we consider a highly simplified particle balance equation for electrons, accounting for electron production through ionisation and loss through volumetric flows out of the plasma region, Γ:

$$\frac{dn_e}{dt} = n_e n_g K_{iz}(T_e) - \Gamma \tag{4.11}$$

In steady state conditions $\frac{dn_e}{dt} = 0$, giving:

$$n_e = \frac{\Gamma}{n_g K_{iz}(T_e)} \tag{4.12}$$

Note that Γ is itself a function of n_e, meaning increased electron loss does not produce an increased electron density. The ionisation rate factor is a function of electron temperature, which is itself a function of neutral gas density. This allows the ionisation rate to be expressed as a function of neutral gas density, which is plotted for all data points in Figure 4.5.

Using the relationship determined in the figure, $K_{iz}(T_e) \propto n_g^{-2}$, this leaves:

$$n_e \propto n_g \Gamma \tag{4.13}$$

We can thus conclude that in order for electron density to plateau with respect to neutral gas density $\Gamma \propto n_g^{-1}$. This aligns with an electron flux function dominated by the previously discussed incompressible flow velocity or gas flow momentum, both of which exhibit inverse proportionality to neutral gas density.

Wall-dominated loss fluxes are correlated to neutral gas density through the edge-to-centre plasma density ratios, introduced in Section 1.2. These ratios are functions of neutral gas density and electron temperature, itself a function of gas density. As a result, when evaluated for examined conditions, these functions are best fit by curves proportional to n_g^{-a} for a between 1.15 and 1.25. Thus wall-dominated loss fluxes do no cancel out the neutral gas density component of Equation 4.13.

Considering this conclusion in light of the results of Figure 4.4 implies that the 2.5

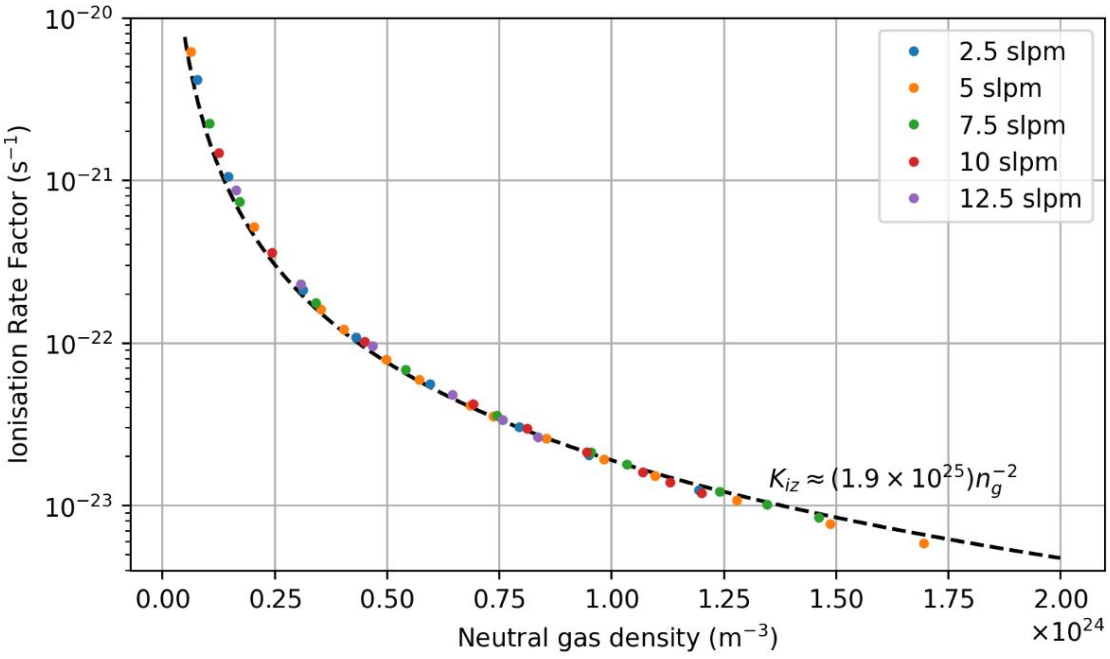

Figure 4.5: Ionisation rate factor calculated using electron temperatures determined by the global model from measured pressures and temperatures, plotted against neutral gas density for all data points. The dashed line shows the data can be approximately fit to the inverse square of neutral gas density.

slpm and 5 slpm cases do not exhibit an electron density plateau due to diffusion to the wall dominating the charged particle losses of such discharges for all examined pressures. The higher flow rates, meanwhile, appear to transition from wall-dominated losses at low pressures to exhaust-dominated losses at higher pressures. This initial wall-dominated loss regime gives rise to the similar electron densities present across all flow rates below 50-100 Torr, with divergence occurring only once both the gas density and flow velocity are high enough for losses to the plume to outnumber losses to the walls.

This conclusion is complicated by the electron temperature calculation process considering losses only to the walls. As increased losses yield higher electron temperatures for a given gas density, electron temperature and density are likely underestimated for all flow rates, with the higher flow rates seeing the largest errors. The scale of this error is likely relatively small, however, as the electron temperatures of the discharge are low compared to the ionisation and excitation energies of nitrogen. A five-fold increase in the modelled loss flux yields electron temperatures only ∼10% higher, and electron densities ∼5% higher. It is therefore unlikely that the observed plateaus are an artefact of underestimated electron temperatures.

Correlation with Gas Heating

The possibility that discharges experience significant charged particle losses to the plume was identified in the previous chapter due to the observation of gas heating between the source region and plume that could not be attributed to energy lost from the vibrational mode. This heating was observed for the 7.5, 10 and 12.5 slpm flow rates in varying pressure ranges above ∼60 Torr. Figure 4.6 plots source and plume gas temperatures and electron densities against pressure for these three flow rates to assess correlation between observed electron density plateaus and temperature inversions.

A clear alignment is evident between the pressures where electron densities of the examined flow rates first fall relative to those of the 5 slpm case, and the pressures where plume temperatures first exceed source temperatures. This provides further evidence that recombination of charged particles lost to the plume produces much of the excess gas heating observed in the previous chapter. Additionally, it indicates that the electron density plateaus observed for the same flow rates may arise due to this same loss. This follows from considering an approximated energy balance equation: the power transfer efficiencies, and thus total powers absorbed in the plasma, are generally similar for all flow rates at all pressures, and thus approximately equal rates of ionisation are seen across all flow rates for a given pressure. For two flow rates at the same pressure to exhibit different electron densities, one must lose a larger fraction of the charged particles present in the source than the other. Those which lose a larger fraction of charged particles present in the source necessarily have lower electron densities. Therefore, the 7.5, 10 and 12.5 slpm flow rates all experience greater electron losses than the 2.5 and 5 slpm flow rates, which experience similar losses. As the 12.5 slpm case plateaus at the lowest electron densities, it experiences the most significant losses to the plume, followed by the 10 and 7.5 slpm cases, respectively.

Interestingly, Figure 4.6 also shows that the pressures where electron density plateaus begin largely align with those for which the direction of the source temperature trend changes from negative to positive. This suggests charged particle losses to the plume may play a role in increasing source temperatures, however, as the 2.5 and 5 slpm cases both also exhibit such increases in source temperatures, it is likely not correlated strictly to density plateaus, but rather the presence of charged particle losses at all. This is further examined in Section 4.3.

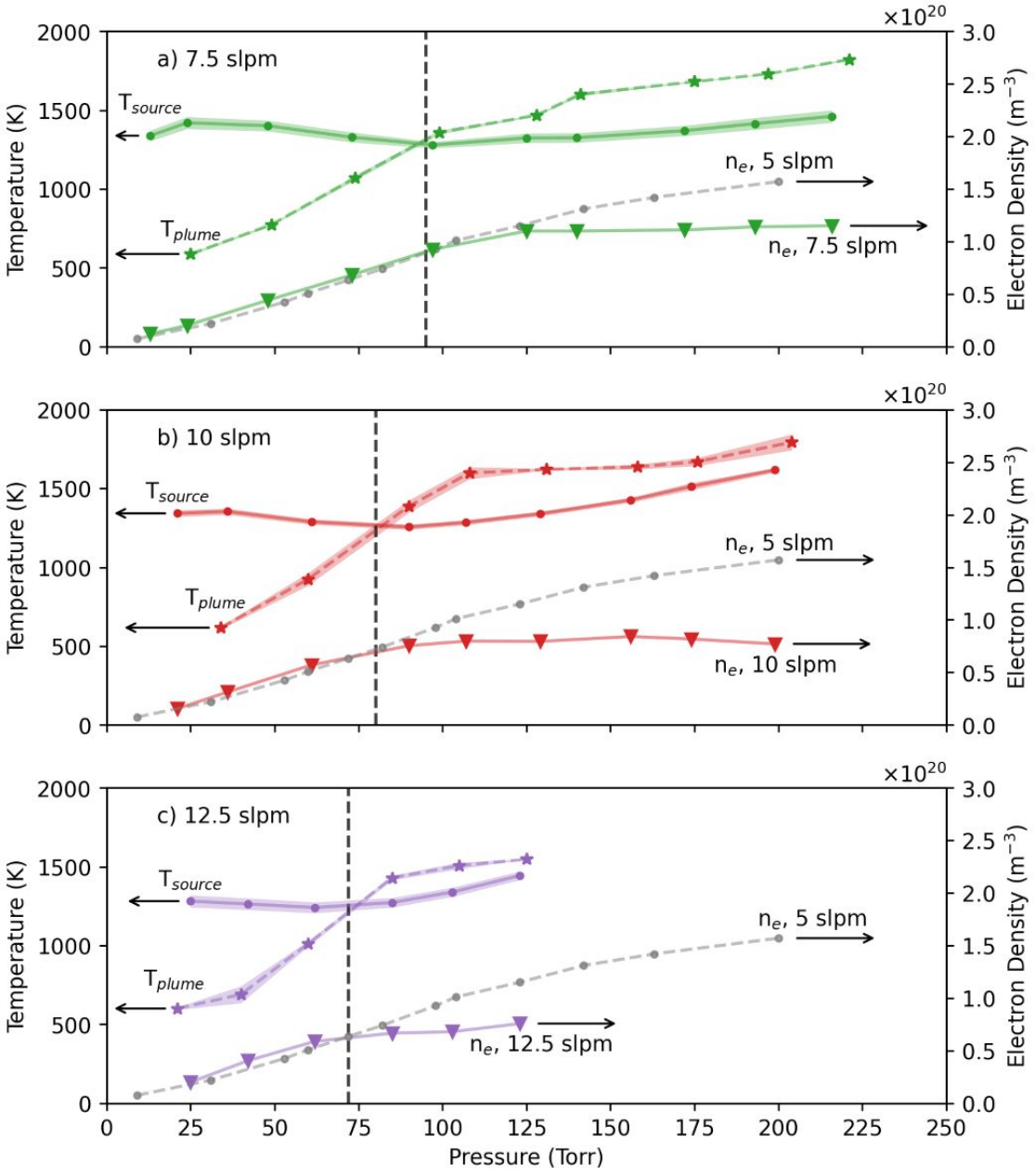

Figure 4.6: Plots of gas temperatures (left axis) and electron densities (right axis) against pressure for discharges with flow rates of a) 7.5 slpm, b) 10 slpm, and c) 12.5 slpm. Electron densities for the 5 slpm case are included on all plots (grey markers with dashed line) as an non-plateauing baseline for electron density. The dashed black line on each plot indicates the approximate pressure where the electron density trend diverges from the 5 slpm case, marking the start of the plateau.

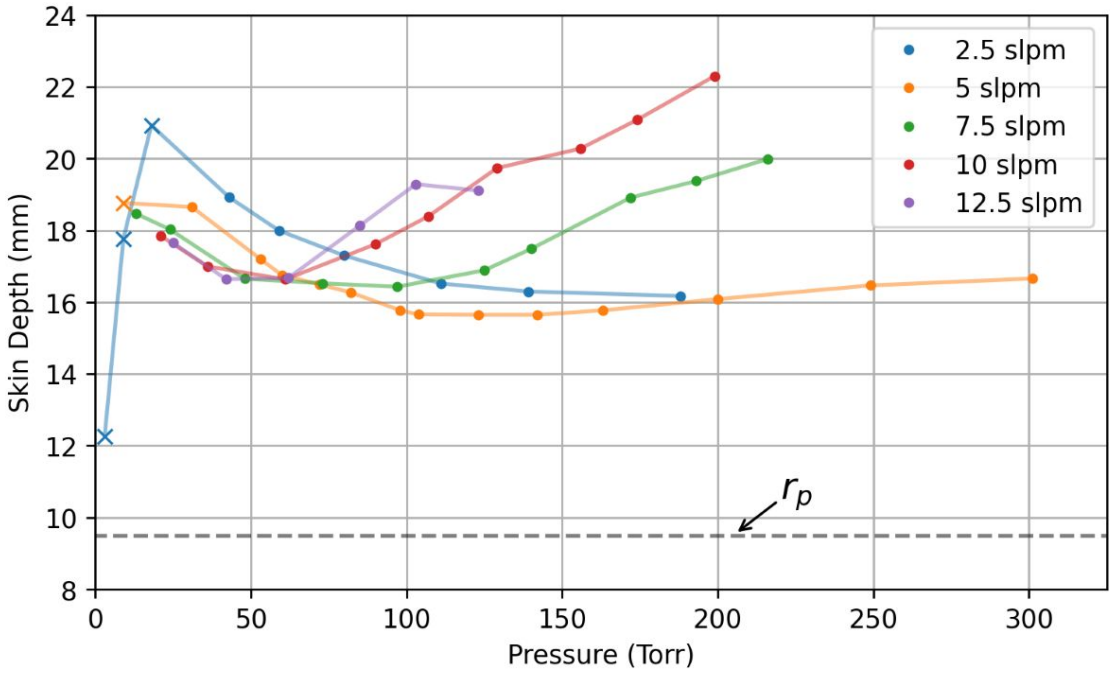

Figure 4.7: Skin depth, determined using calculated electron density values, against pressure. Circles indicate values calculated using measured gas temperatures, crosses indicate values calculated assuming a gas temperature equal to that of the lowest pressure conditions for which a gas temperature could be measured for a discharge of the same flow rate.

4.2.4 Skin Depth

In Ref. [11] Pascale *et al.* suggests that the electron density plateaus observed using plasma impedance measurements may be accounted for by electromagnetic shielding of the plasma bulk. As electron density increases, the skin depth decreases, resulting in the region of plasma 'visible' to the electromagnetic field of the coil being limited to an annulus of decreasing depth. Due to previously discussed edge-to-centre ratios for confined inductively coupled plasma, the electron density decreases with distance from the device axis, resulting in any increase in average density within the skin depth to be offset by the region included within it shrinking to exclude more of the innermost plasma regions. This hypothesis was supported by the skin depth calculated using peak electron density measurements being in the range of 25% to 50% of the radius of the plasma region. Such skin depths are likely underestimates, as the average electron density of the discharge will be lower than the peak electron density. Nonetheless, the assumption that the skin depth is smaller than the plasma radius was likely correct.

Skin depths were calculated for the nitrogen discharges studied in this work, accord-

ing to the process described in Section 4.1. The results are presented in Figure 4.7. For all examined flow rates and pressures, the skin depth was found to be larger than the plasma radius, r_p. This indicates that the device axis is likely not electromagnetically shielded from the coil fields, meaning that the entire plasma contributes to the measured impedance. This is strong evidence that the electron density plateaus are not an artefact of electromagnetic shielding in the plasma, and instead a result of gas flow dynamics.

At low pressures the 7.5, 10 and 12.5 slpm flow rates exhibit very similar skin depths, smaller than those of lower flow rates at the same pressures. These pressures align with those where higher flow rates exhibit higher power transfer efficiency and slightly higher electron densities than lower flow rates. They also align with the pressures where high flow rates likely see a significant share of the incoming gas flow directly downstream without passing under the coil.

The influence of this latter factor may be responsible for the comparatively better performance of high flow rate discharges. It may result in them seeing lower effective mass flow rates passing through the plasma forming region compared to low flow rates. Such discharges would see more energy available per molecule, leading to higher electron densities. Alternatively, a layer of gas flowing across the throat may produce insulating effects that reduces energy loss out of the plasma, leaving more energy in the plasma for ionisation collisions. Regardless of the exact mechanism, these flow rates exhibit slightly higher electron density at low pressures, which results in a smaller skin depth. This, in turn, leads to a higher RF efficiency, as decreases in skin depth above the optimal value of $\sim 0.57 r_p$ means more energy is coupled out of the coil fields, improving efficiency [121].

Trends in power transfer efficiency can be similarly linked to electron density trends by way of the skin depth. High flow rate discharges at higher pressures experience an electron density plateau while neutral gas density continues to increase. Equation 4.10 shows that an increase in neutral density unmatched by an increase in electron density of equal magnitude results in a larger skin depth. When starting from a skin depth larger than $\sim 0.57 r_p$, this reduces power transfer efficiency.

Due to being present only at lowest pressures examined, the electron density behaviour correlated to the remarkably low skin depth and high RF efficiency exhibited by the 2.5 slpm case is not clearly visible. Figure 4.8 presents the ratio between electron and neutral gas density, the ionisation ratio, for all flow rates. It shows that the short skin depths correspond to unusually high electron densities which fall rapidly with increasing pressure to a trend significantly lower than that of higher flow rates. The weak correlation between electron temperature and density discussed

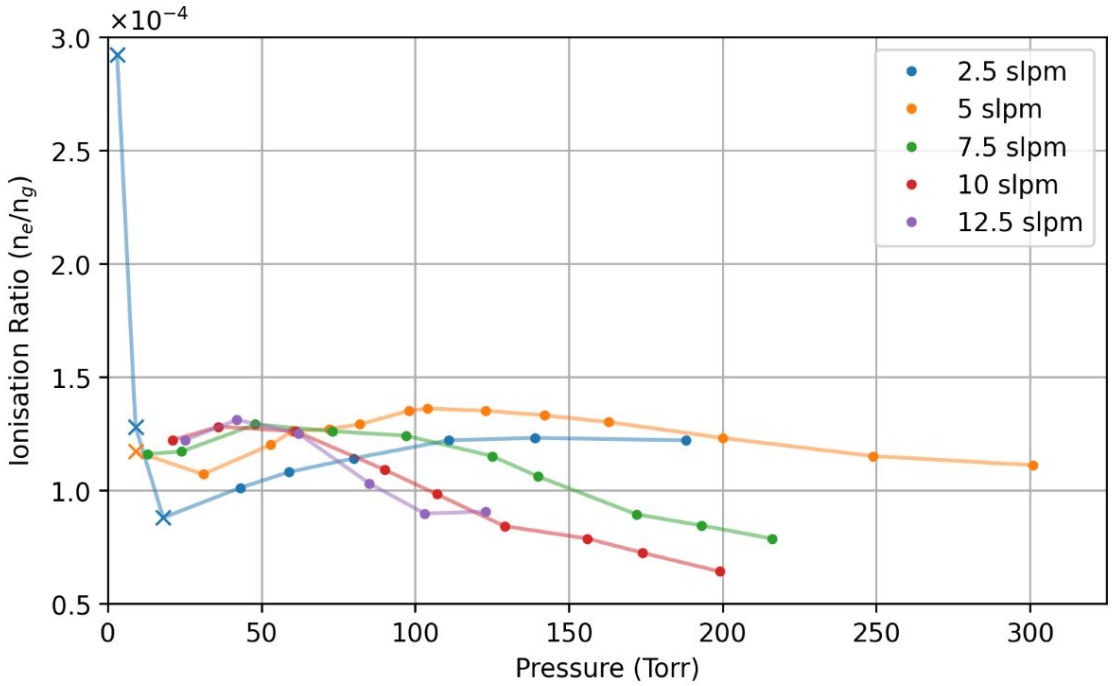

Figure 4.8: Ionisation ratio, determined using calculated electron density values, against pressure. Circles indicate values calculated using measured gas temperatures, crosses indicate values calculated assuming a gas temperature equal to that of the lowest pressure conditions for which a gas temperature could be measured for a discharge of the same flow rate.

in Section 4.2.3 rules out the high density being a result of the higher electron temperature predicted for such a discharge. Instead, its strong sensitivity to both flow rate and pressure points once again to flow dynamics as the underlying cause. The low collision rates and high residence times afforded by the low pressure and flow rate respectively may result in the gas spiralling upward through the device coupling strongly to the coil, as opposed to the preheated, downward-spiralling gas nearer the device axis. Such a discharge would behave more similarly to forward-vortex stabilised plasmas, which exhibit significant recirculation of plasma under the coil. Such a flow regime would likely have higher electron densities, but would see greater heat losses due to high temperature plasma contacting the walls. The enhanced power losses to the walls found for the 2.5 slpm case in Section 3.5.1 of Chapter 3 potentially align with this behaviour.

4.3 Plasma Oscillation

Oscillations in plasma resistance and optical emission intensity with periods on the order of tens of milliseconds were observed in discharges generated using a variety of flow rates and across a wide range of operating conditions. Both plasma resistance and optical emission intensity are correlated to the densities of electrons and neutral gas. Skin depth is sensitive to the ratio between these densities, meaning variation in one without equal relative change in the other produces fluctuations in RF efficiency and plasma resistance as discussed in Section 4.2.4. Optical emission intensity is sensitive to the electron-neutral collision rate, as the frequency with which molecules are excited into metastable states that emit light upon decaying determines the radiative power loss of a plasma. The collision frequency is linearly proportional to both electron and neutral density, suggesting absolute variation of either parameter will impact emission intensity. To gain greater insight into the underlying cause of this behaviour, measurements of these oscillations across varying power, flow rates and pressures were collected.

Figure 4.9 shows an example of measurements taken in an oscillating discharge. The signal from the current probe and the peak-to-peak measurement of this signal is shown in the top and middle plots, respectively. As the current probe signal oscillates on short timescales with the applied radio-frequency AC power, the larger time scale oscillation is apparent in the variation of the signal envelope, shown in orange. The output sampling rate applied by the oscilloscope when saving data is much lower than both the RF oscillation and sampling rate, decreasing the time resolution of the recorded measurements and resulting in noisy signal envelopes and peak-to-peak current probe measurements. Optical emissions from the plasma do not fluctuate significantly with the applied radio-frequency power, allowing photodiode measurements shown in the bottom plot to produce much clearer evidence of the oscillation.

Using the wave frequency and phase of the oscillation visible in the photodiode signal, contributions from an oscillation of the same frequency can be made out in the peak-to-peak measurement of the current probe. Peaks in the latter can be seen to align with troughs in the former. This phase difference aligns with oscillation in electron density. A drop in electron density causes the skin depth to expand, decreasing plasma resistance. This results in a higher current across the coil and thus a peak in the probe signal. Simultaneously, the electron-neutral collision rate would drop, causing optical output from the plasma to decline and produce a trough in the photodiode signal.

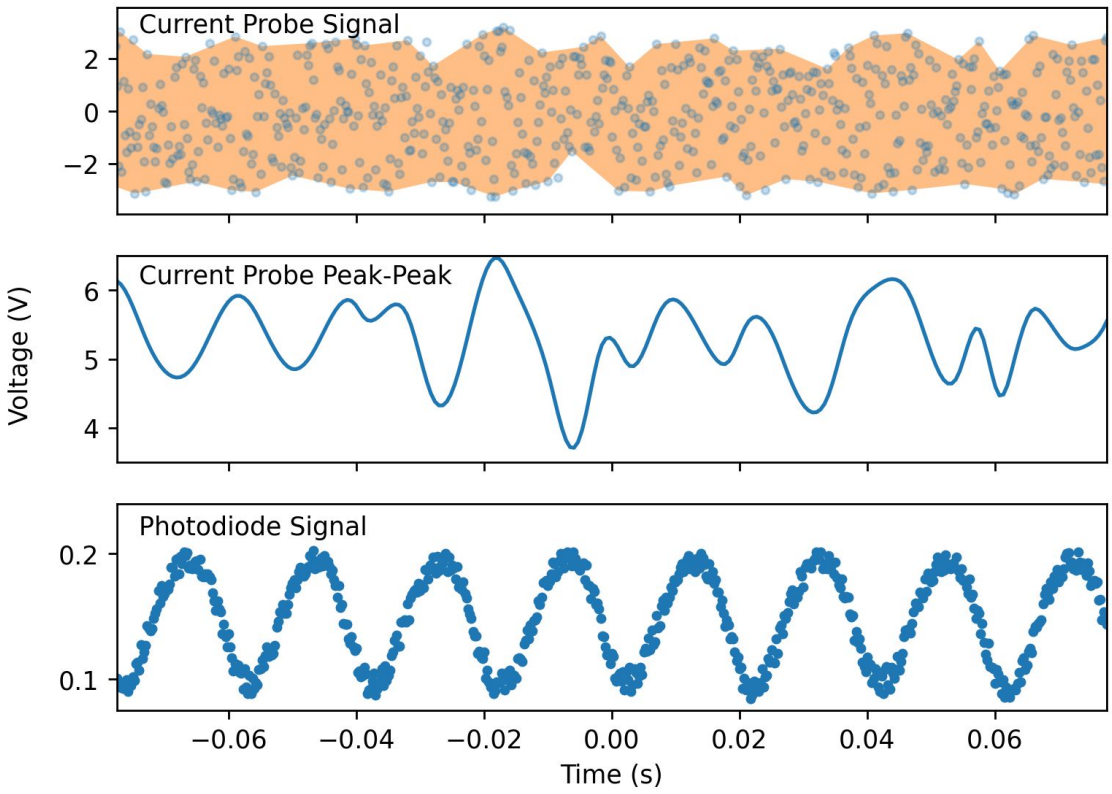

Figure 4.9: Time-resolved current probe (top) and photodiode (bottom) signals, produced by a 950 W, 5 slpm discharge at 400 Torr. Noise in the current probe signal is produced by the sampling rate of the oscilloscope data output, however evidence of a regular oscillation can be seen in the width of the peak-to-peak envelope (middle).

This behaviour is distinct from that which would be expected if the neutral gas density were instead the parameter fluctuating. In that case, when neutral density increases, so too would skin depth, decreasing the plasma resistance and thus producing a peak in coil current. As the electron-neutral collision rate is proportional to the gas density, it would also increase in this period, producing, among other effects, higher rates of metastable production. The short lifetime of most of these states would result an effectively immediate increase in the intensity of light emitted by the discharge at the timescales examined, leading to a peak in the photodiode signal. Thus, if the oscillation was caused by variation in the neutral gas density, the oscillations measured by the current probe would be in phase with those measured by the photodiode, rather than in quadrature, as observed. While not conclusive given their relatively low time resolutions, the likelihood of gas density oscillation is further reduced by a lack of time-varying fluctuations in either the pressure measurements or mass flow controller output.

Similar oscillation has been observed in Ref. [88] in argon discharges in the pre-

viously discussed supersonic ICP torch. In such a device fluctuations originating downstream cannot propagate across the supersonic nozzle into the plasma forming region. Given the similarity of the oscillations observed, it was determined that study of the plume emissions would not be necessary. Without the restriction of requiring detectable emissions in the plume, the device could be operated at pressures up to 1 atmosphere, allowing measurement of the instability over a greater pressure range than those used for temperature measurements.

Measurements presented in this section were captured prior to the addition of water-cooling in the coil. As part of this change, additional electrical insulation was added between the coil and the exterior source tube to minimise risk of arcing between them. Thus in the conditions presented below, the coil was closer to plasma forming region than in previously presented measurements, producing an RF efficiency between 5 and 10% higher across all discharge conditions. As a result, the discharges examined in this section likely experienced slightly higher electron densities than those previously reported, as well as potentially stronger electric fields from the coil. Additionally, without water cooling, the electrical behaviour of the coil is impacted by its thermal conditions, which are sensitive to the operating power and discharge duration.

4.3.1 Sensitivity to Flow Rate

The photo-diode measurements showed low-intensity and high frequency instabilities were present for a far greater range of pressures and flow rates than could be observed using only oscillation of the current probe envelope. Generally, for operation at 950 W, the instability is most strongly present at high pressures and flow rates, where it often appears to be a likely cause of plasma extinction. Measurements of 600 W discharges using the photo-diode show, however, that the instability is present at pressures as low as 20 Torr and with flow rates as low as 2 slpm, as shown in Figure 4.10.

The figure plots the frequency and amplitude of the oscillation against mass flow rate for a low power, low pressure discharge. The amplitude is normalised by dividing half the measured peak-to-peak value of the photodiode signal by the average value of the signal across several oscillation periods. This normalised value can be thought of as a measure of the severity of the oscillation, with higher values corresponding to larger variations in electron density.

Both the frequency and the amplitude of the oscillation are shown to be sensitive to the flow rate of the discharge. Both parameters see an initial increase with flow rate between 2 and $\sim$3.5 slpm, before a peak around 4 slpm and strong declines

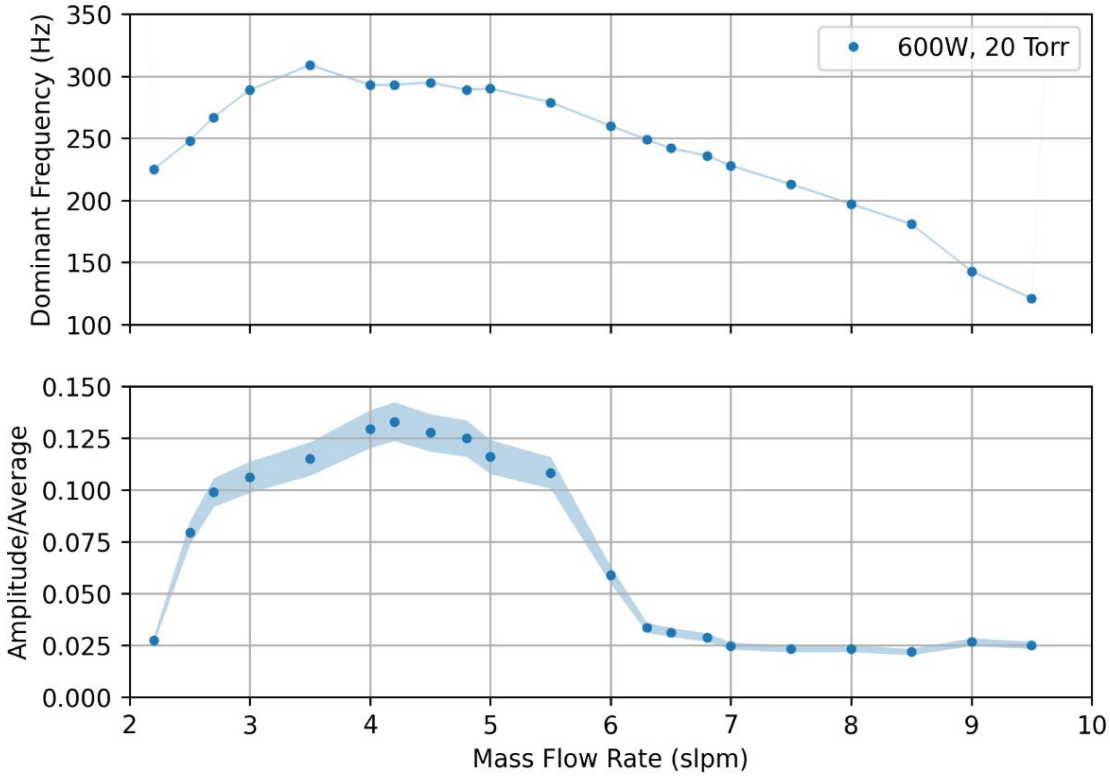

Figure 4.10: Dominant frequency of the oscillation (top), and ratio between the amplitude of the emission intensity oscillation and the time-averaged output (bottom), against flow rate for a 600 W discharge at 20 Torr.

from 5 slpm. While the frequency declines relatively smoothly for high flow rates, a comparatively sharp change in normalised amplitude is present between 5.5 and 6.3 slpm, beyond which it remains low and relatively steady. This behaviour suggests that the frequency and amplitude of the oscillation are not strongly correlated. The relatively steady trend exhibited by frequency suggests it is correlated to a parameter that itself changes steadily with flow rate, which at these low pressures includes gas temperature (see Chapter 3). The sudden changes exhibited by normalised amplitude are suggestive of a resonance effect, caused by alignment between plasma or flow parameters with a factor such as device geometry.

4.3.2 Sensitivity to Pressure

Figure 4.11 presents the frequency and normalised amplitude of a 600 W discharge produced with a constant flow rate of 10 slpm and under varying pressures. Interestingly the values measured at ∼20 Torr differ from those observed in the variable flow rate run for high flow rates, both being close to double the values presented for

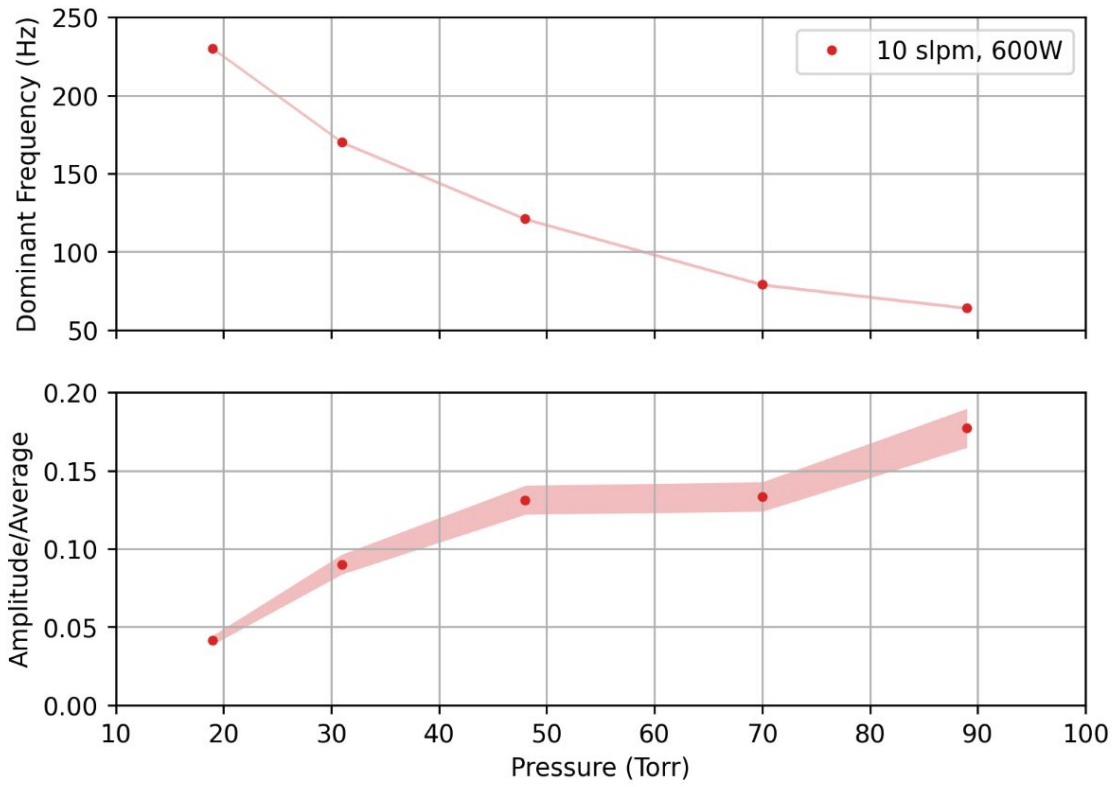

Figure 4.11: Dominant frequency of the oscillation (top), and ratio between the amplitude of the emission intensity oscillation and the time-averaged output (bottom), against pressure for a 600 W discharge with a flow rate of 10 slpm.

the 9.5 slpm discharge in Figure 4.10. This may be due to the temperature of coil, as the 9.5 slpm measurement in the varying flow rate run was taken after the discharge had been running for approximately an hour, while the ∼20 Torr measurement of the constant 10 slpm run was captured shortly after the plasma was ignited. As the discharge runs and coil temperature increases, so too does the resistance of the coil wire, lowering the total power available for dissipation within the plasma and thus possibly lowering the electron density of the plasma produced. This difference in electron density may then give rise to a different oscillation response.

Figure 4.11 shows that increasing pressure results in decreasing oscillation frequency and increasing normalised oscillation amplitude. As pressure is strongly correlated to neutral gas density, this increasing severity may be a function of density. As density and pressure increase, gas flow velocity is expected to decrease, while under idealised flow regimes the gas flow velocity should increase with flow rate. Applying these assumptions, the oscillation amplitude being sensitive to a particular range of gas velocities may be able to account for the amplitude trends of Figures 4.10 and 4.11, with increasing pressure and density slowing the flow velocity of the 10 slpm

discharge until it falls within the range exhibited by lower flow rates at 20 Torr. However such an explanation does not account for the evidence of non-ideal gas flow regimes found for higher flow rate discharges at low pressures, which result in roughly similar flow velocities within the source compared to other flow rates.

Considering the possible influence of the gas flows identified in Section 3.1.1 indicates that oscillation amplitude may be related to charged particle losses due to plasma expulsion. Previous findings suggest that at low pressures, high flow rates likely lose a large share of gas immediately down the throat. This may result in flow rate through the plasma forming region being lower for higher flow rates, resulting in lower flow velocities. As pressure increases, a greater portion of the gas enters the reverse vortex flow, resulting in flow velocities closer to the ideal flow case (*i.e.,* higher than those of low flow rates). Thus, as pressure increases, all flow rates experience a similar increase in density while velocity decreases less for high flow rates than low. The overall result is that at low pressures, low flow rates experience greater momentum flow and thus greater rates of plasma expulsion, while at higher pressures high flow rates experience stronger plasma expulsion. If oscillation amplitude is correlated with charged particle loss via expulsion, this could explain why oscillation amplitude is significant only for low flow rates in Figure 4.10, while also steadily increasing with pressure for a higher flow rate in Figure 4.11.

Figure 4.12 examines the pressure-sensitivity of the oscillation for a discharge operated at a higher power. The pressure range in which a 950 W discharge could operate was significantly larger than the 600 W discharges examined previously, with both flow rates examined in this case capable of operation up to approximately atmospheric pressure.

The rate at which instability frequency declines with respect to pressure is significantly lower than in 600 W discharges, and varies with flow rate more at low pressures than at high pressures. Interestingly the 7 slpm discharge sees higher instability frequencies than the 5 slpm discharge for all pressures, suggesting that, under these conditions, the upward sloping portion of the frequency-flow rate plot measured in 4.10 extends to much higher flow rates. This upward sloping region may be correlated to gas flow velocity, as without significant gas loss upon injection, higher flow rates necessitate higher flow velocities and thus reduced residence times. Such changes would result in a higher refilling rate within the source, potentially increasing the frequency with which a cycle can occur. Alternatively, small differences in neutral gas density due to temperature variation between flow rates would produce higher collision rates, potentially allowing cooler plasmas to build up electrons more quickly after a dip in electron density, resulting in higher oscillation

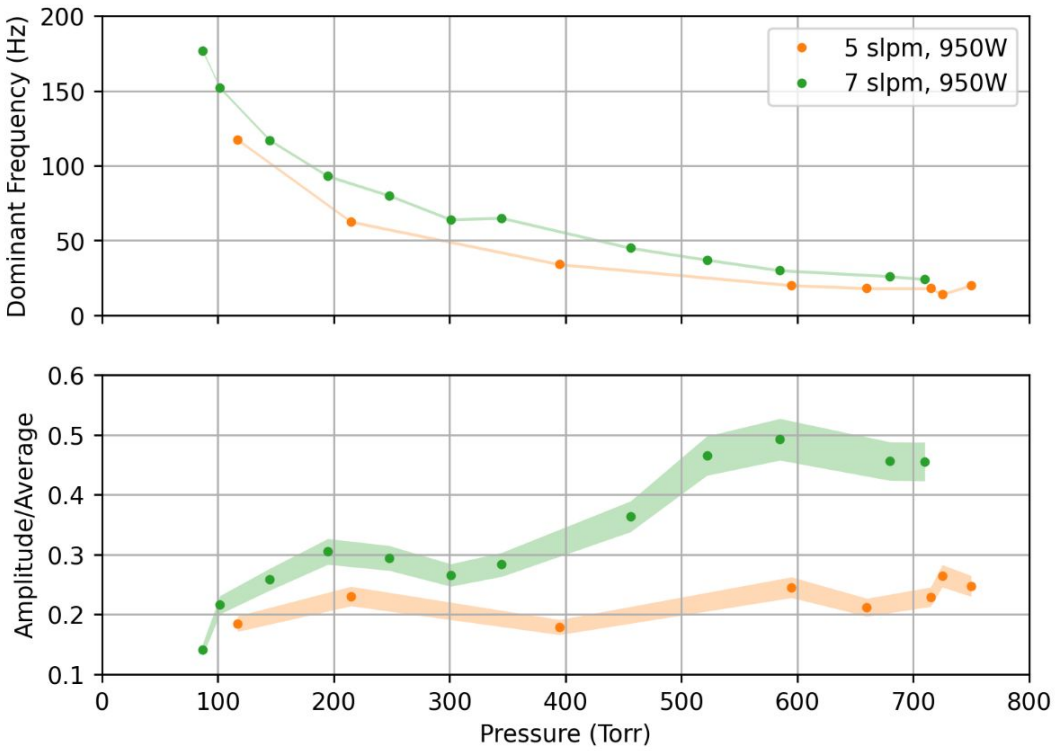

Figure 4.12: Dominant frequency of the oscillation (top), and ratio between the amplitude of the emission intensity oscillation and the time-averaged output (bottom), against pressure for 950 W discharges of differing flow rates.

frequencies.

The oscillation amplitude diverges significantly between the two flow rates examined, after starting from values generally consistent with the highest pressure measurements of Figure 4.11. Just as for the frequency measurements, the normalised amplitude of the 7 slpm discharge is higher than that of the 5 slpm discharge for all pressures examined. This difference holds relatively stable between 100 and 300 Torr before diverging significantly between 300 and 500 Torr. At the highest examined pressures this difference appears to plateau, with the 5 slpm case seeing normalised amplitudes of approximately 0.25, while the 7 slpm case has reached amplitudes around 0.5. The significantly stronger oscillation amplitude of the higher flow rate case aligns with the lower maximum operating pressure and decreased electrical stability exhibited by higher flow rates in previous results, indicating that as pressure increases so too does the severity of the oscillation up to a critical point where the discharge cannot be sustained.

This divergence between flow rates also supports the hypothesis that oscillation amplitude correlates to charged particle loss to the plume. In this pressure range, measured pressure ratios are better aligned with those calculated from idealised

flows, meaning flow velocity increases with flow rate. Charged particles in higher flow rate discharges thus experience stronger inertial forces pushing them downstream, leading to higher loss fluxes and stronger oscillation.

4.3.3 Possible Production Mechanism

A stable oscillation in electron density over time suggests that a steady-state solution to the simplified electron particle balance (Equation 4.11) does not exist. As the experimentally observed solution is sinusoidal, the particle balance must be a second-order differential equation. Such an equation would require a term proportional to the second time derivative of electron temperature. This term may arise from sensitivity of electron loss flux to interaction between the fields generated by the plasma and the coil. Electrons are accelerated azimuthally around the axis by an electro-motive force ($\mathcal{E}$) determined by Faraday's law:

$$\mathcal{E} = -\frac{d\mathbf{B}_z A}{dt} \tag{4.14}$$

where $\mathbf{B}_z$ is the axial magnetic field and A the cross-sectional area of the discharge. Through Ampere's law:

$$\mathbf{B}_z = \mu_0(\mathbf{J}_\phi + \varepsilon_0 \frac{d\mathbf{E}_\phi}{dt})r \tag{4.15}$$

where $\mathbf{J}_\phi$ and $\mathbf{E}_\phi$ are azimuthal current density and electric field, respectively. The current density accounts for currents in both the coil and the plasma, the latter of which is proportional to $n_e v_\phi$. The electric field in the plasma is proportional to n_e through plasma polarisability ε_p, thereby providing the required second derivative of electron density.

Therefore, the observed oscillation may be the result of the electron particle balance equation requiring a term dependent on the azimuthal electron velocity, which is governed by the electro-motive force produced by induction. Such a term can be interpreted physically by linking azimuthal electron velocity to a resulting centripetal force toward the device walls.

In discharges where plasma flow out of the source dominates charged particle losses, the electric field experienced by an electron in the plasma bulk is stronger than that experienced in a discharge with low charged particle losses, due to the lower electron density present screening out less of the coil field. The electron therefore experiences strong azimuthal acceleration, resulting in a centripetal force pushing it toward the wall and encouraging recirculation. A high recirculation rate reduces the electron loss flux, leading to an increased electron density. This results in more

significant shielding of the electric fields of the coil, causing electrons to experience weaker azimuthal acceleration and this weaker centripetal forces toward the wall. This results in a smaller portion of electrons in the bulk flow reaching the wall and experiencing recirculation, increasing electron losses to the plume, lowering electron density and finishing the oscillation cycle.

Such fluctuations in electron density under the coil would result in power transfer efficiency fluctuations. This would produce periods in the cycle with high rates of electron-ion recombination. These periods would convert electronic energy into thermal energy in the source region, and are likely the origin of the increases gas temperatures with increasing pressure observed in Figures 3.6 and 4.6.

In discharges not dominated by plume losses, small changes in the electron particle balance produced by fluctuations in the recirculation rate likely have little impact on overall charged particle exhaustion rates, resulting in fluctuations of electron density with time being damped. This would account for the low pressures of discharges of all flow rates exhibiting no clear evidence of oscillation, while reporting similar electron densities, no evidence of electron-ion recombination in the plume, and source temperatures that decrease with pressure.

4.4 Summary

- An analytical model was developed based on that described in Ref. [12]. The model takes inputs of gas flow rate, operating pressure, resistance across the device, source region temperature, and chiller water temperature of a given plasma run and outputs electron temperature and density. From the latter, the plasma parameters of skin depth and ionisation rate could be determined.
- Results of the model showed electron densities varying significantly between flow rates, particularly at pressures above 100 Torr. Below 50 Torr, all examined flow rates saw electron density increase linearly with operating pressure, following similar gradients. Above 50 Torr, electron densities begin to plateau with respect to pressure, with plasmas diverging from this linear trend in reverse order of gas flow rate. As a result, the peak electron density modelled for the 10 and 12.5 slpm flow rates are less than half of those determined for the 2.5 and 5 slpm cases.
- The pressures at which such plateaus begin are shown to correlate with those at which measured gas temperatures in the plume overtake those found in the source. This may be indicative of charged particle expulsion rates increasing with gas flow rate for a given pressure, resulting in higher flow rate plasmas

seeing increased downstream heating at lower pressures due to higher electron-ion recombination rates in the plume.

- Measurements of an oscillation in plasma resistance and intensity of optical emission were presented. The amplitude of this oscillation was found to be sensitive to pressure and, at pressures above $\sim$ 100 Torr, strongly sensitive to increases in gas flow rate. A production mechanism is suggested that links the formation of this instability to increased charged particle losses from the source. This suggests that the lower stability of higher flow rate discharges at high pressures due to this oscillation is caused by the same underlying behaviour that also produces high plume temperatures and lower electron densities compared to lower flow rate discharges.

Chapter 5

Summary and Conclusions

The decarbonisation of many industrial processes requires the development of economically-viable, electrically-powered heat sources capable of reaching high temperatures (>800 C°). Plasma torches show potential for these applications, however economic viability currently limits their uptake. The plasma sources presently used most widely for process heat generation, arc discharge torches, experience significant electrode degradation and thus require frequent servicing and replacement of expensive plasma-facing components. Development of plasma torches with low servicing needs and therefore minimal operational downtime is necessary in order to be cost-competitive with fossil fuels. RF-ICP torches show promise in this regard, as they experience no contact between the electrode and plasma and thus do not require frequent servicing. Research evaluating them as sources of process heat has been limited, however, as the technology is primarily used in specialist industrial applications where electro-thermal efficiency is not a limiting constraint. Therefore, before the viability of using RF-ICP torches as process heat generators can be assessed, devices capable of operating under industrially-relevant pressures using low-cost feed gases need to be developed, and the plasma they produce experimentally characterised. In this thesis a 1kW RF-ICP torch was developed which generates plasma using nitrogen feed gas under pressures up to ∼0.5 atmosphere. Measurements of thermal and electrical properties of these plasma were performed, providing plasma parameters trends with respect to varying feed gas flow rates and operating pressures.

5.1 Summary

Plasma generated in the device was characterised using measurements of temperature, derived from captured emission spectra using optical emissions spectrometry (OES), and plasma resistance, derived from measurements of the coil current. All measurements were performed on discharges with supplied powers of 950 W, under

pressures between 3 and 300 Torr, and feed gas flow rates between 2.5 and 12.5 slpm.

The wavelength ranges studied were selected to capture the Second Positive and Fist Negative nitrogen emission systems. Fittings to these spectra therefore provided rotational and vibrational temperatures for neutral molecules in the third excited state, $N_2(C)$ and molecular ions in the second excited state, $N_2^+(B)$, respectively. For all but the lowest pressures examined, the collisionality of the plasma was found to be sufficient to ensure the $N_2(C)$ rotational temperature equilibrates with the overall gas temperature.

A simple analytical model was developed which takes experimentally-determined values of source region gas temperature and plasma resistance as inputs, alongside the independent variable of operating pressure. Using literature values for electron-neutral collision cross sections and time-invariant, volume-averaged particle balance equations presented in Ref. [12], it solves for the electron temperature and electron density present in the source region.

Thermal Characterisation

The neutral gas densities and collision frequencies were determined using measured pressure and $N_2(C)$ rotational temperature values in the source region and the plume. The collision frequencies for both regions were compared to the frequency corresponding to a collision interval one-quarter of the radiative lifetime of the $N_2(C)$ state. In discharge conditions exhibiting frequencies above this value, the gas temperature was taken as equal to the $N_2(C)$ rotational temperature. Conditions with frequencies below this value were excluded from gas temperature analysis.

Using the source region neutral gas densities, qualitative evidence of gas flow dynamics differing between flow rates was observed. Experimental measurements of the pressure difference across the choke were compared to those calculated assuming the density of gas passing through the throat matches that observed in the peak heating region of the source. All flow rates exhibit smaller pressure differences than predicted, indicating the density of expelled gas is higher than that observed in the source. As flow rate increases, so too does the difference between observed and predicted pressure ratios, indicating that higher flow rates see a greater share of injected gas flow immediately downstream rather than join the upwelling vortex to supply the plasma.

Neutral gas temperatures measured in the source region ranged from 1256 K for the 12.5 slpm discharge at 62 Torr, to 1766 K for the 5 slpm discharge at 301 Torr. Below 62 Torr, temperature was found to be generally inversely proportional

to flow rate. Above this pressure the 10 and 12.5 slpm discharges exhibit strong upward trends in temperature not present in the lower flow rates. These increases start at the same pressures as the previously observed electron density plateaus, indicating possible correlation with high rates of charged particles being expelled into the plume. It was determined that energy released in electron-ion recombination reactions due to strong electron density oscillation was the likely source of these increases in temperature.

Gas temperatures measured in the plume provided further evidence of charged particle expulsion. All flow rates exhibit temperatures of ∼600 K at pressures around 25 Torr before climbing rapidly with pressure up to ∼100 Torr. The gradient of this climb correlates with flow rate, resulting in a strong divergence in temperature; the 10 slpm discharge reaches 1598 K at 108 Torr, while the 5 slpm discharge reaches only 1255 K at 104 Torr. The 7.5, 10 and 12.5 slpm discharges exhibited higher temperatures in the plume than the source for all pressures above 99, 90 and 85 Torr, respectively. Enthalpy calculations were performed, showing equilibration between vibrational and rotational modes cannot account for such temperature increases. An additional source of energy is required to produce such heating downstream, indicating that higher flow rates likely see increased rates of electron-ion recombination in the plume, which would require higher rates of charged particle loss in the plume.

N_2(C) state vibrational temperatures were determined, which provide evidence of vibrational non-equilibrium in high-power nitrogen plasma operating at pressures up to 300 Torr for the first time. The vibrational distribution observed is in line with those previously found in low-power, low-pressure nitrogen discharges, corresponding to an underpopulation of the vibrational ground state compared to vibrational excited states. This arises due to the electron temperatures in the source being sufficiently low that step-wise excitation of the N_2(C) state via the N_2(A) state makes a significant contribution to the N_2(C) population. In contrast to the source, a non-equilibrium distribution was not observed in the plume for any examined condition. This is indicative of a low collision rate between electrons and N_2(A) molecules, likely caused by the plume exhibiting low electron densities compared to the source region.

The N_2^+(B) state temperatures were reported. The rotational temperatures differed significantly from those determined for the N_2(C) state due, despite both molecules exhibiting similar rotational constants. This was attributed to the ion excited state experiencing higher rates of quenching through collisions with the nitrogen molecule ground state compared to the neutral excited state. An equilibrated vibrational

distribution was found in both the source and plume. The rate of equilibration between rotational and vibrational temperatures was found to increase with both flow rate and pressure in the source, with the temperatures of the 7.5 slpm discharge differing by only ∼17% at 216 Torr. This behaviour is not repeated in the plume, where all flow rates see rotational temperatures maintain values ∼50% that of the vibrational temperature at the same pressure. Such differences may be attributable to the dominant production of the $N_2^+(B)$ state shifting from direct excitation from $N_2(X)$ in the source toward excitation of $N_2^+(X)$ in the plume.

Thermal performance of the device was evaluated using calculated thermal efficiencies and measurements of chiller water temperature. The thermal efficiency of the torch was determined using the neutral gas temperatures measured downstream. Due to high temperatures attributed to recombination in the plume, the 10 and 12.5 slpm flows were found to exhibit the highest efficiencies, reporting 66.0% at 204 Torr and 67.4% at 125 Torr respectively. 32.6-34% of input power lost to both the walls and as radiative emissions compares favourably to findings for argon plasma in the supersonic ICP device, which reported a minimum of 30% of power lost exclusively to the walls. Accounting for radiative losses, the thermal efficiency of this device likely matches or exceeds those achieved by the prior iteration. Measured chiller water temperatures showed strong sensitivity to both flow rate and discharge pressure. Higher temperatures were reported for lower flow rates, and all flow rates saw temperature increase with pressure. The former correlation suggests that lower flow rates exhibit higher recirculation rates, further supporting the hypothesised enhancement of charged particle loss to the plume with increased flow rate.

Plasma Behaviour

The electron temperatures determined using the model are strongly dependent on pressure and exhibit little variation across flow rates. The highest values were found for discharge pressures of 3 Torr, reaching 1.46 eV. As pressure increases, electron temperature declines, reaching a minimum of 0.8 eV at 300 Torr. These values generally align with those observed in argon discharges in similar devices. The electron temperature varying little between flow rates can be attributed to neutral gas density exhibiting a similar invariance, which emerges due to the source region gas temperatures differing across flow rates by less than ∼20%.

Unlike electron temperatures, calculated electron densities see significant divergence among flow rates. Below 60 Torr, electron densities rise approximately linearly with pressure for all flow rates, reaching 5-6 $\times$ 10^{19} m^{-3}. As pressure increases further, the increase in electron density slows and eventually plateaus for the highest examined

Flow Rate	Electron Density (m^{-3})
2.5 slpm	1.46×10^{20} @ 188 Torr
5 slpm	1.89×10^{20} @ 301 Torr
7.5 slpm	1.15×10^{20} @ 216 Torr
10 slpm	8.41×10^{19} @ 156 Torr
12.5 slpm	7.57×10^{19} @ 123 Torr

Table 5.1: Maximum electron densities achieved by feed gas flow rate, 950 W supplied power. Note that the 2.5 slpm discharge did not exhibit an electron density plateau in the examined pressure range, which did not extend beyond 188 Torr due to the plume being too dim for OES measurements.

flow rate, 12.5 slpm, while lower flow rate discharges see electron density continue to increase. This plateauing occurs for the three highest flow rates examined, each departing from the near-linear trend in reverse order of flow rate. As a result, at 100 Torr and above, the electron density in a discharge is strongly correlated to its feed gas flow rate. Table 5.1 provides the maximum electron densities observed for each flow rate.

The correlation between observed plateaus in electron density and plume gas temperatures that exceed source gas temperatures was examined for the 7.5, 10 and 12.5 slpm flow rates. It was found that the pressures at which electron density plateaus start match those where plume gas temperatures eclipse source gas temperatures, strongly indicating that high rates of charged particle losses to the plume cause both the increased gas heating and reductions in electron density observed for high flow rates.

Measurements of power transfer efficiency reflect the lower electron densities achieved in high flow rate discharges when pressure exceeds 50 Torr. High flow rate discharges see efficiency climb with pressure at low pressures, reaching a peak of 76-77.5% between 42 and 73 Torr, before declining an average of 1% every 10 Torr. The pressure at which this peak efficiency occurs decreases as flow rate increases, resulting in an inverse correlation between flow rate and efficiency at high pressures. Evaluation of the skin depth at each data-point indicated that the observed declines in efficiency correspond to increases in skin depth, produced by the observed electron density plateaus. No discharge studied was found to have a skin depth smaller than the plasma radius; all flow rates exhibited a minimum value of $\sim$16 mm. Starting from this value, any increase in skin depth therefore reduces the effective resistance and thus power transfer efficiency of the plasma.

These results were compared to electron density and power transfer efficiency measurements performed using the same methods in argon plasmas in the 13.56 MHz

supersonic ICP torch upon which the device studied in this work was based. While the use of a supersonic nozzle and downstream pressure control precluded direct comparison, similar trends in both plasma properties with respect to pressure and flow rate were observed. Of particular note is that both devices exhibit flow rate-dependant electron density plateaus, and achieve similar maximum electron density values of $\sim 2 \times 10^{20}$ m^{-3} across a similar pressure range, using similar absorbed powers. As argon plasma requires less input power than nitrogen plasma to sustain a given electron density, this agreement is surprising. Source region gas flow effects were identified as a likely cause for such shared behaviour, as both devices use the same reverse vortex gas flow in the source.

Oscillations in plasma brightness and resistance were observed during operation of the device. Time-resolved measurements of these oscillations using a photo-diode were performed to characterise them with respect to flow rate, pressure and applied power. The phase of the oscillation observed in the optical emissions was compared to that observed in the coil current and determined to be caused by fluctuations in electron density. The oscillation frequency measured ranged from a maximum of 310 Hz for a 600 W, 3.5 slpm discharge at 20 Torr, to a minimum of 14 Hz for a 950 W, 12 slpm discharge at 725 Torr. The oscillation was found to have a baseline amplitude that increased with power, upon which an additional contribution from a flow rate-dependant component could further increase the severity of the oscillation. The flow rate above which this additional contribution was observed likely increase with power and decreases with pressure. At 950 W, the baseline amplitude of the intensity oscillation was found to be $\sim$20% of the average brightness of the plasma, while the additional flow rate-dependant component brought this up to $\sim$50%.

The rate of charged particles being carried downstream into the plume increasing with flow rate was proposed to explain the observed trends in and oscillation of electron density. Ions are subject to inertial forces produced by the gas flow through the source and can therefore be carried out of the source and into the plume. Ambipolar diffusion causes an equal number of electrons to follow, maintaining quasi-neutrality of the plasma. Source region inertial forces are proportional to gas density, which increases with pressure, and flow velocity, which increases with flow rate. The implications of an electron loss function that includes contributions from the bulk gas flow were explored and found to possibly explain the pressure and flow rate dependencies exhibited by the electron density plateaus. Additionally, it was found that including a term corresponding to the electron recirculation rate in the electron loss function may result in an electron density oscillation, such as that observed at higher pressures and flow rates. A physical interpretation of such an oscillation was

proposed. Further work is required to model and experimentally confirm the loss function exhibited by the device.

5.2 Future Works

The results of this work indicate that both the plasma behaviour and thermal characteristics of high-pressure, high-flow rate RF-ICP torches likely experience significant effects from enhanced rates of charged particles being swept out the source region and into the plume. These include detrimental changes, such as reductions in power transfer efficiency and the presence of destabilising oscillations. They also include a significant benefit, however: increased plume temperatures and thus thermal efficiencies due to higher rates of electron-ion recombination in the plume. In order to develop RF-ICP torches optimised for use in high-temperature industrial processes, deeper understanding of the charged particle loss function of such devices is necessary.

This section suggests avenues of future research with two goals: confirmation that the discharges studied in this work experience charged particle loss functions dominated by expulsion; and characterisation of the loss function with respect to input power, driving frequency, discharge pressure and feed gas flow rate.

- Characterisation of the charged particle loss function would require understanding of the flow regime within the source region, particularly the gas flow velocity under given pressure, flow rate and input power conditions. Computational fluid dynamics (CFD) modelling may be used alongside experimental temperature and power transfer efficiency results to quantify flow velocities and provide insight into gas dynamics in the source.
- Replacing the alumina tubes of the plasma source with quartz would permit transverse imaging of the source region plasma across a range of axial distances from the choke. Comparing second positive system emissions captured at various axial positions in the plasma can provide an axially-resolved proxy measurement of electron density, as the degree of equilibration between the vibrational levels of $N_2(C)$ corresponds to the collision rate between electrons and the long-lived $N_2(A)$ state. These measurements can be used to determine where in the device electron-ion recombination occurs. This would confirm the findings in this work that plasma passing the injector optical access port has already undergone significant recombination.
- Electron temperature is strongly correlated to the charged particle loss function. Explicit measurement of the electron temperature in the source could therefore

be used to evaluate the loss rate of a discharge. Comparison between measured loss rates and those predicted by diffusion to the walls can be used to confirm the global model of the discharge is missing sources of particle loss and quantify the deficit. The excitation temperature in the source could be determined by adding a trace amount of argon to the feed gas and performing OES measurements using atomic argon emission lines, as performed in Ref. [11]. This would require modelling and subtraction of the nitrogen first positive emission system, and would be limited to argon lines that do not overlap the second positive system, as a similar subtraction of that system is not possible due to a known metastable excitation reaction between argon atoms and nitrogen molecules [122].

- Combining the two experiments outlined above, a detailed collisional-radiative model could be developed to take axially-resolved measurements of both electron temperature and $N_2(C)$ vibrational distribution and output axially-resolved values of electron density. This would allow the charged particle expulsion rate to be quantified.

- Density of atomic nitrogen in the plume could be used as a proxy measurement for the charged particle loss rate, as it is produced by recombination reactions. If atomic emission lines in the plume are strong enough to reliably measure amongst contributions from the molecular first positive system, the density could be determined using absolute intensity-calibrated measurements of lines with wavelengths in the 730-760 nm. Otherwise, analysis of less commonly examined lines such as those around 822 nm as in Ref. [123] may be possible using a similar OES set-up, or a high-sensitivity monochromator could be used to examine the forbidden emission line at 346.65 nm as in Ref. [113]. Inferring atomic nitrogen densities may also be possible through detailed modelling and measurement of molecular nitrogen emission systems, as the efficient quenching of vibrationally-excited molecules by atomic nitrogen should lead to perturbations in the population distribution of the molecular excited state. Alternatively, two-photon absorption laser-induced fluorescence (TALIF) may be necessary, as used in Ref. [124], though the high operating pressures and low atomic nitrogen concentrations present in the device may lead to unusably high signal-to-noise ratios.

5.3 Final Remarks

This thesis motivated and detailed the development and experimental characterisation of a reverse vortex-fed RF-ICP torch capable sustaining plasma in pure nitrogen

flows at high pressures. Optical emission spectrometry and resistance measurements were used alongside a simple global model to examine the plasma behaviour and thermal characteristics of discharges in the device with respect to varying feed gas flow rate and operating pressure. The torch was found to produce promising downstream temperatures and thermal efficiencies when using operated with high feed gas flow rates and at high pressures. These conditions aligned with electron density and plasma oscillation results that suggest a significant share of charged particles may be expelled into the plume. Further work examining and characterising the charged particle loss functions of high-pressure, high-flow rate RF-ICPs is necessary to optimise torch designs for use as sources of industrial process heat. The results presented in this work indicate that reverse vortex stabilised RF-ICPs are capable of operation using pure nitrogen gas, and can achieve thermal efficiencies similar to those of arc-discharge plasma sources.

Bibliography

[1] Kali Charan Sabat. Physics and Chemistry of Solid State Direct Reduction of Iron Ore by Hydrogen Plasma. *Physics and Chemistry of Solid State*, 22(2):292–300, May 2021.

[2] Hossam A. Gabbar, Sharif Abu Darda, Vahid Damideh, Isaac Hassen, Mohamed Aboughaly, and Davide Lisi. Comparative study of atmospheric pressure DC, RF, and microwave thermal plasma torches for waste to energy applications. *Sustainable Energy Technologies and Assessments*, 47:101447, October 2021.

[3] Wencong Zhang, Junwu Tao, Kama Huang, and Li Wu. Numerical Investigation of the Surface Wave Formation in a Microwave Plasma Torch. *IEEE Transactions on Plasma Science*, 45(11):2929–2939, November 2017.

[4] Michael A. Lieberman and Allan J. Lichtenberg. *Principles of Plasma Discharges and Materials Processing*. Wiley, 1 edition, April 2005.

[5] Ash Pascale, Trevor Lafleur, and Cormac S Corr. Bidirectional Vortex Stabilization of a Supersonic Inductively Coupled Plasma Torch. *Journal of Physics D: Applied Physics*, February 2023.

[6] Mi-Young Song, Hyuck Cho, Grzegorz P. Karwasz, Viatcheslav Kokoouline, and Jonathan Tennyson. Cross Sections for Electron Collisions with N2, N2*, and N2+. *Journal of Physical and Chemical Reference Data*, 52(2):023104, June 2023.

[7] Ángel Yanguas-Gil, José Cotrino, and Luís L Alves. An update of argon inelastic cross sections for plasma discharges. *Journal of Physics D: Applied Physics*, 38(10):1588–1598, May 2005.

[8] Alf Lofthus and Paul H. Krupenie. The Spectrum of Molecular Nitrogen. *Journal of Physical and Chemical Reference Data*, 6(1):113–307, 1977.

[9] Forrest R. Gilmore. Potential energy curves for N2, NO, O2 and corresponding ions. *Journal of Quantitative Spectroscopy and Radiative Transfer*, 5(2):369–IN3, March 1965.

[10] A. Murmantsev, A. Veklich, V. Boretskij, A. Shapovalov, and A. Kalenyuk. Optical Emission Spectroscopy of Magnethron Discharge Ar/Cu Plasma. *Plasma Physics and Technology*, 6(1):87–90, July 2019.

[11] A Pascale, T Lafleur, and C S Corr. Parametric study of a vortex-enhanced supersonic inductive plasma torch. *Journal of Physics D: Applied Physics*, 57(43):435206, November 2024.

[12] Pascal Chabert and Nicholas Braithwaite. *Physics of Radio-Frequency Plasmas*. Cambridge University Press, 1 edition, February 2011.

[13] De Benedictis and G Dilecce. Vibrational relaxation of N_2(C, u) state in N_2 pulsed rf discharge: electron impact and pooling reactions. *Chemical Physics*, (192):149–162, 1995.

[14] European Commission. Joint Research Centre. and IEA. *GHG emissions of all world countries*. Publications Office, LU, 2024.

[15] Energy Institute. Statisitcal Review of World Energy 2025 (74th Edition), 2025.

[16] WEF. Scaling the Industrial Transition: Hard-to-Abate Sectors and Net-Zero Progress in 2025, December 2025.

[17] Jan Rosenow, Cordin Arpagaus, Stefan Lechtenböhmer, Sem Oxenaar, and Elian Pusceddu. The heat is on: Policy solutions for industrial electrification. *Energy Research & Social Science*, 127:104227, September 2025.

[18] REN21. Renewables 2024 Global Status Report, 2024.

[19] IEA. Renewables 2025, October 2025.

[20] Keith Lovegrove, Dani Alexander, Roman Bader, Stephen Edwards, Michael Lord, Ahmad Mojiri, Jay Rutovitz, Hugh Saddler, Cameron Stanley, Kali Urkalan, and Muriel Watt. Renewable Energy Options for Industrial Process Heat, 2019.

[21] Daniel Navia Simon and Laura Diaz Anadon. Power price stability and the insurance value of renewable technologies. *Nature Energy*, 10(3):329–341, January 2025.

[22] Dolf Gielen, Deger Saygin, Emanuele Taibi, and Jean-Pierre Birat. Renewables-based decarbonization and relocation of iron and steel making: A case study. *Journal of Industrial Ecology*, 24(5):1113–1125, October 2020.

[23] Keith Lovegrove, Dani Alexander, Roman Bader, Stephen Edwards, Michael Lord, Ahmad Mojiri, Jay Rutovitz, Hugh Saddler, Cameron Stanley, Kali Urkalan, and Muriel Watt. Renewable Energy Options for Industrial Process Heat Appendices, 2019.

[24] Ehsan Fooladgar, Alexey Sepman, Yngve Ögren, Andreas Johansson, Marcus Gullberg, and Henrik Wiinikka. Low-NOx thermal plasma torches: A renewable heat source for the electrified process industry. *Fuel*, 378:132959, December 2024.

[25] Nishit Patel, Mitren Sukhram, Ian Cameron, Veena Subramanyam, Alex Gorodetsky, and Manuel Huerta. The Use of Plasma Torches in Blast Furnace Ironmaking. In *ABM Proceedings*, pages 348–357, Rio de Janeiro, September 2016. Editora Blucher.

[26] F.F. Chen. *Introduction to Plasma Physics and Controlled Fusion: Volume 1: Plasma Physics*. Springer US, 3rd ed. edition, 2013.

[27] Maher I. Boulos, Pierre Fauchais, and Emil Pfender. *Thermal Plasmas*. Springer US, Boston, MA, 1994.

[28] Anthony B Murphy and Dirk Uhrlandt. Foundations of High-Pressure Thermal Plasmas. *Plasma Sources Science and Technology*, 27(6):063001, June 2018.

[29] Qihao Jiang, Zhenyu Liu, Yue Niu, Yanan Xie, and Yanming Liu. Calculations of flow field and heat exchange properties in high-power high-enthalpy inductively coupled plasma generator. *Physics of Plasmas*, 31(4):043511, April 2024.

[30] Kazuhisa Fujita, Toshiyuki Suzuki, Masahito Mizuno, and Keisuke Fujii. Comprehensive Characterization of Test Flows in 110-kW Inductively-Coupled-Plasma Heater. In *46th AIAA Aerospace Sciences Meeting and Exhibit*, Reno, Nevada, January 2008. American Institute of Aeronautics and Astronautics.

[31] Yue Niu, Weimin Bao, Donglin Liu, Xiaoping Li, and Yanming Liu. Analysis of enthalpy and energy conversion efficiency in high-power inductively coupled plasma. *Vacuum*, 225:113220, July 2024.

[32] Maher I. Boulos, Pierre L. Fauchais, and Emil Pfender. Thermal Arcs. In *Handbook of Thermal Plasmas*. Springer International Publishing, Cham, 2023.

[33] P. Fauchais and A. Vardelle. Thermal plasmas. *IEEE Transactions on Plasma Science*, 25(6):1258–1280, December 1997.

[34] Johannes W Oswald, Georg Herdrich, Adam S Pagan, Alexander Behnke, and Jasmine Giacomelli. Evaluation of High Enthalpy Air Plasma Conditions for Investigation of Magnetohydrodynamic Flow Interactions. In *Proceedings of the 2nd International Conference on Flight Vehicles, Aerothermodynamics and Re-entry Missions Engineering (FAR)*, Heilbronn, Germany, 2022.

[35] Monika Auweter-Kurtz and Thomas Wegmann. Overview of IRS Plasma Wind Tunnel Facilities. In *RTO EN-8*, October 1999.

[36] Peter M. Finch, Zev N. Granowitz, Christopher L. Strand, Ronald K. Hanson, Megan E. MacDonald, Frank C. L. Hui, and Tahir Gökçen. Temperature and Enthalpy Characterization of NASA Arcjet Using Oxygen and Nitrogen Absorption. *Journal of Thermophysics and Heat Transfer*, 39(4):936–955, October 2025.

[37] P Fauchais and A Vardelle. Pending problems in thermal plasmas and actual development. *Plasma Physics and Controlled Fusion*, 42(12B):B365–B383, December 2000.

[38] M Baeva, M S Benilov, T Zhu, H Testrich, T Kewitz, and R Foest. Modelling and experimental evidence of the cathode erosion in a plasma spray torch. *Journal of Physics D: Applied Physics*, 55(36):365202, September 2022.

[39] Maher I. Boulos, Pierre L. Fauchais, and Emil Pfender. Electrode Phenomena in Plasma Sources. In *Handbook of Thermal Plasmas*. Springer International Publishing, Cham, 2023.

[40] Tejashwi Rana and Satyananda Kar. Study of preheating temperature and electrode consumption in a plasma gasification system for waste processing. *Journal of the Energy Institute*, 120:102122, June 2025.

[41] Jörg Leicher, Anne Giese, and Christoph Wieland. Electrification or Hydrogen? The Challenge of Decarbonizing Industrial (High-Temperature) Process Heat. *J*, 7(4):439–456, October 2024.

[42] Wencong Zhang, Li Wu, Kama Huang, and Junwu Tao. Propagating modes of the travelling wave in a microwave plasma torch with metallic enclosure. *Physics of Plasmas*, 26(4):042101, April 2019.

[43] Javier F De La Fuente, Anton A Kiss, Marilena T Radoiu, and Georgios D Stefanidis. Microwave plasma emerging technologies for chemical processes.

Journal of Chemical Technology & Biotechnology, 92(10):2495–2505, October 2017.

[44] Sirius. Sirius 100 kW Microwave Plasma Torch | Radom Corporation.

[45] Guoxing Chen, Rony Snyders, and Nikolay Britun. CO2 conversion using catalyst-free and catalyst-assisted plasma-processes: Recent progress and understanding. *Journal of CO2 Utilization*, 49:101557, July 2021.

[46] Forhad Hossain, Jeffrey V. Turner, Robert Wilson, Ling Chen, Geoffrey De Looze, Juliano Katrib, Chris Dodds, and Georgios Dimitrakis. Microwave plasma as an efficient energy source for metal powder melting in additive manufacturing and powder metallurgy. *Applied Thermal Engineering*, 299:131198, July 2026.

[47] Sai Likitha Siddanathi, Lars-Göran Westerberg, Hans O. Åkerstedt, Henrik Wiinikka, and Alexey Sepman. The Effect of Non-Transferred Plasma Torch Electrodes on Plasma Jet: A Computational Study. *Applied Sciences*, 15(15):8367, July 2025.

[48] Peter J Hammond. *Characterization and Gas Temperature Measurements of a Waveguide-Based Microwave Plasma Torch*. Doctoral Dissertation, The Pennsylvania State Univerity, August 2013.

[49] Benoit Bottin, Mario Carbonaro, Stefan Zemsch, Gerard Degrez, Benoit Bottin, Mario Carbonaro, Stefan Zemsch, and Gerard Degrez. Aerothermodynamic design of an inductively coupled plasma wind tunnel. In *32nd Thermophysics Conference*, Atlanta,GA,U.S.A., June 1997. American Institute of Aeronautics and Astronautics.

[50] Igor Matveev. Key Selection Criteria and Analysis of Plasma Source Parameters for Modern Industrial Plasma. *arXiv*, 2025.

[51] Thomas B. Reed. Induction-Coupled Plasma Torch. *Journal of Applied Physics*, 32(5):821–824, May 1961.

[52] Thomas R. Smith and M. Bonner Denton. A High-Pressure Inductively Coupled Plasma Torch. *Applied Spectroscopy*, 41(4):654–657, May 1987.

[53] M. I. Boulos. The inductively coupled R.F. (radio frequency) plasma. *Pure and Applied Chemistry*, 57(9):1321–1352, January 1985.

[54] Ali Ebrahimi, Sina Alavi, and Javad Mostaghimi. Development and experi-

mental validation of a high-power conical RF-ICP torch for advanced material processing. *Applied Thermal Engineering*, 289:129771, March 2026.

[55] Maher I. Boulos. New Frontiers in Thermal Plasmas from Space to Nanomaterials. *Nuclear Engineering and Technology*, 44(1):1–8, February 2012.

[56] Yasunori Tanaka. Recent development of new inductively coupled thermal plasmas for materials processing. *Advances in Physics: X*, 6(1), January 2021.

[57] J.M. Larson, M.T. Swihart, and S.L. Girshick. Characterization of the near-surface gas-phase chemical environment in atmospheric-pressure plasma chemical vapor deposition of diamond. *Diamond and Related Materials*, 8(10):1863–1874, October 1999.

[58] Ramona Pristavita, Norma-Yadira Mendoza-Gonzalez, Jean-Luc Meunier, and Dimitrios Berk. Carbon Nanoparticle Production by Inductively Coupled Thermal Plasmas: Controlling the Thermal History of Particle Nucleation. *Plasma Chemistry and Plasma Processing*, 31(6):851–866, December 2011.

[59] Alexander Chirokov, Alexander Gutsol, Alexander Fridman, and Lawrence Kennedy. Reverse-vortex plasma stabilization: experiments and numerical simulation. In *Proceedings of the 15th International symposium on plasma chemistry*, 2001.

[60] Akbar. Montaser and Velmer A. Fassel. Inductively coupled plasmas as atomization cells for atomic fluorescence spectrometry. *Analytical Chemistry*, 48(11):1490–1499, September 1976.

[61] Samira Elaissi, Amira Trabelsi, Fatemah Alkallas, Tahani Alrebdi, and Kamel Charrada. Energy Efficiency Enhancement of Inductively Coupled Plasma Torch: Computational Study. *Materials*, 15(15):5213, July 2022.

[62] Stanley Greenfield and Maryanne Thomsen. Atomiser, source, inductively coupled plasmas, in atomic fluorescence spectrometry (ASIA). Some recent work. *Spectrochimica Acta Part B: Atomic Spectroscopy*, 40(10-12):1369–1377, January 1985.

[63] Sina Alavi, Taghi Khayamian, and Javad Mostaghimi. Conical Torch: The Next-Generation Inductively Coupled Plasma Source for Spectrochemical Analysis. *Analytical Chemistry*, 90(5):3036–3044, March 2018.

[64] A Gutsol and J A Bakken. A new vortex method of plasma insulation and explanation of the Ranque effect. *J. Phys. D: Appl. Phys.*, pages 704–711, 1998.

[65] T. Lafleur and C. S. Corr. Characterization of a radio-frequency inductively coupled electrothermal plasma thruster. *Journal of Applied Physics*, 130(4):043304, July 2021.

[66] David Bohm. *Quantum Theory*. Dover Publications, 2012. OCLC: 868271771.

[67] Xingyue Jin, Peng Zhao, Lin Li, Chengzhou Liu, Chuanwen Geng, Qifu Lin, and Liqun Hu. Diagnostic study of atmospheric pressure inductively coupled plasma temperature field based on image and relative spectral line method. *Vacuum*, 232:113841, February 2025.

[68] BenchChem Technical Support Team. Argon vs. Nitrogen: A Cost-Performance Comparison for the Modern Laboratory, April 2026.

[69] Akbar Montaser, Izumi Ishii, B.A. Palmer, and L.R. Layman. Line widths and temperatures of Ar-N2 ICP discharges measured by high-resolution Fourier transform spectrometry. *Spectrochimica Acta Part B: Atomic Spectroscopy*, 45(6):603–612, January 1990.

[70] Gerhard A. Meyer and Ramon M. Barnes. Analytical inductively coupled nitrogen and air plasmas. *Spectrochimica Acta Part B: Atomic Spectroscopy*, 40(7):893–905, January 1985.

[71] J. G. Parker. Rotational and Vibrational Relaxation in Diatomic Gases. *The Physics of Fluids*, 2(4):449–462, July 1959.

[72] Jeffrey I. Steinfeld. *Molecules and radiation : an introduction to modern molecular spectroscopy.* Mit Press, Cambridge, Mass, 2nd ed. edition, 1985.

[73] P J Bruggeman, N Sadeghi, D C Schram, and V Linss. Gas temperature determination from rotational lines in non-equilibrium plasmas: a review. *Plasma Sources Science and Technology*, 23(2):023001, April 2014.

[74] M.H. Abdallah and J.M. Mermet. The behavior of nitrogen excited in an inductively coupled argon plasma. *Journal of Quantitative Spectroscopy and Radiative Transfer*, 19(1):83–91, January 1978.

[75] A. Greig, C. Charles, and R. W. Boswell. Neutral gas temperature estimates and metastable resonance energy transfer for argon-nitrogen discharges. *Physics of Plasmas*, 23(1):013508, January 2016.

[76] Hira Fatima, M. Usman Ullah, S. Ahmad, Mubashair Imran, S. Sajjad, S.Hussain, and A. Qayyum. Spectroscopic evaluation of vibrational tempera-

ture and electron density in reduced pressure radio frequency nitrogen plasma. *SN Applied Sciences*, 3(6):646, June 2021.

[77] Jan Voráč, Lukáš Kusýn, and Petr Synek. Deducing rotational quantum-state distributions from overlapping molecular spectra. *Review of Scientific Instruments*, 90(12):123102, December 2019.

[78] Hafiz Imran Ahmad Qazi and Jian-Jun Huang. The Influence of Metastable Species and Rotational Quantum Numbers on the Derivation of OH (A–X), NO^-

[79] S. J. Doyle and K. G. Xu. Use of thermocouples and argon line broadening for gas temperature measurement in a radio frequency atmospheric microplasma jet. *Review of Scientific Instruments*, 88(2):023114, February 2017.

[80] F. Mavier, F. Zoubian, M. Bienia, J. F. Coudert, M. Lejeune, V. Rat, and P. André. Plasma Spraying of Solution Precursor in Pulsed Mode: In-Flight Phenomena and Coating Deposition. *Plasma Chemistry and Plasma Processing*, 38(4):657–682, July 2018.

[81] Kun Liu, Wenqiang Geng, Xiongfeng Zhou, Qingsong Duan, Zhenfeng Zheng, and Kostya (Ken) Ostrikov. Transition mechanisms between selective O_3 and NO_x generation modes in atmospheric-pressure plasmas: decoupling specific discharge energy and gas temperature effects. *Plasma Sources Science and Technology*, 32(2):025005, February 2023.

[82] E. L. Harris and Lorenzo M. Albacete. Vibrational Relaxation of Nitrogen in the NOL Hypersonic Tunnel No. 4:. Technical report, Defense Technical Information Center, Fort Belvoir, VA, April 1964.

[83] Kazuhisa Fujita and Takashi Abe. Coupled Rotation-Vibration-Dissociation Kinetics of Nitrogen Using QCT Models. In *36th AIAA Thermophysics Conference*, Orlando, Florida, June 2003. American Institute of Aeronautics and Astronautics.

[84] I. Nadler and S. Rosenwaks. Studies of energy transfer processes in triplet states of N_2. I. Energy pooling by vibrationally selected N_2 $(B^3\Sigma_u^+, v)$ molecules. *The Journal of Chemical Physics*, 83(8):3932–3940, October 1985.

[85] John C. Lindon, George E. Tranter, and John Leonard Holmes. *Encyclopedia of spectroscopy and spectrometry*. Academic Press, San Diego, 2000.

[86] Takeshi Sakamoto, Haruaki Matsuura, and Hiroshi Akatsuka. Spectroscopic

study on the vibrational populations of N_2 $C^3\Pi$ and $B^3\Pi$ states in a microwave nitrogen discharge. *Journal of Applied Physics*, 101(2):023307, January 2007.

[87] Michael Steer. *Microwave and RF Design III - Networks*. LibreTexts, May 2026.

[88] Ash Pascale. *A Supersonic Bidirectional Vortex Enhanced Radio-Frequency Inductively Coupled Plasma Torch for Electrothermal Propulsion Applications*. Doctoral Dissertation, Australian National University, Canberra, November 2025.

[89] C O Laux, T G Spence, C H Kruger, and R N Zare. Optical diagnostics of atmospheric pressure air plasmas. *Plasma Sources Science and Technology*, 12(2):125–138, May 2003.

[90] Spectralfit, SAS. Specair User Manual Version 3.0, 2012.

[91] Richard T Jacobsen, Richard B. Stewart, and Majid Jahangiri. Thermodynamic Properties of Nitrogen from the Freezing Line to 2000 K at Pressures to 1000 MPa. *Journal of Physical and Chemical Reference Data*, 15(2):735–909, April 1986.

[92] P. W. Atkins and Julio De Paula. *Physical chemistry for the life sciences*. Oxford University Press ; W.H. Freeman, Oxford, UK : New York, 2006.

[93] Yun Jin, Yiyi Fan, Xiuxia Meng, Weimin Zhang, Bo Meng, Naitao Yang, and Shaomin Liu. Theoretical and Experimental Insights into the Mechanism for Gas Separation through Nanochannels in 2D Laminar MXene Membranes. *Processes*, 7(10):751, October 2019.

[94] Assistant Professor, College of Engineering, University of Buraimi, Al Buraimi, Sultanate of Oman, Oman. and Osama A Marzouk. Assessment of Three Databases for the NASA Seven-Coefficient Polynomial Fits for Calculating Thermodynamic Properties of Individual Species. *International Journal of Aeronautical Science & Aerospace Research*, pages 150–163, November 2018.

[95] R.F. Wuerker, L. Schmitz, T. Fukuchi, and P. Straus. Lifetime measurements of the excited states of N_2 and N_2^+ by laser-induced fluorescence. *Chemical Physics Letters*, 150(6):443–446, September 1988.

[96] L. Abad, D. Bermejo, V. J. Herrero, J. Santos, and I. Tanarro. Molecular Relaxation in Supersonic Free Jets of N_2 and CH_4 from Stimulated Raman Spectroscopy and Time-of-Flight Measurements. *The Journal of Physical Chemistry A*, 101(49):9276–9285, December 1997.

[97] Serguei Filimonov and Jacek Borysow. Vibrational and rotational excitation within the X^1 state of N_2 during the pulsed electric discharge and in the afterglow. *Journal of Physics D: Applied Physics*, 40(9):2810–2817, May 2007.

[98] N. A. Dyatko, I. V. Kochetov, and A. P. Napartovich. Electron temperature in nitrogen afterglow: Dependence of theoretical results on the adopted set of cross sections and on the type of molecular distribution over vibrational levels. *Plasma Physics Reports*, 28(11):965–971, November 2002.

[99] A. Lo, G. Cléon, P. Vervisch, and A. Cessou. Spontaneous Raman scattering: a useful tool for investigating the afterglow of nanosecond scale discharges in air. *Applied Physics B*, 107(1):229–242, April 2012.

[100] C Stewig, S Schüttler, T Urbanietz, M Böke, and A Von Keudell. Excitation and dissociation of CO_2 heavily diluted in noble gas atmospheric pressure plasma. *Journal of Physics D: Applied Physics*, 53(12):125205, March 2020.

[101] K. A. Vereshchagin, V. V. Smirnov, and V. A. Shakhatov. CARS study of the vibrational kinetics of nitrogen molecules in the burning and afterglow stages of a pulsed discharge. *Technical Physics*, 42(5):487–494, May 1997.

[102] R F Boivin and E E Scime. Control of nitrogen species in helicon plasmas. *Plasma Sources Science and Technology*, 14(2):283–292, May 2005.

[103] Helen L Davies, Vasco Guerra, Marjan Van Der Woude, Timo Gans, Deborah O'Connell, and Andrew R Gibson. Vibrational kinetics in repetitively pulsed atmospheric pressure nitrogen discharges: average-power-dependent switching behaviour. *Plasma Sources Science and Technology*, 32(1):014003, January 2023.

[104] Caleb Richards, Elijah Jans, Ilya Gulko, Keegan Orr, and Igor V Adamovich. N_2 vibrational excitation in atmospheric pressure ns pulse and RF plasma jets. *Plasma Sources Science and Technology*, 31(3):034001, March 2022.

[105] N K Bibinov, A A Fateev, and K Wiesemann. On the influence of metastable reactions on rotational temperatures in dielectric barrier discharges in He-N_2 mixtures. *Journal of Physics D: Applied Physics*, 34(12):1819–1826, June 2001.

[106] George C.-Y. Chan, Jacob T. Shelley, Joshua S. Wiley, Carsten Engelhard, Ayanna U. Jackson, R. Graham Cooks, and Gary M. Hieftje. Elucidation of Reaction Mechanisms Responsible for Afterglow and Reagent-Ion Formation

in the Low-Temperature Plasma Probe Ambient Ionization Source. *Analytical Chemistry*, 83(10):3675–3686, May 2011.

[107] G. Dilecce, P.F. Ambrico, and S. De Benedictis. On $N_2(C^3\Pi_u$, v= 0) state lifetime and collisional deactivation rate by N_2. *Chemical Physics Letters*, 444(1-3):39–43, August 2007.

[108] G Dilecce, P F Ambrico, and S De Benedictis. On the collision quenching of $N_2^+(B^2\Sigma_u^+$, v=0) by N_2 and O_2 and its influence on the measurement of E / N by intensity ratio of nitrogen spectral bands. *Journal of Physics D: Applied Physics*, 43(19):195201, May 2010.

[109] M. W. Chase and National Institute of Standards and Technology (U.S.). Nitrogen (N2). In *NIST-JANAF thermochemical tables*, page 1621. American Chemical Society ; American Institute of Physics for the National Institute of Standards and Technology, Washington, DC : New York, 4th ed edition, 1998.

[110] Karl K. Irikura. Experimental Vibrational Zero-Point Energies: Diatomic Molecules. *Journal of Physical and Chemical Reference Data*, 36(2):389–397, June 2007.

[111] L. Uvarova, S. Rednyk, P. Dohnal, M. Kassayová, S. Saito, Š. Roučka, R. Plašil, R. Johnsen, and J. Glosík. Recombination of vibrationally cold N2+ ions with electrons. *The Journal of Chemical Physics*, 158(17):174303, May 2023.

[112] Charlotte E Moore. Selected Tables of Atomic Spectra; A. Atomic Energy Levels - Second Edition; B. Multiplet Tables: N I, N II, N III. Technical Report Section 5, National Bureau of Standards, Washington, DC, May 1975.

[113] A Salmon, N A Popov, G D Stancu, and C O Laux. Quenching rate of N(^{2} P) atoms in a nitrogen afterglow at atmospheric pressure. *Journal of Physics D: Applied Physics*, 51(31):314001, August 2018.

[114] Y Tanaka and T Sakuta. Chemically non-equilibrium modelling of N_2 thermal ICP at atmospheric pressure using reaction kinetics. *Journal of Physics D: Applied Physics*, 35(5):468–476, March 2002.

[115] K.C. Paul and T. Sakuta. Properties study of inductively coupled nitrogen plasmas and pressure effects on them. *Electric Power Systems Research*, 56(3):185–193, December 2000.

[116] Djilali Benyoucef and Mohammed Yousfi. Ar^+ /Ar, $O_2{}^+$ /O_2 and $N_2{}^+$ /N_2 Elastic Momentum Collision Cross Sections: Calculation and Validation Using

the Semi-Classical Model. *Plasma Science and Technology*, 16(6):588–592, June 2014.

[117] Pierre Mariotto. *Kinetics of nonequilibrium recombining nitrogen-argon plasmas*. PhD thesis, Paris-Saclay University, September 2023.

[118] M. Capitelli, C. Gorse, and G.D. Billing. V—V pumping up in non-equilibrium nitrogen: Effects on the dissoviation rate. *Chemical Physics*, 52(3):299–304, November 1980.

[119] Ulysse Dubuet, Pierre Mariotto, Christophe O Laux, and Marie-Yvonne Perrin. Electronic-specific modeling of a nonequilibrium recombining N_2 /Ar plasma and comparison with experiments. *Plasma Sources Science and Technology*, 35(4):045007, April 2026.

[120] S Kawaguchi, K Takahashi, and K Satoh. Electron collision cross section set for N_2 and electron transport in N_2 , N_2 /He, and N_2 /Ar. *Plasma Sources Science and Technology*, 30(3):035010, March 2021.

[121] Nolan M. Uchizono, Marcel P. Georgin, and Michael S. McDonald. Efficiency scaling of inductively coupled plasmas for radio frequency propulsion systems. *Journal of Electric Propulsion*, 3(1):27, November 2024.

[122] L Isola, M López, and B J Gómez. Study of the excitation mechanisms of the second positive system in the negative glow of a N_2 –Ar discharge. *Journal of Physics D: Applied Physics*, 44(37):375204, September 2011.

[123] R. Hayakawa, T. Yoshimura, A. Ashida, N. Fujimura, H. Kitahata, and M. Yuasa. Analysis of nitrogen plasma generated by a pulsed plasma system near atmospheric pressure. *Journal of Applied Physics*, 96(11):6094–6096, December 2004.

[124] Yoshiyuki Teramoto, Ryo Ono, and Tetsuji Oda. Production mechanism of atomic nitrogen in atmospheric pressure pulsed corona discharge measured using two-photon absorption laser-induced fluorescence. *Journal of Applied Physics*, 111(11):113302, June 2012.